Cross-Coupling of Gyrokinetic Turbulence and the Neoclassical Equilibrium in Tokamak Plasmas

Von der Universität Bayreuth
zur Erlangung des Grades eines
Doktors der Naturwissenschaften (Dr. rer. nat.)
genehmigte Abhandlung

von

Felix Seiferling

aus Aschaffenburg

1. Gutachter: Prof. Dr. Arthur G. Peeters
2. Gutachter: Prof. Dr. Volker Naulin

Tag der Einreichung: 23.05.2019
Tag des Kolloquiums: 08.08.2019

Betreut durch Prof. Dr. Arthur G. Peeters

Abstract

Small scale turbulence in a magnetically confined fusion plasma is the major loss channel for energy and critically limits the confinement. This thesis investigates the interactions between the turbulence and the neoclassical equilibrium background in a tokamak fusion plasma and conducts various numerical investigations using the nonlinear gyrokinetic code GKW. It is conventionally assumed that the neoclassical and turbulent description of a plasma can be treated separately. This is, in many cases, a reasonable approximation because of the large separation of the respective length and time scales. Moreover, different aspects of plasma behaviour are well described by employing just the relevant one of these two descriptions. However, cross-coupling can be important in some cases and in this thesis several aspects of turbulence-background cross-coupling are examined.

Firstly, the influence of turbulent dynamics on the neoclassical equilibrium with an emphasis on the turbulence driven stationary electric current is investigated. The neoclassical solution is evaluated using the Hirschmann-Sigmar formalism into which the turbulent dynamics enter as driving terms. These driving terms are evaluated through time averages of gyrokinetic turbulence simulations and are linked with the velocity nonlinearity in the gyrokinetic equation. The time averaged turbulent driving terms provide a non-negligible current drive, despite being a correction of second order in the normalised Larmor radius. For ion temperature gradient mode turbulence, the force exerted due to the heat flux balance is the dominant contribution to the current, which is mostly driven by the electrons, namely by the parallel fluctuations of electron density/temperature and the electrostatic potential. The current is in magnitude comparable to the bootstrap current in the kinetic cyclone base case and increases the total current by a few percent in cases with an experimentally relevant heat flux. A symmetry breaking mechanism for the mode structure along the magnetic field is required for the turbulent current drive. In this study the symmetry breaking is provided by a background rotation or rotation gradient. Consequently the current is nearly linear in the plasma rotation or its gradient. Additional current generation is of great economic interest for tokamaks as the inductive current drive for the poloidal magnetic field naturally limits the operation time.

Secondly, a large scale parameter study of the intrinsic rotation caused by neoclassical modifications to the Maxwellian background in turbulent simulations is performed and a simple scaling model using the first order neoclassical flow and its gradient is developed. The results show that the toroidal angular momentum flux is roughly linear in the parallel flow velocity obtained by the neoclassical theory. This suggests that the parallel flow in the neoclassical equilibrium provides the most important symmetry breaking mechanism required for momentum transport, and allows for a simple scaling law for the flux in terms of the flow. The scaling law provides a good approximation of the intrinsic rotation due to the neoclassical corrections,

but does not perfectly reproduce the momentum flux as there is a significant amount of scatter in the data.

Thirdly, a new damping mechanism for zonal flows is discovered. Zonal flows are toroidally symmetric poloidal shear flows and are not considered a neoclassical phenomena; however, they can be seen as a background flow that couples with the turbulence and has a critical impact on its regulation. It is shown that the radial transport of parallel momentum provides a damping mechanism for the zonal flow relevant for plasmas turbulence close to the nonlinear threshold. The damping mechanism is confirmed by a "Rosenbluth-Hinton" test with a model radial momentum diffusion, in which the decay rate of the residual potential is found to be proportional to the model diffusion coefficient and in good agreement with the analytic result. Nonlinear simulations show that stronger long wavelength zonal flow shearing occurs when momentum transport is suppressed. This is relevant for the spontaneously occurring meso-scale structures in the E×B shear, known as staircases, which critically impact the nonlinear stability at experimentally relevant turbulence levels. The suppression of momentum transport allows for the development of fully developed staircase structures in the E×B shear, which can suppress turbulence completely for a finite time window. No impact on shorter wavelength zonal flows is observed, in contrast to the analytic prediction which suggests a high damping rate. The latter result raises questions about the relevance of the residual zonal flow for turbulence saturation.

Finally, the interplay between an external torque and staircase structures in the E×B shear is investigated. Gyrokinetic simulations show that the E×B shear connected with the external torque does not simply add to the shear of the meso-scale structures. A positive (negative) externally forced E×B shear leads to a broadening of the corresponding region of the staircase, but does not significantly change the plateau value or the narrow layer of zero shear. In consequence, while the space and time averaged shearing rate is enhanced by the external torque, there is little or no effect on the turbulent transport. This raises doubts about the importance of driven or intrinsic rotation as a means to improve plasma confinement close to the stability threshold.

Zusammenfassung

Kopplung zwischen gyrokinetischer Turbulenz und dem neoklassischen Hintergrund in Tokamak-Plasmen

In einem magnetisch eingeschlossenem Fusionsplasma ist kleinskalige Turbulenz der dominante Energieverlustmechanismus und stört den Einschluss signifikant. Diese Dissertation untersucht die Wechselwirkung zwischen Turbulenz und dem neoklassischen Gleichgewichtshintergrund in einem Tokamak-Fusionsplasma, vornehmlich mit Hilfe von numerischen Untersuchungen mit dem nichtlinearen gyrokinetischen Code GKW. Es wird üblicherweise angenommen, dass die neoklassische und turbulente Beschreibung des Plasmas getrennt behandelt werden kann. Aufgrund der großen Unterschiede zwischen den jeweiligen Längen- und Zeitskalen ist dies in vielen Fällen eine vernünftige Näherung. Außerdem können verschiedene Aspekte des Plasmaverhaltens gut beschrieben werden, indem nur die Relevante der beiden Beschreibungen verwendet wird. Allerdings kann die Kreuzkopplung in einigen Fällen wichtig sein. In dieser Arbeit werden mehrere Aspekte der Kopplung zwischen Turbulenz und Hintergrund untersucht.

Erstens wird der Einfluss der turbulenten Dynamik auf das neoklassische Gleichgewicht mit besonderem Augenmerk auf den turbulenzgetriebenen stationären elektrischen Strom untersucht. Die neoklassische Lösung wird mit dem Hirschmann-Sigmar-Formalismus ermittelt, wobei die turbulente Dynamik als zusätzliche Kraftquelle berücksichtigt wird. Diese treibenden Terme werden über die Zeitmittelwerte von gyrokinetischen Turbulenzsimulationen ermittelt und sind mit dem nichtlinearen Geschwindigkeitsterm in der gyrokinetischen Gleichung verknüpft. Die zeitgemittelten turbulenten Quellterme treiben einen nicht vernachlässigbaren Strom, obwohl es sich um eine Korrektur zweiter Ordnung im normalisierten Larmorradius handelt. Bei einer durch die Ionentemperaturgradientenmode getriebenen Turbulenz ist die Kraft, die durch die Wärmeflussbilanz ausgeübt wird, der dominante Beitrag zum Strom, der vornehmlich von den Elektronen getragen wird und zwar durch die parallelen Schwankungen der Elektronendichte/-temperatur und des elektrostatischen Potentials. Der Strom ist von der Größenordnung vergleichbar mit dem *Bootstrap*-Strom im kinetischen *cyclone base case* und erhöht den Gesamtstrom um einige Prozent für einen Fall mit experimentell relevantem Wärmefluss. Für den turbulent getriebenen Strom ist ein Symmetriebrechungsmechanismus für die Modenstruktur entlang des Magnetfeldes erforderlich, der in dieser Studie durch eine Hintergrundrotation oder einen -rotationsgradienten bereitgestellt wird. Folglich ist der Strom nahezu linear in der Plasmarotation oder ihrem Gradienten. Die zusätzliche Stromerzeugung

ist für Tokamaks von großem wirtschaftlichen Interesse, da der induktive Stromantrieb für das poloidale Magnetfeld naturgemäß die Betriebszeit begrenzt.

Zweitens wird die intrinsische Rotation, die durch neoklassische Modifikationen des Maxwellschen Hintergrunds in turbulenten Simulationen verursacht wird, in einer groß angelegten Parameterstudie untersucht. Dabei wird ein einfaches Skalierungsmodell unter Verwendung des parallelen neoklassischen Flusses erster Ordnung und dessen Gradienten entwickelt. Die Ergebnisse zeigen, dass der toroidale Drehimpulstransport in etwa linear in der parallelen Strömungsgeschwindigkeit ist, die durch die neoklassische Theorie ermittelt wird. Dies deutet darauf hin, dass die parallele Strömung im neoklassischen Gleichgewicht den wichtigsten Mechanismus für die Symmetriebrechung, die für den Impulstransport benötigt wird, liefert, und ermöglicht ein einfaches Skalierungsgesetz für den Impulsfluss. Das Skalierungsgesetz bildet den zwar Impulsfluss nicht perfekt ab, d.h. es gibt eine signifikante Streuung in den Daten, bietet aber eine gute Annäherung an die von den neoklassischen Korrekturen getriebene intrinsische Rotation.

Drittens wird ein neuer Dämpfungsmechanismus für zonale Strömungen aufgedeckt. Zonale Strömungen sind toroidalsymmetrische poloidale Scherströme und gelten nicht als neoklassische Phänomene, können aber als Hintergrundströmungen betrachtet werden, die mit der Turbulenz gekoppelt sind und eine kritische Rolle bei der Regulierung von Turbulenz spielen. Es wird gezeigt, dass der radiale Transport von parallelem Impuls einen Dämpfungsmechanismus für die zonale Strömung bietet, der relevant für Turbulenz nahe dem nichtlinearen Schwellenwert ist. Der Dämpfungsmechanismus wird durch einen „Rosenbluth-Hinton"-Test mit einer modellierten radialen Impulsdiffusion bestätigt, wobei die Abklingrate des Residualpotenzials proportional zum Diffusionskoeffizienten ist und in guter Übereinstimmung mit dem analytischen Ergebnis steht. Nichtlineare Simulationen zeigen, dass bei unterdrücktem Impulstransport eine stärkere langwellige Scherung durch die zonale Strömung stattfindet. Dies ist relevant für die spontan auftretenden mesoskaligen Strukturen in der E×B-Scherströmung, die die nichtlineare Stabilität bei experimentell relevanter Turbulenz entscheidend beeinflussen. Die Unterdrückung des Impulstransports ermöglicht die Entwicklung voll ausgeprägter Strukturen in der E×B Scherströmung, die die Turbulenz für ein begrenztes Zeitfenster vollständig unterdrücken können. Im Gegensatz zur analytischen Vorhersage, die auf eine hohe Dämpfungsrate hindeutet, ist kein Einfluss auf zonale Strömungen mit kürzerer Wellenlänge zu beobachten. Dieses Ergebnis wirft die Frage nach der Relevanz der zonalen Residualströmung für die Turbulenzsättigung auf.

Abschließend wird das Zusammenspiel zwischen einem externen Drehmoment und E×B-Scherstrukturen untersucht. Gyrokinetische Simulationen zeigen, dass die mit dem externen Drehmoment verbundene E×B-Scherströmung sich nicht einfach zur Scherung durch die mesoskaligen Strukturen addiert. Eine positive (negative) extern erzwungene E×B-Scherung führt zu einer Verbreiterung des entsprechenden Strukturbereichs, ändert aber weder den Plateauwert noch die schmale Region ohne Scherung wesentlich. Während die räumlich und zeitlich gemittelte Scherrate durch das externe Drehmoment erhöht wird, beeinflusst es den turbulenten Transport dabei wenig bis gar nicht. Dies wirft Zweifel an der Bedeutung von getriebener oder intrinsischer Rotation als Mittel zur Verbesserung des Plasmaeinschlusses nahe dem Schwellwert für Stabilität auf.

Contents

1. Introduction

The promise of virtually unlimited sustainable clean energy from a fusion power plant has motivated about seven decades of research and has never been more appealing than in today's context of looming climate change paired with the ever increasing demand for power. Continuous and impressive progress has been made rivalling the rate of development of microprocessors, maybe one of the greatest success stories in the 20th century (see Fig. 1.1). However, a breakthrough in form of an economically viable reactor is not yet in sight. This shows the many scientific and technical challenges that accompany the task of maintaining a process that in nature only happens in the core of a star.

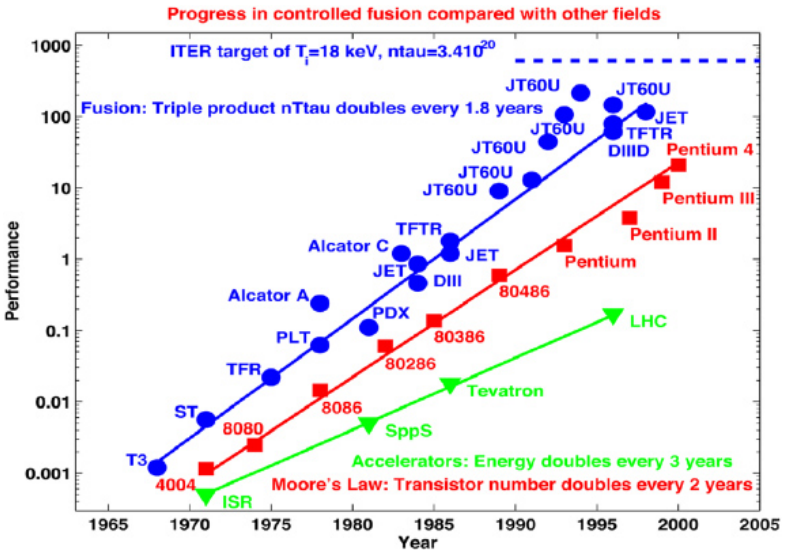

Figure 1.1. Progress in fusion research measured by the triple product $nT\tau$ of density, temperature and confinement time. The rate of progress is shown to be in the same league as microelectronics or particle accelerators. Figure from Ref. [1].

The fusion of two light atoms generates a large amount of energy, due to the higher bonding energy of the product, with the most promising reaction being the fusion of the hydrogen isotopes deuterium and tritium

$$ {}^{2}_{1}\mathrm{D} + {}^{3}_{1}\mathrm{T} \longrightarrow {}^{4}_{2}\mathrm{He} + {}^{1}_{0}\mathrm{n} + 17.6\ \mathrm{MeV}, $$

as it exhibits the highest cross section at the required temperature of the order of 100 million Kelvin. The extreme temperatures are required as the nuclei need to overcome their Coulomb repulsion. The fusion plasma (the atoms are ionised at such high temperatures) has to be

confined with minimal energy loss to keep the reaction alive. This is the main challenge of fusion power, for which two solutions, inertial and magnetic confinement, have been studied extensively, with the latter being the most promising approach. In magnetic confinement an external magnetic field is imposed to confine the plasma, with the Lorentz force preventing a motion across the field lines. There are two main concepts for magnetic confinement devices: the tokamak and the stellarator. Both confine the plasma along closed field lines in a torus. While recent stellarator experiments like Wendelstein 7-X have shown great promise, the tokamak has historically been more developed and is the focus of this work. Starting in the late 1950s, tokamak experiments have steadily improved, demonstrating fusion reactions and temperatures hotter than in the core of the Sun [2]. There are several research reactors worldwide, with an example, ASDEX Upgrade, shown in Fig. 1.2, while the first reactor to generate significantly more fusion power than its required input power, ITER, is currently under construction.

Sadly, the particles do not follow the magnetic field line indefinitely but the plasma is subject to a plethora of instabilities. Large scale instabilities which disrupt the confinement, were the main problem in early experiments but are nowadays well understood and kept in check by modern reactor design and control [2]. However, small scale instabilities drive turbulent transport degrading the confinement and are still only partly understood as well as more difficult to control. The underlying physics of microturbulence is highly complex and the nonlinear and high dimensional nature of the problem poses significant challenges for numerical modelling. However, the development of a specialised theory to deal with the large range of time and

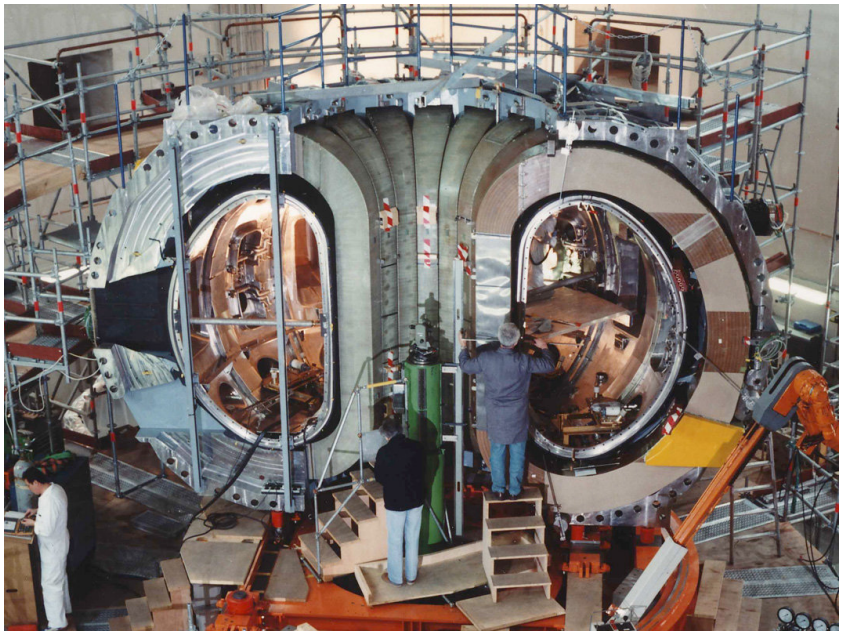

Figure 1.2. The ASDEX Upgrade fusion reactor during assembly. (Source: "Max Planck Institute for Plasma Physics": `https://www.ipp.mpg.de/14905/magnetspulen` [Accessed 25 Apr. 2019])

space scales, the gyrokinetic theory, accompanied by the rise of high-performance computing has allowed for significant progress.

This thesis continues the work on this topic by studying turbulence driven by the ion temperature gradient instability - the dominant instability - and accompanying transport processes. Firstly, the coupling of turbulence with the neoclassical background, which are usually treated separately, is investigated. In Chapter 2 it is shown that turbulence can generate a sizeable plasma current, potentially allowing for longer tokamak operation. Furthermore, the toroidal plasma rotation generated by the neoclassical background is investigated in Chapter 3. Secondly, turbulence suppression connected with the recently discovered structure formation of the zonal flow is studied, detailing the effect of momentum transport in Chapter 4 and plasma rotation in Chapter 5 to gain new insight in the physics processes and to enhance our predictive capabilities of turbulent transport.

Part of the work reported in this thesis has been published in (or submitted to) peer-reviewed journals as listed below:

(a) F. Seiferling, A. G. Peeters, R. Buchholz, S. R. Grosshauser, F. Rath, and A. Weikl. On turbulence driven stationary electric currents in a tokamak. *Physics of Plasmas*, 25(10), 102305, 2018

(b) F. Seiferling, A. G. Peeters, R. Buchholz, S. R. Grosshauser, F. Rath, and A. Weikl. Damping of zonal modes through turbulent momentum transport. *Physics of Plasmas*, 25(2):022505, 2018.

(c) F. Seiferling, A. G. Peeters, S. R. Grosshauser, F. Rath, and A. Weikl. The interplay of an external torque and E×B structure formation in tokamak plasmas; submitted to *Physics of Plasmas*

Chapters 2, 4 and 5 are based on (a),(b) and (c) respectively. Chapter 3 is part of the EUROfusion project WP17-ENR-CEA-02.

The remainder of this chapter first introduces the basic principles of plasma physics and the tokamak reactor in section 1.1. Then the neoclassical theory used to describe the background is briefly discussed in section 1.2 before important aspects of turbulence are explained in section 1.3. Finally, the gyrokinetic theory and gyrokinetic simulations with the code GKW are introduced in sections 1.4 and 1.5.

1.1. Principles of magnetic confinement

This section aims at discussing the fundamental principles required for the advanced theory in the following sections and the later chapters of this thesis. Starting with the motion of a charged particle along a magnetic field in Sec. 1.1.1, the design of the tokamak device and basic associated phenomena are covered in Sec. 1.1.2.

1.1.1. Single particle motion

Here, the motion of a single charged particle in an inhomogeneous magnetic and electric field is discussed. For a more detailed treatment the reader is referred to a standard textbook, like Refs. [3–5].

Subjected to the Lorentz force, charged particles perform a circular motion around the magnetic field line in the plane perpendicular to the magnetic field. The Larmor (or gyro-) radius ρ and cyclotron frequency ω_c of the gyration are given by

$$\rho_s = \frac{m_s v_{\perp,s}}{|Z_s| eB} \qquad \text{and} \qquad \omega_{c,s} = \frac{Z_s eB}{m_s}. \tag{1.1}$$

The subscript s denotes the particle species, m is the particle mass, Z the charge number, e the elementary charge, $v_\perp$ the velocity perpendicular to the magnetic field and B the magnetic induction. For typical parameters in a reactor the gyroradius is of the order of millimetres for deuterium ions and less by roughly a factor of 60 for the electrons. Both the ion as well as the electron Larmor radii are small compared to the system size of several meters. Furthermore, the turbulent fluctuations are slow compared to the ion and electron cyclotron frequencies ($\omega_{c,i} \sim 2 \cdot 10^8 \mathrm{s}^{-1}$, $\omega_{c,e} \sim 8 \cdot 10^{11} \mathrm{s}^{-1}$). This large separation of length and time scales makes it favourable to separate the particle motion into the fast gyration and the slower motion of the gyrocentre. In consequence, the magnetic moment $\mu = m v_\perp^2 / 2B$ is an adiabatic invariant of the motion, i.e. $\mathrm{d}\mu/\mathrm{d}t = 0$.

The free cyclotron motion around the field described above is only valid for straight field lines and no external forces acting on the particle. If a force $\mathbf{F}$ is applied to the particle, the gyrocentre will drift perpendicular to the magnetic field with the drift velocity $\mathbf{v}_d$,

$$\mathbf{v}_d = \frac{\mathbf{F} \times \mathbf{B}}{ZeB^2}. \tag{1.2}$$

The drift velocity is small compared to the thermal velocity v_th or the velocity parallel to the magnetic field $v_\parallel$, as the force can be considered small compared to the Lorentz force connected with the strong magnetic field. However, the gyrocentre drift provides an important correction, since it is a motion perpendicular to the magnetic field, and leads to several new phenomena. There are several drift mechanisms to consider.

First, the E×B drift

$$\mathbf{v}_E = \frac{\mathbf{E} \times \mathbf{B}}{B^2}, \tag{1.3}$$

due to the electrostatic force connected with an electric field **E**, is unique compared to the other drifts as the charge dependency in Eq. 1.2 cancels and the velocity is the same for ions and electrons. If the electric field is not constant, the inertial force connected with the time dependent E×B drift leads to an additional drift, the polarisation drift

$$\mathbf{v}_p = \frac{1}{\omega_c B}\frac{\mathrm{d}\mathbf{E}}{\mathrm{d}t}. \tag{1.4}$$

The second important mechanism is the curvature and ∇B drift

$$\mathbf{v}_D = \frac{m v_\parallel^2 \mathbf{B}\times(\mathbf{B}\cdot\nabla)\mathbf{B}}{ZeB^4} + \frac{\mu \mathbf{B}\times\nabla B}{ZeB^2}. \tag{1.5}$$

Two contributions are considered here. The first term is due to the centrifugal force acting on the particle following a curved field line. The second term is caused by the magnetic mirror force $\mathbf{F} = -\mu\nabla B$ acting on the particle as the magnetic field strength varies over the cyclotron orbit. If the plasma pressure is low compared to the magnetic field strength $\nabla \times \mathbf{B} = 0$ is a good approximation and the curvature term can be rewritten using $(\mathbf{B}\cdot\nabla)\mathbf{B} = B\nabla B$, leading to the commonly used drift velocity

$$\mathbf{v}_D = \left(m v_\parallel^2 + \mu B\right)\frac{\mathbf{B}\times\nabla B}{ZeB^3}. \tag{1.6}$$

Finally, in a rotating plasma that is described in the co-moving frame additional drifts occur. This thesis only considers the drift connected with the Coriolis force [6]

$$\mathbf{v}_c = \frac{2mv_\parallel}{ZeB}\mathbf{\Omega}_\perp, \tag{1.7}$$

where $\mathbf{\Omega}_\perp = \mathbf{\Omega} - (\mathbf{\Omega}\cdot\mathbf{b})\mathbf{b}$ is the part of the angular toroidal rotation vector perpendicular to the field and $\mathbf{b}$ the unit vector in the direction of the magnetic field. The drift due to the centrifugal force connected with the plasma rotation is neglected because it is of second order in $\Omega \sim 0.1 v_{\mathrm{th}}/R$.

The motion of the guiding centre position **X** is given by the movement parallel to the magnetic field and the drift velocity,

$$\frac{\mathrm{d}\mathbf{X}}{\mathrm{d}t} = v_\parallel \mathbf{b} + \mathbf{v}_E + \mathbf{v}_D + \mathbf{v}_p. \tag{1.8}$$

Here, like in the remainder of the thesis, the plasma is assumed to be electrostatic, i.e. $\partial\mathbf{B}/\partial t = 0$, and phenomena connected with local magnetic field fluctuations are not considered.

1.1.2. The tokamak fusion reactor

The tokamak reactor confines the plasma in a torus using a strong magnetic field. For clarity, the toroidal geometry and the associated quantities are shown in Fig. 1.3. The defining feature of the tokamak is the toroidal symmetry, i.e. all properties are invariant to any rotation around the central axis of the torus (z-axis). The toroidal magnetic field is generated by external coils,

with a schematic shown in Fig. 1.4. The toroidal field coils provide the major part of the magnetic field, which is not uniform but has a radial variation $B \sim 1/R$ due to toroidal geometry. As a consequence, this toroidal field alone is not sufficient for confinement. Considering the drift mechanisms discussed previously it is easily seen that the ∇B drift causes charge separation in the plasma and the E×B drift due to the resulting electric field causes the particles to drift outwards in the direction of the major radius. To remove this effect, a secondary magnetic field in the poloidal direction is employed. The field is realised by a toroidal plasma current driven by a central solenoid. The resulting helical winding of the magnetic field lines averages the radial component of the ∇B drift to zero. Thus, the large electric field of the case without a poloidal magnetic field can not build up and the plasma is not ejected. While inductive current drive is the easiest way to generate the toroidal current required for the poloidal magnetic field, it naturally limits the operation time of a tokamak. The current in the central solenoid can not increase indefinitely and additional ways of current generation are needed to extend the length of an operation pulse or achieve stationary operation.

The magnetic field configuration results in helical field lines winding around the torus, they map out nested surfaces with constant magnetic flux ψ, called flux surfaces (see Fig. 1.5), which are described by the Grad-Shafranov equation [8–10].

Equilibrium confinement requires that the pressure force is balanced by the Lorentz force. Using a fluid description of the plasma, also referred to as magnetohydrodynamics (MHD), this can be written as

$$\mathbf{J} \times \mathbf{B} = \nabla p, \tag{1.9}$$

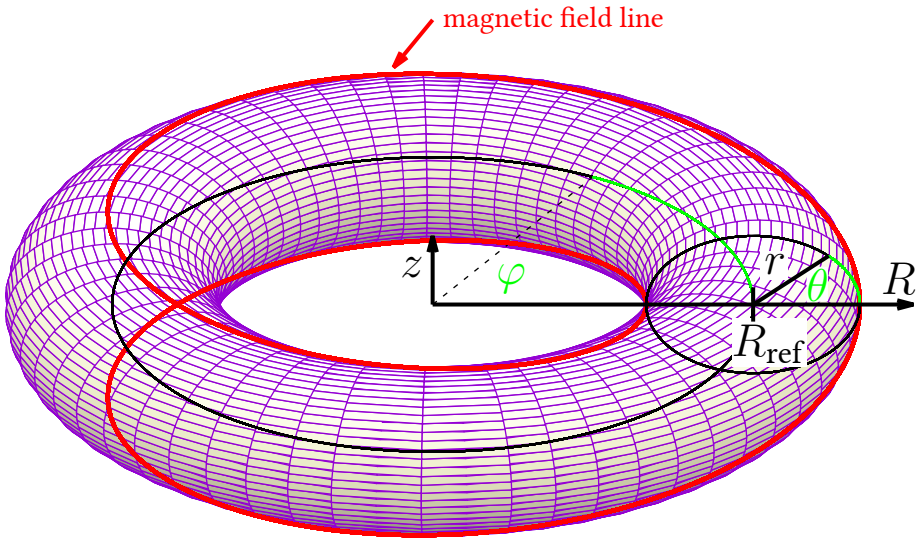

Figure 1.3. The toroidal geometry with major radius R, minor radius r, toroidal angle φ, poloidal angle θ and an example for a helical magnetic field line (red) on a flux surface with safety factor q=2. The field line reaches its original poloidal position after two toroidal turns.

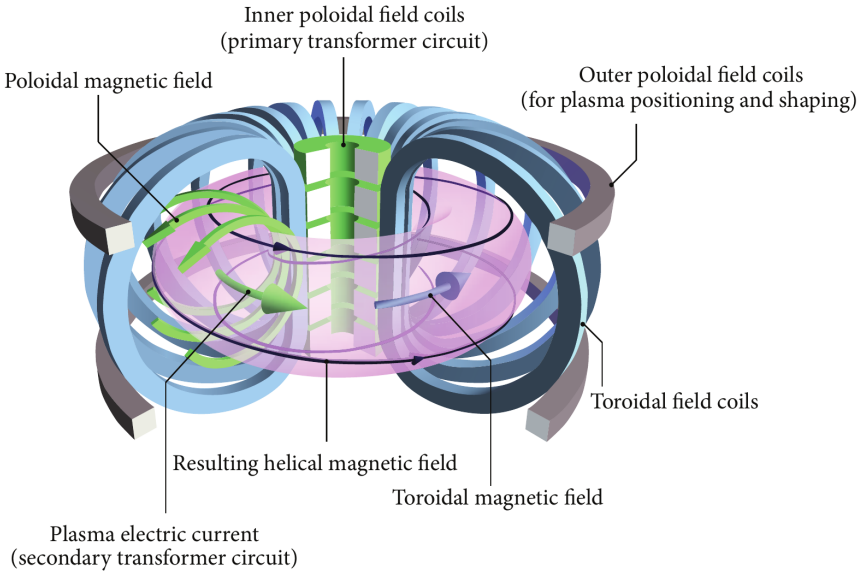

Figure 1.4. Schematic of the setup of the magnetic coils and the resulting magnetic field in a tokamak. Figure from Ref. [7].

where $\mathbf{J}$ is the current and p the pressure of the plasma. Here, we have neglected the centrifugal force, which is only important for strongly rotating plasmas. Two observations can be made here. Firstly, the flux surfaces are also surfaces of constant pressure, because $\mathbf{B} \cdot \nabla p = 0$. Secondly, $\mathbf{J} \cdot \nabla p = 0$ and thus the current must lie in the flux surface. Since the particles can move freely along the magnetic field over the flux surface, the fast thermal motion ensures equilibrium, i.e. density n and temperature T are constant on a flux surface. Thus, the equilibrium satisfies the aforementioned toroidal symmetry. In the context of this force balance, the dimensionless ratio of kinetic and magnetic pressure

$$\beta = \frac{p}{B^2/2\mu_0}, \tag{1.10}$$

with the magnetic permeability μ_0, is a frequently used plasma parameter to describe the quality of confinement and usually has values of a few percent in most tokamaks. Even though the flux surfaces in tokamaks are usually elongated and exhibit triangularity (like in Fig. 1.5), the theoretical description of the plasma often uses circular flux surfaces as a good approximation, especially close to the plasma core. Similarly, in this thesis the flux surfaces are assumed to be concentric and circular. This allows for the minor radius r to be used as the flux surface label.

Several geometric quantities are used for the description of the flux surface. The inverse aspect ratio ϵ,

$$\epsilon = r/R_{\text{ref}}, \tag{1.11}$$

is the ratio of the minor radius over the major radius of the magnetic axis R_{ref}. It is usually

assumed to be small (of the order of 0.1) and, especially when developing a theoretical description, terms are often only considered up to the first order in ϵ. Although numerical calculations, like in the later chapters of this thesis, retain all orders of ϵ. The safety factor q denotes the number of toroidal revolutions required for the magnetic field line to reach its original poloidal position and the name originates from its critical impact on large scale MHD-instabilities. The safety factor is calculated by

$$q = \frac{1}{2\pi} \oint \frac{B_t}{RB_p} \mathrm{d}s \approx \epsilon \frac{B_t}{B_p} \tag{1.12}$$

where $\oint \mathrm{d}s$ is a closed line integral over the flux surface and B_t (B_p) is the toroidal (poloidal) component of the magnetic field. The second expression is valid up to the first order in ϵ. If q has an irrational value the field line does not close upon itself but maps out the whole flux surface. The safety factor is determined by the current profile and in general varies with the minor radius. The magnetic shear $\hat{s}$ is introduced to describe the variation

$$\hat{s} = \frac{r}{q} \frac{\mathrm{d}q}{\mathrm{d}r}. \tag{1.13}$$

Usually, $q > 1$ is required for stability and the safety factor varies from $q \approx 1$ at the magnetic axis up to $3 \sim 5$ at the last closed flux surface (before the field lines interact with the wall).

Due to the conservation of energy and the magnetic moment, there are two different kind of particle orbits: Particles trapped on the low field side and passing particles completing full poloidal turns. Their respective orbits are sketched in Fig. 1.6.

The extrema of the magnetic induction are located in the mid plane of the torus with the

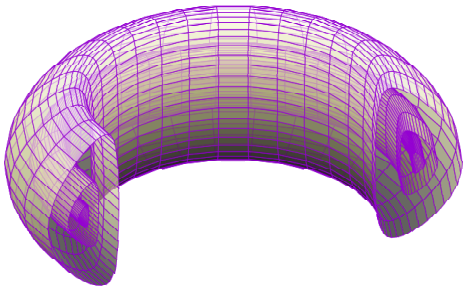

Figure 1.5. Nested flux surfaces in a tokamak.

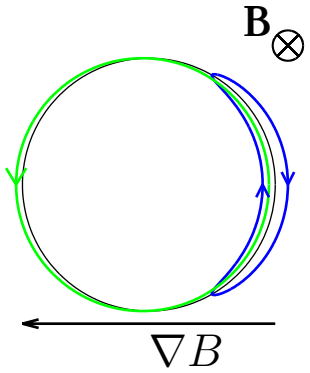

Figure 1.6. Poloidal projection of trapped (blue) and passing (green) ion orbits. The deviation of the orbits from the flux surface is due to the vertical ∇B drift.

minimum on the outboard side and the maximum on the inboard side, called low- and high-field side respectively.

$$B(\theta) = \frac{B_0}{1 + \epsilon \cos\theta}, \tag{1.14}$$

where B_0 is the value of the magnetic field on the magnetic axis. The trapped passing boundary is obtained by setting the parallel velocity on the high field side to zero. Using the conservation of energy

$$E_{\text{kin}} = \frac{1}{2} m \left(v_\parallel^2 + v_\perp^2 \right) = \frac{m v_\parallel^2}{2} + \mu B = \text{const.}, \tag{1.15}$$

the conservation of the magnetic moment and Eq. 1.14 lead to

$$v_\parallel^2 = \frac{2\mu}{m} \left(B_{\text{max}} - B_{\text{min}} \right) = v_\perp^2 \frac{2\epsilon}{1 - \epsilon} \approx 2\epsilon v_\perp^2, \tag{1.16}$$

where B_{max} and B_{min} are the respective strengths of the magnetic field at the high- and low-field side, and the last expression is valid up to the first order in ϵ. If the parallel velocity at the low field side is lower than the threshold given by Eq. 1.16, the parallel velocity reaches zero on the way towards the high field side and the particle will turn around until it bounces again upon approaching the high field, like in a magnetic mirror. Only particles with a parallel velocity higher than the threshold can make a full poloidal turn. As a rough approximation, the fraction $f_t = \sqrt{\epsilon}$ of all particles can be considered trapped.

Similar to the transit frequency $\nu_T = v_{\text{th}}/(2\pi q R)$, the time scale for a full passing orbit parallel to the field line, trapped particle orbits also have a characteristic time scale, the bounce frequency ω_b. In the limit of strongly trapped particles (the poloidal turning point is close to the mid-plane $\theta_b \ll 1$) and large aspect ratio the bounce frequency is given by [3]

$$\omega_b = \sqrt{\frac{\epsilon}{2}} \frac{v_\perp}{qR}. \tag{1.17}$$

Due to the inhomogeneity of the magnetic field the particles do not follow the magnetic field line exactly but are subject to a vertical drift. This drift leads to a radial width of the orbit and, inspired by the shape (see. Fig. 1.6), the term banana orbit is commonly used for trapped particles. The half width w of the orbit can be calculated from the conservation of the canonical toroidal angular momentum, which is an invariant of the motion

$$P_\varphi = m v_\parallel R B_t / B + Z e A_\varphi = \text{const.}, \tag{1.18}$$

where A_φ is the toroidal component of the vector potential with $\mathrm{d}A_\varphi/\mathrm{d}r = R B_p$. Using the approximation $B_t \approx B$ the orbit width is given by

$$w = \frac{m v_\parallel}{Z e B_p}. \tag{1.19}$$

Note that particles are not trapped indefinitely as they can exchange momentum through Coulomb collisions.

1.2. Neoclassical theory

In contrast to the classical theory, which describes the collisionally generated transport of particles and energy across a homogeneous magnetic field, the term neoclassical was established to stress that the theory describes collisional transport in a toroidal geometry. Indeed, the particular features of the particle orbits generated by the drifts in toroidal geometry lead to a strongly enhanced collisionally generated transport. While the thermal loss from collisional transport is up to two orders of magnitude smaller than the turbulent transport due to microinstabilities, neoclassical theory still provides an important baseline for confinement. Furthermore, several aspects of the plasma, like current and resistivity, are governed by neoclassical effects.

Classical transport assumes a plasma with a homogeneous magnetic field, where transport can be understood in terms of a simple diffusion process, where the diffusion coefficient $D = \rho^2/\tau_c$ is determined by the Larmor radius ρ and the collision time τ_c, serving as the characteristic time scale. The toroidal geometry fundamentally changes the behaviour of the plasma. Firstly, due to the curvature there is a toroidally induced force which acts outwards along the major radius, which has to be compensated by a current flow in the plasma. Flux surfaces are surfaces of constant pressure but the area on the outboard side of the torus is larger, due to the larger major radius, than the area on the inboard side. Consequently there is a net imbalance which results in the aforementioned force. Using the force balance $\mathbf{J} \times \mathbf{B} = \nabla p$, the pressure force imbalance has to be counteracted by a vertical current, which in turn is compensated by an internal flow to prevent charge accumulation. The internal current flow, named Pfirsch-Schlüter current and the associated transport is examined in more detail in the next section. Secondly, the fluid description assumes a sufficiently high collisionality, which is not given for the high temperatures in modern fusion plasmas. For the low collisionalities in fusion plasmas the particles perform several transit or bounce orbits before they are scattered by collisions. In this situation the details of the orbits connected with the toroidal geometry have a strong impact on the obtained transport coefficients. Specifically particles trapped on the low field side (see Sec. 1.1.2) trace out a so-called banana orbit which has an orbit width much larger than the Larmor radius. For low collisionality these orbits dominate the diffusive transport and one speaks of the so-called banana regime.

This section aims at covering the aspects of neoclassical theory relevant for this thesis. First the different transport regimes are examined in more detail and the bootstrap current, the most important intrinsic current in a tokamak is explained briefly. Finally, the kinetic description of neoclassical transport using the flux surfaced averaged balance equation is introduced.

1.2.1. Neoclassical transport and current

Based on Ref. [3] this section gives a brief phenomenological discussion of the diffusive neoclassical transport.

Resistive diffusion

The resistive diffusion in a plasma is governed by Ohm's law

$$\mathbf{E} + \mathbf{v} \times \mathbf{B} = \eta \mathbf{j} \tag{1.20}$$

and the force balance

$$\mathbf{j} \times \mathbf{B} = \nabla p, \tag{1.21}$$

where $\mathbf{j}$ is the current. The resistivity η scales with the collision time $\eta \sim m/(ne^2\tau_c)$ but in general it is a tensor and has different values for parallel $\eta_\parallel$ and perpendicular $\eta_\perp$ currents respective to the magnetic field. Crossing Eq. 1.20 with $\mathbf{B}$ and using Eq. 1.21 yields an expression for the perpendicular velocity

$$\mathbf{v}_\perp = \frac{\mathbf{E} \times \mathbf{B}}{B^2} - \eta_\perp \frac{\nabla p}{B^2}, \tag{1.22}$$

where the vector identity $(\mathbf{v} \times \mathbf{B}) \times \mathbf{B} = -B^2 \mathbf{v}_\perp$ is used. In a particle description the terms can be understood as the macroscopic E×B drift and the collisional diffusion of the particles. The diffusive nature of the second term becomes apparent when considering the continuity equation for $\mathbf{E} = 0$ and constant temperature

$$\frac{\partial n}{\partial t} = -\nabla \cdot (n \mathbf{v}_\perp) = \nabla \cdot \frac{\eta_\perp n T \nabla n}{B^2} = \frac{\eta_\perp \beta}{2\mu_0} \nabla^2 n, \tag{1.23}$$

where for the last step the plasma beta $\beta = nT/(B^2/2\mu_0)$ is used and its local variation is neglected.

For high collisionality, the influence of trapped particles can be neglected and the neoclassical transport is described by the Pfirsch-Schlüter regime. High collisionality means that particles are scattered before they can perform a full transit orbit, i.e. the collision frequency ν has to satisfy $\nu > v_{\text{th}}/(qR)$. The Pfirsch-Schlüter current can be approximated by a simple calculation only considering the mid-plane of the torus. The outboard side of the flux surface has a larger surface area than the inboard side but the pressure on the flux surface is constant, resulting in the outward force density F along the major radius

$$F \sim \frac{r}{R} \frac{\mathrm{d}p}{\mathrm{d}r}. \tag{1.24}$$

A vertical current j_z balances the force

$$j_z \sim \frac{1}{B} \frac{r}{R} \frac{\mathrm{d}p}{\mathrm{d}r}, \tag{1.25}$$

where $B_t \approx B$ is used. A current $j_\parallel$ parallel to the field arises to prevent charge accumulation. The vertical component of the current must balance j_z. At the mid-plane where the poloidal and vertical direction are identical and the parallel current is

$$j_\parallel = \frac{B}{B_p} j_p = -\frac{B}{B_p} j_z \sim -\frac{1}{B_p} \frac{r}{R} \frac{\mathrm{d}p}{\mathrm{d}r}. \tag{1.26}$$

The formal calculation is slightly more complex, but the Pfirsch-Schlüter current j_{PS} has a similar form for circular flux surfaces in the large aspect-ratio limit (up to the first order in $\epsilon = r/R$) and is given by,

$$j_{\mathrm{PS}} = -\frac{2\epsilon}{B_p}\frac{\mathrm{d}p}{\mathrm{d}r}\cos\theta. \tag{1.27}$$

The $\cos\theta$ variation is due to the orientation of the poloidal component of the current to the vertical direction. The Pfirsch-Schlüter current drives a perpendicular flow,

$$\frac{\{(v_\perp R)_{\mathrm{PS}}\}}{R_0} = -2\eta_\parallel q^2 \frac{\mathrm{d}p/\mathrm{d}r}{B^2} \tag{1.28}$$

where the curly brackets denote the flux surface average. Consequently, the diffusion is larger by $2q^2\eta_\parallel/\eta_\perp$ than the classical value.

However, the high collisionality case is usually not relevant for tokamak core plasmas studied in this thesis and the neoclassical transport is described by the banana regime. Particles with $v_\parallel < \sqrt{2\epsilon}v_\perp$ are trapped on the low field side and can perform at least one bounce orbit before they are detrapped by collisions. The transition from trapped to passing requires a scattering angle of $\vartheta \sim \sqrt{\epsilon}$ in velocity space and thus the effective collision frequency for detrapping is ν/ϵ. Consequently, the condition for the banana regime is

$$\nu < \frac{\epsilon^{3/2} v_{\mathrm{th}}}{qR}, \tag{1.29}$$

i.e. the detrapping frequency is smaller than the bounce frequency $\omega_b = \sqrt{\epsilon}v_{\mathrm{th}}/(qR)$. Since the trapped particles have a radial orbit width $w_b \sim (q/\sqrt{\epsilon})\rho$, they have a larger step length for the diffusion process than the classical step length, the Larmor radius ρ. Taking into account that only the fraction $\sqrt{\epsilon}$ of the particles are trapped, the diffusion coefficient can be approximated as

$$D \sim \sqrt{\epsilon} w_b^2 (\nu/\epsilon) \sim \frac{q^2}{\epsilon^{3/2}}\nu\rho^2. \tag{1.30}$$

Again the diffusion is much larger than the classical value by a factor $q^2/\epsilon^{3/2}$.

The bootstrap current

Currents that are not driven externally, like the Pfirsch-Schlüter current, are called intrinsic currents. Intrinsic toroidal currents are of great interest for tokamak operation as the poloidal magnetic field requires a toroidal current that, in the absence of a intrinsic currents, must be driven by a central solenoid leading to a pulsed operation. The bootstrap current [11–13] is the most important intrinsic current and is briefly explained below.

Two trapped ions with the same energy and magnetic moment but with opposite parallel velocity will have orbits with a different averaged radius as one drifts outwards due to the ∇B drift while the other drifts inwards. If a radial density gradient exist the outer orbit will be less populated than the inner one and a flow parallel to the magnetic field arises due to the asymmetry in the parallel velocity distribution. Note that the flow of the electrons is antiparallel to

the ions as their ∇B drift is in the opposite direction. Thus, a current j_b called banana current is generated. It is given by

$$j_b \sim \frac{\epsilon^{3/2}}{B_p} T \frac{\mathrm{d}n}{\mathrm{d}r} \tag{1.31}$$

and is not the bootstrap current, or at least only part of it.

The dominant contribution turns out to be driven by the passing particles. The asymmetry in the velocity distribution of the trapped particles implies a discontinuity at the trapped-passing boundary. Collisions, which couple passing and trapped particles will remove the discontinuity and cause an asymmetry in the passing domain as well. While ions mostly collide with themselves, the electron-ion collisions are more important for electrons. Therefore, their velocity distribution is shifted not as much as that of the ions. The derivation of the ion and electron flows is omitted here and can be found for example in Ref. [13]. It is the difference in flow velocities between ions and electrons that yields the bootstrap current

$$j_{\mathrm{BS}} \sim \frac{\sqrt{\epsilon}}{B_p} T \frac{\mathrm{d}n}{\mathrm{d}r}, \tag{1.32}$$

which is a factor $1/\epsilon$ larger than the banana current.

1.2.2. Kinetic description of neoclassical transport

The exact calculation of the neoclassical flows is much more complex than the phenomenological discussion in the previous section and requires the kinetic treatment of the plasma. Neoclassical theory describes the equilibrium transport in the plasma. Therefore, the goal is to obtain the steady state distribution function f (i.e. $\partial f/\partial t = 0$) from the Vlaslov Fokker-Planck equation

$$\mathbf{v} \cdot \nabla f + \frac{Ze}{m} \left(\mathbf{E} + \mathbf{v} \times \mathbf{B}\right) \cdot \frac{\partial f}{\partial \mathbf{v}} = \mathcal{C}(f), \tag{1.33}$$

where $\mathcal{C}$ is the collision operator. With the distribution function the current or the transport across flux surface can be easily calculated. However, for multiple particle species, especially when considering heavy impurity ions which are only partly ionised, the solution of the kinetic equation is not straightforward.

The Hirshmann-Sigmar formalism [14] is probably the most commonly used way to obtain the neoclassical equilibrium and is also used in Chapter 2 even though impurities are not considered in this thesis. The formalism rewrites the kinetic equation as a set of flux surface averaged parallel balance equations in the reduced charge state description.

Following the more readable adaptation from Ref. [15] and considering only one charge state per species the set of equations will be briefly introduced here. The three balance equations ($\alpha = 1, 2, 3$) are

$$\{\mathbf{B} \cdot \nabla \cdot \mathbf{P}^a_\alpha\} = \{\mathbf{F}^a_\alpha \cdot \mathbf{B}\} + S^a_{\parallel,\alpha}, \tag{1.34}$$

for each species a and follow from taking the odd velocity moments $\{\int \mathrm{d}^3 v \; m_a \mathbf{B}\cdot\mathbf{v} L^{3/2}_{\alpha-1}(x_a^2) \cdots\}$ of the kinetic equation. Here $\mathbf{P}^a_\alpha$ is the viscosity tensor, $\mathbf{F}^a_\alpha$ the friction force and $S^a_{\parallel,\alpha}$ are the

source terms. The curly brackets $\{\cdots\}$ denote the flux surface average and the Laguerre polynomials $L_{\alpha-1}^{3/2}(x_a^2)$ are,

$$L_0^{3/2}(x_a^2) = 1, \tag{1.35}$$

$$L_1^{3/2}(x_a^2) = \frac{5}{2} - x_a^2, \tag{1.36}$$

$$L_2^{3/2}(x_a^2) = \frac{35}{8} - \frac{7}{2}x_a^2 + \frac{1}{4}x_a^4, \tag{1.37}$$

with $x_a = v/v_{\text{th},a}$ and $v_{\text{th},a}$ being the thermal velocity of species a. The three moments correspond to the force balance, the heat flux balance and the parallel balance of the next higher order term. The latter term has no direct physical interpretation but cannot be neglected when the bootstrap current and the radial fluxes are to be calculated accurately. There are several parallel source and sink terms that can be considered in $S_{\parallel,\alpha}^a$. The influence of an external electric field E that drives the Ohmic current is an integral part of neoclassical theory and is represented by $S_{E\parallel,\alpha}^a = Z_a n_a e\{\mathbf{E}\cdot\mathbf{B}\}$. Other sources like the momentum driven by neutral beam injection or a model term for anomalous transport can be added as well.

The friction forces are given by the velocity moments of the Collision operator

$$\mathbf{F}_\alpha^a = \int \mathrm{d}^3v\; m_a v L_{\alpha-1}^{3/2}(x_a^2)\mathcal{C}_a \tag{1.38}$$

and couple the equations for species a with the other species b as the Fokker-Plank Coulomb Collision operator C_a

$$C_a = \sum_b C_{ab}(f_a, f_b) \tag{1.39}$$

includes collisions with all other species b (including $b = a$).

Eq. 1.34 can be written in terms of parallel flows as well as friction and viscosity coefficients. The parallel friction forces are

$$\{\mathbf{F}_\alpha^a \cdot \mathbf{B}\} = \sum_b \sum_\beta l_{\alpha\beta}^{a,b} \hat{u}_\beta^b, \tag{1.40}$$

using the parallel friction coefficients $l_{\alpha\beta}^{a,b}$ and the normalised parallel flows $\hat{u}_\alpha^a$. The forces for each species and order have contributions from all other species b and orders β. The neoclassical viscosity is mainly connected to the friction between passing and trapped particles. Both move along the field but the poloidal flow of the passing particles is subject to friction with the particles trapped on the low field side, and is described by a parallel viscosity. The viscous forces are approximately given by

$$\{\mathbf{B}\cdot\nabla\cdot\mathbf{P}_\alpha^a\} = \{B^2\}\sum_\beta \hat{\mu}_{\alpha\beta}^a \hat{u}_{\theta,\beta}^a. \tag{1.41}$$

The poloidal components of the flow $\hat{u}_{\theta,\alpha}^a$ are damped by the parallel viscosity with the co-

efficients $\mu^a_{\alpha\beta}$. The poloidal flows have to be removed to solve the parallel balance equation, and, using that the fluid velocity is divergence free ($\nabla \cdot \mathbf{u} = 0$), are expressed via parallel flows using the force balance normal to the flux surface,

$$\left\{B^2\right\} \hat{u}^a_{\theta,\alpha} = \hat{u}^a_\alpha + S^a_{\theta,\alpha}, \tag{1.42}$$

where the sources for poloidal momentum and heat flow are given by the thermodynamic gradients and if present a radial electric field. The coefficients are complicated functions of the background distributions and collision operators and can be found for example in Ref. [15]. Using the expressions above, Eq. 1.34 becomes a set of three equations per species which can be solved to obtain the parallel flows. It has the general form

$$\mathbf{A} \cdot \hat{\mathbf{u}}^a = \sum_b \mathbf{\Lambda}(\hat{\mathbf{u}}^b) + \mathbf{S}^a, \tag{1.43}$$

with $\hat{\mathbf{u}}^a = (\hat{u}^a_1, \hat{u}^a_2, \hat{u}^a_3)$, i.e. each component of the vectors represents an order of the balance equation. The tensor $\mathbf{A}$ and the vectors for the friction $\mathbf{\Lambda}(\hat{\mathbf{u}}^b)$ are determined by the friction and viscosity coefficients. The source term vector is given by the thermodynamic gradients and the external $S^a_{\parallel,\alpha}$ terms considered. In this form the set of equations essentially becomes a linear algebra problem which can be solved numerically. For more details, the reader is again referred to Ref. [15]. Once the flow velocities are known, the current and radial transport in the neoclassical equilibrium can be directly calculated, e.g. the parallel current is $\{\mathbf{J} \cdot \mathbf{B}\} = \sum_a Z_a e n_a \hat{u}^a_1$.

1.3. Drift wave turbulence

Early tokamak experiments quickly demonstrated that the neoclassical theory was not able to explain the confinement times achieved. Energy and particle transport are one or two orders of magnitude larger then predicted by neoclassical theory. This transport, originally termed "anomalous transport", is nowadays understood to be caused by "drift wave" microturbulence driven by the large temperature and density gradients in the plasma. Turbulent heat flux is recognised as the major loss mechanism for tokamak fusion plasmas. For an in-depth discussion of drift waves and associated instabilities the reader is referred to Ref. [16].

Here, we focus on the ion temperature gradient (ITG) instability [17] which is expected to be the dominant instability under standard conditions. Also, the turbulence studied in the later chapters of this thesis is dominated by the ITG instability. The physical mechanisms behind the ITG are explained in Sec. 1.3.1 and then the self-regulating zonal flows along with their impact on the nonlinear stability of turbulence are discussed in Sec. 1.3.2.

1.3.1. The ion temperature gradient instability

In contrast to the large scale instabilities described by MHD, microturbulence has characteristic wavelengths of the scale of the Larmor radius, and thus the ion and electron dynamics have to be considered separately on this scale, making a single fluid model unsuitable. The disparate dynamics interact through the electrostatic force, working against the local charge disparity, trying to restore quasi-neutrality in the plasma. Quasi-neutrality is an intrinsic feature of any plasma. Despite the ability of positively and negatively charged particles to move independently there is no large scale charge separation, as large electric fields would build up otherwise.

A simplified geometry, neglecting the curvature effects of the toroidal geometry, called slab geometry, can be used to qualitatively understand drift waves and instabilities. An annulus with the inner radius r_s is rolled out into a slab and a Cartesian coordinate system is used as shown in Fig. 1.7. The x direction denotes the radial distance from the flux surface at radius r_s, z is in the direction of the magnetic field on the flux surface, approximately in the toroidal direction and y is perpendicular to the field line, approximately in the poloidal direction. Consider an ion density perturbation $\tilde{n}_i \propto \exp[i(k_y y - \omega t)]$ of the background density n_0 which has a gradient in the negative $x-$direction due to the radial confinement. Due to their small mass the electrons react much faster to the perturbation than the ions and the cold ion approximation is used. In this case the ion thermal motion, and ion pressure is neglected. Confined by the field line, the electrons can move parallel to the magnetic field ($z-$direction) to restore quasi-neutrality. The change in electron pressure $p_e = (n_{e0}+\tilde{n}_e)T_e$ due to the electron density perturbation $\tilde{n}_e$ has to be balanced by an electric field

$$\frac{\partial}{\partial z} p_e = -(n_{e0} + \tilde{n}_e) e E_z, \tag{1.44}$$

Introducing the perturbed potential $\tilde{\phi}$ and assuming a constant electron temperature T_e on the

flux surface Eq.1.44 becomes

$$T_e \frac{\partial}{\partial z}\tilde{n}_e = n_{e0} e \frac{\partial}{\partial z}\tilde{\phi}, \tag{1.45}$$

where the second order perturbation $\propto \tilde{n}_e\tilde{\phi}$ has been neglected. Integrating yields the adiabatic electron response

$$\tilde{n}_e = n_{e0}\frac{e\tilde{\phi}}{T_e}. \tag{1.46}$$

As the electron density perturbation matches that of the ions, the perturbed potential causes an electric field in the $y-$direction from the dense to the less dense regions. The resulting E×B-drift is out of phase with the density perturbation, and brings the higher density plasma from the inside ahead of the density maximum of the wave, resulting in a propagation in the vertical direction, but no instability. Thus, the oscillating density and potential perturbation propagates in the $y-$direction. The process is shown in Fig. 1.8 and is a stable drift wave at this point.

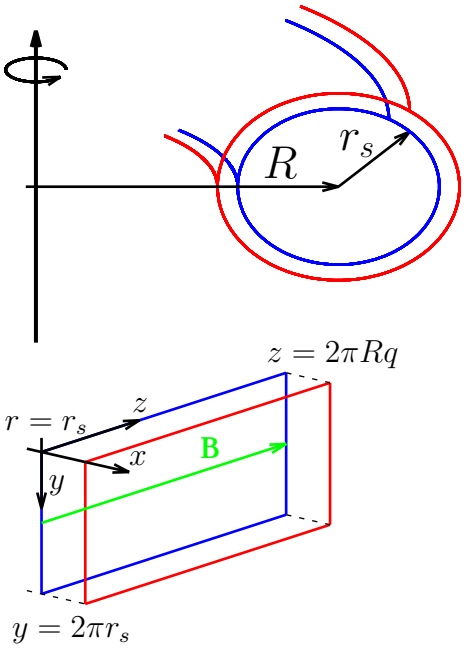

Figure 1.7. The slab geometry: An annulus is rolled out, neglecting the effects of toroidal geometry, to form a Cartesian coordinate system.

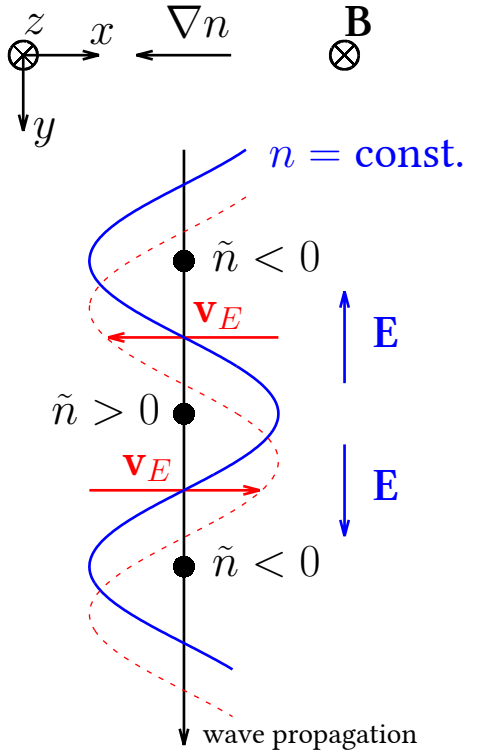

Figure 1.8. An initial density perturbation causes an oscillating density and potential perturbation, propagating in the $y-$direction. The dashed red line shows the constant density surface at a later point in time.

However, with the right phase shift between density and potential perturbation, a positive feedback loop will further increase (decrease) the density in the dense (less dense) regions, forming an exponentially growing instability driven by the background density gradient. Such an instability is possible if friction is considered in the electron response and is called dissipative instability.

In the core of the plasma the coupling to the temperature perturbation is more important than the mechanism discussed above. The coupling of density and temperature perturbations due to the curvature drift in tokamaks leads to the ITG-instability. As the strength of the ∇B-drift depends on the particle velocity (see Eq. 1.6), which scales with the thermal velocity $v_{\mathrm{th}} = \sqrt{2T/m}$, a temperature perturbation leads to a modulation of the averaged drift velocity, which in turn compresses the ions, generating a density perturbation. Similar to the drift wave mechanism discussed above, the electrons move to restore quasi-neutrality and generate an electric field from the dense to the less dense regions. The resulting E×B-drift can stabilise or destabilise the perturbation depending on the orientation of temperature and magnetic induction gradient (see Fig. 1.9). At the high field side where the gradients point in opposite directions the E×B-drift causes hotter plasma to flow towards the cold areas and vice versa. However, at the low field side where the gradients are in the same direction, the temperature perturbation is further enhanced, leading to an unstable ITG mode. The instability leads to an exponential growth of the modes, until they reach an amplitude where nonlinear interac-

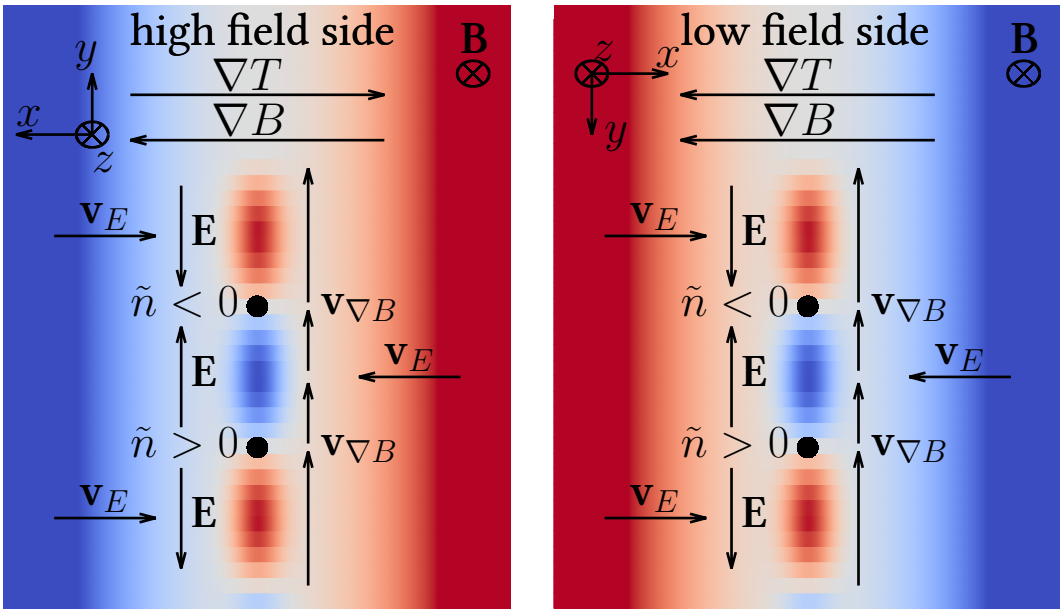

Figure 1.9. Schematic explanation of the ITG-instability. A temperature perturbation causes an ion density perturbation due to the temperature dependence of the ∇B-drift. The adiabatic electron response to the perturbation causes an electric field from the dense to the less dense regions. The resulting E×B-drift stabilises the temperature perturbation at the high field side (left) but further enhances it at the low field side. Thus, the ITG-instability, driven by the temperature gradient, can form at the low field side.

tions can no longer be neglected, resulting in a turbulent state. It is this turbulent state that is responsible for the degraded confinement of the tokamak.

A critical temperature gradient is required for the ITG-mode to become unstable. Depending on the complexity of the model, different thresholds are reported in the literature: the linear threshold, the nonlinear threshold [18] and the finite-heat-flux-threshold [19]. The nonlinear turbulence calculation finds an up-shift compared with the linear theory, which is due to turbulence suppression by zonal shear flows. A more recent discovery is the finite-heat-flux-threshold which is even higher, and is related to structure formation in the zonal flow. Zonal flows and their structure formation will be discussed in more detail in the following section as they play an integral role in the Chapters 4 and 5.

1.3.2. Zonal flows

Zonal flows are latitude parallel, toroidally symmetric shear flows. The collective flow pattern only depends on the radial coordinate and band-like structures are formed as sketched in Fig. 1.10. Originally a meteorological term, it is used in plasma physics due to the similarity to the oceanic and atmospheric flows, with popular examples being jet streams or the distinct belt structure of the Jovian atmosphere. Zonal flows exhibit a self-regulating character as they work to reduce their drive, in the above example a temperature or pressure difference in the atmosphere. In laboratory fusion plasma experiments, turbulence drives a zonal flow through nonlinear coupling. In turn, the zonal flow reduces the turbulence through eddy shear stabilisation. A thorough review of plasma zonal flows and their interaction with drift waves, sometimes referred to as "drift wave-zonal flow turbulence" is given in Ref. [20]. However, the interaction of zonal flows with turbulence is an active research topic and recent findings suggest that the previously advocated predator-prey model does not capture all relevant effects [21–23]. Furthermore, structure formation in the zonal flow, which will be discussed later in this section, can critically modify the effect of zonal flows on turbulence generation [19, 24].

Zonal flows are driven by turbulent Reynolds stresses [25]. Considering the flux-surface averaged momentum balance equation of an incompressible fluid and splitting the velocity $v = \bar{v} + \tilde{v}$ in a mean and a fluctuating part, the mean poloidal flow (the zonal flow v_{zf}) is given by

$$\frac{\partial}{\partial t} v_{\mathrm{zf}} = - \left\{ \frac{\partial}{\partial r} (\tilde{v}_r \tilde{v}_\theta) \right\}, \tag{1.47}$$

where $\{ \cdots \}$ denotes the average over the flux surface and $\tilde{v}_r, \tilde{v}_\theta$ are the radial and poloidal velocity components of the turbulent velocity. For isotropic turbulence, i.e. perfectly circular turbulent vortices, the Reynolds stress $(\tilde{v}_r \tilde{v}_\theta)$ vanishes under the flux surface average due to the symmetry. A finite Reynolds stress can, for instance, occur through the modulation instability [26–30], and has been observed in experiments [31]. In a heuristic picture the modulation instability works as follows: A small tilt (modulation) of the turbulent vortex breaks the symmetry, which drives a zonal flow further shearing the vortex. An exponential growth of the zonal flow results, that continues until its amplitude is sufficiently large for damping mechanisms to balance the growth. Several damping mechanisms saturate the zonal flows,

including collisional damping [21, 32] and Kelvin Helmholtz tertiary instabilities [33]. A new mechanism, the damping of zonal flows through turbulent momentum transport is introduced in Chapter 4.

The zonal flow is associated with a zonal electrostatic potential ϕ_{zf},

$$v_{\mathrm{zf}} = \frac{B_t}{B^2}\frac{\partial \phi_{\mathrm{zf}}}{\partial r} \approx \frac{1}{B}\frac{\partial \phi_{\mathrm{zf}}}{\partial r}. \tag{1.48}$$

Since it is an E×B flow, the terms E×B shear flow or E×B shearing are commonly used for zonal flows. The radial variation of the zonal flow, the E×B shear rate $\omega_{E\times B}$,

$$\omega_{E\times B} = \frac{\partial v_{\mathrm{zf}}}{\partial r} = \frac{1}{B}\frac{\partial^2 \phi_{\mathrm{zf}}}{\partial r^2} \tag{1.49}$$

is an important measure for the ability of zonal flows to regulate or suppress turbulence. The turbulence suppression by zonal flows is attributed to the shear decorrelation of the turbulent fluctuations and used to explain the high confinement regime (H-mode [34]) reported in tokamaks [35–37]. Using a simplistic picture, shown in Fig. 1.11, the turbulent eddies are subject to the radially varying zonal flow leading to a tilted elongation. If they are sheared sufficiently, the vortices will break into smaller ones, reducing the radial correlation length of turbulent structures and thus reducing transport. In this picture it is easy to see that quickly time varying zonal flows are much less effective in suppressing turbulence than slowly varying ones, because the flow pattern changes before the eddies are sufficiently distorted [38]. Therefore, even though the instantaneous value of the shearing rate is typically dominated by the quickly fluctuating components the mean shear rate is the interesting quantity. The above discussion

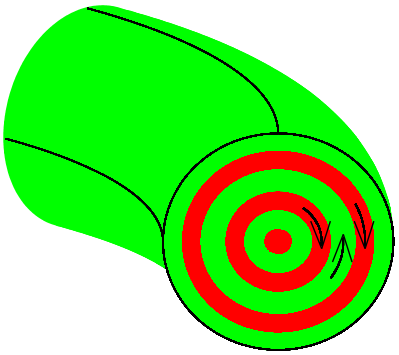

Figure 1.10. Schematic representation of zonal flows in a tokamak.

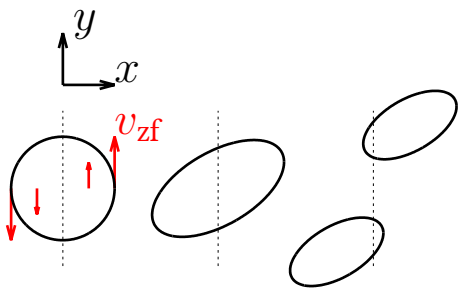

Figure 1.11. The zonal flow shears the turbulent eddies, leading to tilted elongation until they break in smaller eddies.

can be reduced to a rule of thumb for turbulence suppression. Turbulence suppression will occur if the mean E×B shearing rate is comparable to or higher than the growth rate γ of the dominant instability (with the latter calculated without taking shearing into account),

$$\omega_{E\times B} \approx \gamma_{\mathrm{ITG}}, \tag{1.50}$$

which is the so-called Waltz-criterion [39, 40].

A recent milestone in our understanding of drift wave-zonal flow turbulence is the discovery of meso-scale structures, called staircases, in the E×B shear flow (see Fig. 1.12) [24, 41, 42], and their ability to partially or completely suppress turbulence [19, 43]. E×B staircases lead to a further up-shift of the temperature gradient threshold for turbulence, the so-called finite heat flux threshold. This threshold is qualitatively different to the nonlinear threshold, as the heat flux does not decline smoothly but jumps from a finite value to zero.

For a thorough discussion of the appearance and features of E×B staircases the reader is referred to Ref. [24]. Here, the most important aspects for the purposes of this thesis will be briefly summarised. The E×B staircase is a near-marginal pattern, i.e. it only appears close to the instability threshold. However, this is a likely operating regime for current and future tokamaks and indications of staircases have been reported in the Tore Supra tokamak, making

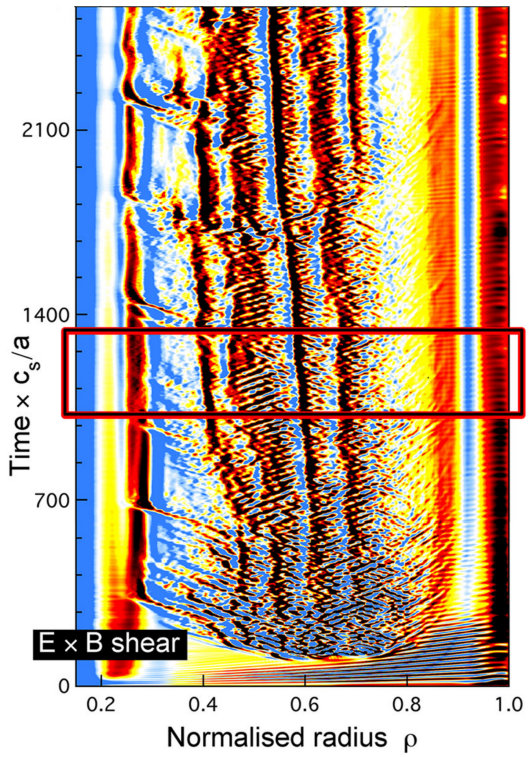

Figure 1.12. The structure formation of the E×B shear in a global gyrokinetic simulation. Figure from Ref. [24].

zonal flow structure formation highly relevant for understanding turbulent transport in fusion reactors. The radial heat transport for plasmas close to stability is dominated by avalanches. They mostly originate in the narrow low shear regions of the staircase structure and and propagate through the high shearing rate regions until they reach the so called bipolar shear layer, a region in which the shearing rate quickly changes sign. The latter acts as a micro-barrier hindering large scale avalanches, thus reducing transport. Staircase structures are long-lived and have a radial extent of several ten Larmor radii. While the overall magnitude of zonal flow shear is not modified, their distinct structure allows for large connected radial regions with high shear fulfilling the Waltz-criterion and effectively suppressing turbulence.

1.4. Gyrokinetic theory

The description of a tokamak plasma featuring about 10^{22} particles and requiring the simultaneous study of large range of length and time scales provides a formidable challenge. Particles gyrate around the magnetic field line with a Larmor radius of a few millimetres while the device size is of several meters. The temporal scale covers even more orders of magnitude: the fast cyclotron frequency $\omega_{c,i} \sim 10^8 \mathrm{s}^{-1}$, the frequency of one toroidal revolution called transit frequency $\omega_{T,i} = v_{\mathrm{th}}/(qR) \sim 10^5 \mathrm{s}^{-1}$, the collision frequency $\nu_{ii} \sim 10^{-3}\omega_{T,i} \sim 100\mathrm{Hz}$, and the energy confinement time of a few seconds[1]. As discussed in Sec. 1.3.1, a fluid model can not accurately describe microinstabilities, and thus turbulent transport, which is the major loss channel in tokamaks. Consequently, a sophisticated theory is required to make the theoretical study of turbulence numerically feasible. The gyrokinetic description uses the large scale separation to analytically average over the gyromotion, while retaining all physical effects which are believed to be relevant for microturbulence. While the underlying idea is simple, the theoretical formalism and numerical implementation prove to be quite complex and a more general review can be found in Ref. [45], while Refs. [46] and [47] provide more details on the analytical formalism and the numerical implementation as well as the comparison to experiments. Here, the kinetic model and ordering is outlined and, skipping the tedious analytical derivation, the local gyrokinetic equation is given.

Tracing every particle motion of each species is not feasible even with modern (or future) supercomputers. Therefore, a kinetic theory is used to describe the plasma with a particle distribution function $f_s(\mathbf{q}, \mathbf{p})$ for each species s in the six-dimensional phase space given by the particle position $\mathbf{q}$ and momentum $\mathbf{p}$. The fusion plasma, especially hot plasmas with $T \sim 10$ keV, can be considered weakly coupled, as the density is low and the kinetic energy is much larger than the average potential energy between particles due to the Coulomb interaction. Therefore, all particle interactions are neglected except two particle Coulomb collisions, which are treated by a collision operator $\mathcal{C}(f_{s'}, f_s)$. Indeed, studies of microturbulence often use a collisionless plasma model, as the collision frequency is much lower than the frequency of turbulent fluctuations and thus collisions do not have a critical impact on many aspects of turbulence. The time evolution of the particle distribution function is given by the Boltzmann equation,

$$\frac{\mathrm{d}f_s}{\mathrm{d}t} = \frac{\partial f_s}{\partial t} + \{f_s, \mathcal{H}_s\} = \mathcal{C}(f_{s'}, f_s) \tag{1.51}$$

or the Vlaslov equation when neglecting collisions

$$\frac{\partial f_s}{\partial t} + \{f_s, \mathcal{H}_s\} = 0 \tag{1.52}$$

The curly brackets $\{\cdot, \cdot\}$ denote the Poisson bracket for the canonical coordinates $(\mathbf{q}, \mathbf{p})$

$$\{f, \mathcal{H}\} = \frac{\partial f}{\partial q_j}\frac{\partial \mathcal{H}}{\partial p_j} - \frac{\partial f}{\partial p_j}\frac{\partial \mathcal{H}}{\partial q_j} \tag{1.53}$$

[1] All magnitude approximations are made for deuterium ions in an expected ITER scenario [44].

and $\mathcal{H}_s$ is the Hamiltonian of the collisionless single particle motion

$$\mathcal{H}_s(\mathbf{q}, \mathbf{p}) = \frac{1}{2m_s} |\mathbf{p} - Z_s e\mathbf{A}|^2 + Z_s e\phi, \tag{1.54}$$

where $\mathbf{A}$ is the vector potential for the magnetic field $\mathbf{B} = \nabla \times \mathbf{A}$ and ϕ the electrostatic potential. The plasma charge density ϱ and current $\mathbf{J}$ are given by summing the respective velocity moments of the distribution function for each species

$$\varrho = \sum_s Z_s e \int \mathrm{d}^3 p \, f_s, \tag{1.55}$$

$$\mathbf{J} = \sum_s Z_s e \int \mathrm{d}^3 p \, \mathbf{v} f_s, \tag{1.56}$$

where $\mathbf{v} = (\mathbf{p} - Z_s e\mathbf{A})/m_s$ is the particle velocity. Charge density and current are sources in the Maxwell equations and the latter have to be solved to obtain the electrostatic potential and vector potential used in the Hamiltonian of the Vlaslov equation. While being considerably more elegant than a Newton-Maxwell description, the Vlaslov-Maxwell system is not suitable to study low frequency phenomena, i.e. slow compared to the cyclotron frequency, like drift waves due to the extreme time scale discrepancy. This is where the gyrokinetic approach is required.

Modern gyrokinetic theory [46] is based on the Hamiltonian or Lagrangian formalism paired with the Lie perturbation theory [48, 49]. This approach allows to correctly study collisionless turbulent dynamics, keeping the conservation and symmetry properties of the system.

The starting point of gyrokinetic theory is to introduce an ordering based on the scale separation discussed above and the physical properties of drift waves to develop an expansion of the kinetic equation using a smallness parameter. While the temporal, spatial and perturbation to background scale separations are not identical, a single smallness parameter, the normalised ion gyro radius $\rho_* = \rho_i/R$ is usually employed and provides a good description of large aspect ratio tokamak core turbulence studied here. Microturbulence is considered to obey the ordering [47]:

$$\frac{\omega}{\omega_{c,s}} \sim \frac{k_\parallel}{k_\perp} \sim \frac{v_D}{v_{\mathrm{th},s}} \sim \frac{\delta n_s}{n_0} \sim \frac{B_1}{B_0} \sim \frac{\rho_s}{L_n} \sim \rho_*, \tag{1.57}$$

where ω is the characteristic frequency of turbulence, $k_\parallel$ and $k_\perp$ are the components of the wave vector, parallel and perpendicular to the magnetic field respectively, v_D is the drift velocity, δn the density perturbation, n_0 the equilibrium density, B_0 the background magnetic field, B_1 the perturbed field and finally $L_n = |\nabla \ln n_0|$ is the characteristic length scale of the background density. Because the normalised Larmor radius is $\rho_* \sim 10^{-3}$ for current machines and even smaller for a much larger actual power plant, standard gyrokinetic theory only considers terms up to the first order in ρ_*, but higher order terms can be included as the gyrokinetic formalism is in principle correct up to an arbitrary order in ρ_*.

Two transformations the guiding-centre transform [50–53] and the gyrocentre transform [54–57] are employed. The guiding-centre transform allows to describe the particle using

its guiding-centre position, the gyroangle α which determines the actual position, the velocity parallel to the magnetic field, and the magnetic moment. Taking advantage of the scale separation the gyrocentre transform allows for an average over the gyromotion, i.e. eliminates the gyroangle. This also removes high frequency phenomena from consideration like Langmuir waves, which are believed to be not important for turbulence, allowing the study of the relevant effects [58, 59]

While reducing the demands on the time resolution by roughly three orders of magnitude (and even more for electron dynamics), the gyrocentre transform also reduces to the dimensionality of the problem to a 5D phase space. The rigorous derivation is omitted here and can be found in Ref. [46].

The gyrokinetic equation for the time evolution of the gyrocentre density distribution function $\bar{f}_s(\mathbf{X}, v_\parallel, \mu)$ is given by

$$\frac{\partial \bar{f}_s}{\partial t} + \dot{\mathbf{X}} \cdot \nabla \bar{f}_s + \dot{v}_\parallel \frac{\partial \bar{f}_s}{\partial v_\parallel} = \mathcal{C}(\bar{f}_{s\prime}, \bar{f}_s), \tag{1.58}$$

where $\mathbf{X}$ is the gyrocentre position, $v_\parallel$ the parallel velocity, and μ the magnetic moment, which is an adiabatic invariant, i.e. $d\mu/dt = 0$. Note that turbulence is on the scale of the Larmor radius, therefore the local variation of the fields over the gyromotion has to be considered in the averaging process of the gyrocentre transform. Neglecting magnetic field perturbations in the low plasma β limit, the Maxwell equations reduce to the solution of the Poisson equation of electrostatics. Gyrokinetics is valid for length- and timescales for which quasi-neutrality is satisfied. Therefore, the local charge density is zero and the Poisson equation is not suited to find the electric field. The gyrokinetic Poisson equation is actually derived from the constraint of quasi-neutrality

$$\sum_s Z_s e n_s(\mathbf{x}) = 0. \tag{1.59}$$

However, this requires the actual particle position $\mathbf{x}$ in physical phase space $(\mathbf{x}, \mathbf{v})$, whereas the distribution function is given in gyrocentre phase space $(\mathbf{X}, v_\parallel, \mu)$. The gyrokinetic quasi-neutrality condition

$$\bar{\rho}(\mathbf{X}) + \rho_{\text{pol}}(\mathbf{X}) = 0 \tag{1.60}$$

is expressed via the gyrocentre charge density

$$\bar{\rho} = \sum_s Z_s e \bar{n}_s = \sum_s Z_s e \int \mathrm{d}^3 v \ \bar{f}_s \tag{1.61}$$

and the gyrocentre polarisation density

$$\rho_{\text{pol}} = \sum_s Z_s e \int \mathrm{d}^3 v \ \left(\langle \mathcal{T} \bar{f}_s \rangle - \bar{f}_s \right). \tag{1.62}$$

The angle brackets $\langle \cdots \rangle$ denote the average over the gyroangle and the operator $\mathcal{T}$ transforms the distribution function from gyrocentre phase space back to physical phase space. The polar-

isation density is used to describe the difference between the actual charge density at a given point in physical space and the charge density read from the gyrocentre density. The correction to the density can be understood as a Boltzmann response $n_{\mathrm{pol}} \propto \exp[-Ze\delta\phi/T]$ as the particles are subject to the variation $\delta\phi = \phi - \langle\phi\rangle$ over the course of their gyromotion. The gyrokinetic Poisson equation up to first order in ρ_* is given by [47]

$$\sum_s \int \mathrm{d}^3 v \ \left[Z_s e \langle \delta f_s \rangle + \frac{Z_s e^2}{T_s} F_{M,s} \left(\phi - \langle\langle \phi \rangle\rangle \right) \right] = 0 \tag{1.63}$$

and is used to calculate the potential at a given point $\mathbf{x}$ in real space. It is derived from Eq. 1.60 and the potential enters through the pull-back operator $\mathcal{T}$. Here, the gyrocentre distribution $\bar{f}_s = \delta f_s + F_{M,s}$ is split into the first order perturbation δf_s and the Maxwellian background $F_{M,s}$. The first term of Eq. 1.63 is the gyrocentre charge density while the second represents the linearized polarisation density.

The equations can be subject to further approximations (see Secs. 1.4.2-1.4.3) and the exact equations solved in simulations for this thesis will be given in Sec. 1.5.

1.4.1. Field Aligned Coordinates

The gyrokinetic study of turbulence is best done using a specialised coordinate system. The benefits of a field-aligned coordinate system are easy to see, when considering the length scale differences of the dynamics parallel and perpendicular to the field line. A high resolution grid is needed perpendicular to the field to cover the dynamics on the scale of the Larmor radius but a low resolution grid is sufficient parallel to the field, where variations are on the scale of the system size. If the coordinate system is not field aligned, one has to retain the Larmor radius resolution in all three coordinates, which significantly increases the computational costs.

Here, the field aligned Hamada coordinates (ψ, ζ, s) [60, 61] are presented and the necessary transformations starting from the known orthogonal toroidal coordinate system (ψ, θ, φ) are derived in detail. θ, φ are the poloidal and toroidal angle respectively and ψ the radial coordinate. The derivation works for any arbitrarily shaped magnetic field configuration, provided it is toroidally symmetric. Then, the magnetic field can be written as

$$\mathbf{B} = RB_t \nabla\varphi + \nabla\varphi \times \nabla\Psi, \tag{1.64}$$

where $B_t = \mathbf{B} \cdot \nabla\varphi / |\nabla\varphi| = R\mathbf{B} \cdot \nabla\varphi$ is the toroidal magnetic field strength, R the local major radius and Ψ the poloidal flux. The radial coordinate $\psi = \psi(\Psi)$ is a flux surface label, i.e. ψ =const. on a given flux surface. For the purposes of this thesis, where circular flux surfaces are assumed it is convenient to directly use the minor radius as the radial coordinate. The goal is to have straight magnetic field lines and a coordinate s aligned to the field line. Furthermore, to keep using the benefits of the toroidal symmetry all quantities independent of the toroidal angle φ need to be independent of the new "toroidal" coordinate ζ. The transformation is split into two steps

$$(\psi, \theta, \varphi) \to (\psi, s, \gamma) \to (\psi, \zeta, s) \tag{1.65}$$

and the process is illustrated in Fig. 1.13. First, the poloidal and toroidal angle are replaced by $s = s(\psi, \theta)$ and $\gamma = \gamma(\psi, \theta, \varphi)$ with the goal to get straight field lines on a flux surface (ψ =const.), i.e.,

$$\frac{\mathrm{d}\gamma}{\mathrm{d}s} = \frac{B^\gamma}{B^s} = q(\psi), \tag{1.66}$$

where q is the safety factor. Therefore, the contravariant components of the magnetic field have to be functions of only the radial coordinate ψ

$$B^s = B^s(\psi), \qquad B^\gamma = B^\gamma(\psi). \tag{1.67}$$

Note that the magnetic field configuration already demands $\mathbf{B} \cdot \nabla\psi = B^\psi = 0$. The transformation for s is obtained by taking

$$B^s = \mathbf{B} \cdot \nabla s = \mathbf{B} \cdot \nabla\theta \frac{\partial s}{\partial \theta} \tag{1.68}$$

and integrating the expression in θ

$$s = B^s \int_0^\theta \frac{1}{\mathbf{B} \cdot \nabla\theta'} \mathrm{d}\theta'. \tag{1.69}$$

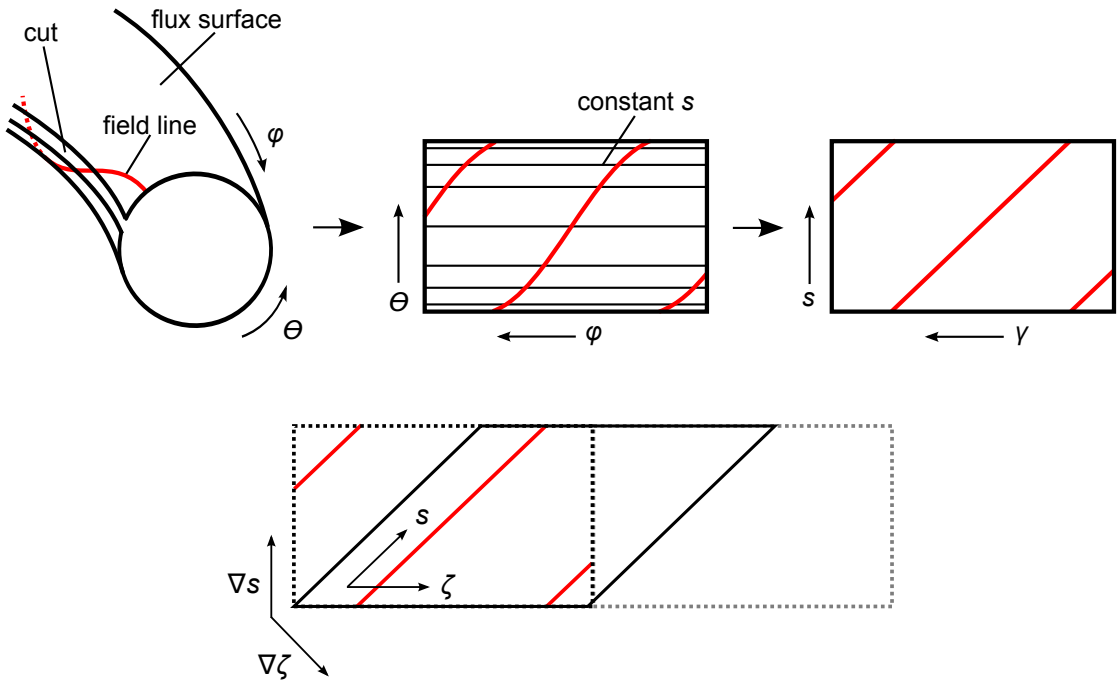

Figure 1.13. Illustration of the transformation from toroidal to field aligned Hamada coordinates [Arne Weikl, personal communication, March 13, 2019]. The field lines are straightened and aligned to the $s-$coordinate.

Demanding that $s = [-1/2, 1/2]$ corresponds to one poloidal turn, Eq. 1.69 yields,

$$1 = B^s \int_0^{2\pi} \frac{1}{\mathbf{B} \cdot \nabla\theta'} \mathrm{d}\theta'. \tag{1.70}$$

and inserting back in Eq. 1.69 gives the transformation for s

$$s(\psi, \theta) = \int_0^{\theta} \frac{1}{\mathbf{B} \cdot \nabla\theta'} \mathrm{d}\theta' \Big/ \int_0^{2\pi} \frac{1}{\mathbf{B} \cdot \nabla\theta'} \mathrm{d}\theta'. \tag{1.71}$$

Choosing that $\gamma = [0, 1]$ corresponds to one toroidal revolution, the ansatz

$$\gamma(\psi, \theta, \varphi) = \frac{\varphi}{2\pi} + g(\theta, \psi), \tag{1.72}$$

with the subsidiary function g, is used to find the expression for γ. Then, the contravariant component B^γ is given by

$$B^\gamma = \mathbf{B} \cdot \left(\nabla\varphi \frac{\partial\gamma}{\partial\varphi} + \nabla\theta \frac{\partial\gamma}{\partial\theta} \right) = \frac{B_t}{2\pi R} + \mathbf{B} \cdot \nabla\theta \frac{\partial g}{\partial\theta}. \tag{1.73}$$

Integrating in θ allows to determine g,

$$g = \int_0^{\theta} \frac{1}{\mathbf{B} \cdot \nabla\theta'} \left(B^\gamma - \frac{B_t}{2\pi R} \right) \mathrm{d}\theta'. \tag{1.74}$$

Demanding that g is poloidally periodic, i.e.

$$0 = \int_0^{2\pi} \frac{1}{\mathbf{B} \cdot \nabla\theta'} \left(B^\gamma - \frac{B_t}{2\pi R} \right) \mathrm{d}\theta', \tag{1.75}$$

yields an expression for B^γ

$$B^\gamma = \oint \frac{B_t}{2\pi R} \frac{\mathrm{d}\theta'}{\mathbf{B} \cdot \nabla\theta'} \Big/ \oint \frac{\mathrm{d}\theta'}{\mathbf{B} \cdot \nabla\theta'} = \oint \frac{B_t}{2\pi R} \mathrm{d}s = \left\{ \frac{B_t}{2\pi R} \right\}. \tag{1.76}$$

The curly brackets denote the average over the flux surface $\{Q\} = \oint Q \mathrm{d}s$. Inserting Eqs. 1.74 and 1.76 in 1.72 and using that $B_t \propto 1/R$, i.e. $RB_t = \text{const.}$ to rewrite the expression yields the transformation for γ

$$\gamma(\psi, \theta, \varphi) = \frac{\varphi}{2\pi} + \frac{RB_t}{2\pi} \int_0^{\theta} \left(\left\{ \frac{1}{R^2} \right\} - \frac{1}{R^2} \right) \frac{\mathrm{d}\theta'}{\mathbf{B} \cdot \nabla\theta'}. \tag{1.77}$$

The coordinates (ψ, γ, s) are the Hamada coordinates but they are not yet field aligned. The second transformation $(\psi, s, \gamma) \to (\psi, \zeta, s)$ aligns the $s-$coordinate with the magnetic field line

$$\mathbf{B} \cdot \nabla = B^s \frac{\partial}{\partial s} \tag{1.78}$$

or equivalently $B^\psi = B^\zeta = 0$. The condition $B^\zeta = 0$ translates to

$$B^\gamma \frac{\partial \zeta}{\partial \gamma} + B^s \frac{\partial \zeta}{\partial s} = 0. \tag{1.79}$$

It is easy to verify that the linear transformation

$$\zeta = qs - \gamma \tag{1.80}$$

satisfies Eq. 1.79 as $q = B^\gamma / B^s$. Note that the transformation flips the sign of the toroidal angle. Therefore, the right handed field aligned Hamada coordinate system is (ψ, ζ, s).

All transformations depend on the background magnetic field **B**. Therefore, the magnetic field configuration has to be specified in simulations. While it is possible to get the exact equilibrium field by solving the Grad-Shafranov equation [10] for a specific reactor experiment, this process is not only cumbersome but also further impedes comparability of the results within an already vast parameter space. Furthermore, the shaped plasmas used in experiments usually require a higher numerical resolution to obtain a similar accuracy compared with a simplified equilibrium. Therefore, several approximations are commonly used for high aspect ratio core plasma turbulence.

Most notably are the s–α geometry and the *circular geometry*, which both feature concentric circular flux surfaces. The s–α geometry is the crudest model that still features trapped particles, keeping only the lowest order of the expansion in the inverse aspect ratio ϵ. The poloidal variation up to the first order in ϵ is only kept for the magnetic field strength and neglected ($\epsilon \to 0$) for all other quantities[2]. Despite its limitations, significant quantitative differences to a MHD equilibrium and inconsistency in the ϵ ordering [62], the s–α geometry is regularly used due to its prevalence in the literature.

The circular geometry retains the full ϵ dependence of all geometric quantities and thus provides a significant improvement to the s–α model. However, it is not an exact solution of the the Grad-Shafranov equation as it assumes concentric circular flux surfaces, i.e. the Shafranov-shift $\propto \epsilon^2$ [63], which displaces the flux surface centre, is neglected. Even though it can be considered sufficient for the turbulence studied in this thesis [62].

In the circular geometry the field aligned coordinates are

$$s = \frac{1}{2\pi} \left(\theta + \epsilon \sin \theta \right), \tag{1.81}$$

$$\zeta = -\frac{\varphi}{2\pi} + \frac{q}{\pi} \arctan\left(\sqrt{\frac{1-\epsilon}{1+\epsilon}} \tan \frac{\theta}{2} \right) \tag{1.82}$$

and the minor radius is used as the radial coordinate.

[2] The most common simulation parameter set, the Cyclone Base Case, uses $\epsilon = 0.19$.

1.4.2. Local flux tube limit

Nonlinear gyrokinetic simulations are computationally very expensive, especially so called global simulations which cover a large radial extent of the torus. The local flux tube limit uses the scale separation in the gyrokinetic ordering to provide a model which makes computer simulations more feasible. All simulations in this thesis are flux tube simulations, which still allow for the study of physical mechanisms and predicting the magnitude of transport phenomena.

The simulation domain is reduced to a radially thin region, the flux tube, confined by flux surfaces. The large scale separation allows the choice of a radial extend L_ψ of the domain which satisfies

$$\epsilon R \gg L_\psi \gg \rho. \tag{1.83}$$

The domain is much smaller than the system size and the background quantities can be taken to be constant on this scale. Yet, the characteristic length scale of turbulence, the Larmor radius, is again much smaller and it is assumed that the key features of plasma turbulence are not affected by the size of the simulation domain. This limit is valid for small $\rho_* = \rho/R$ and the smallness of ρ_*, implied by Eq. 1.83, also suggests the use of the δf formalism, $f = \delta f + F_M$, i.e. the distribution function can be decomposed in a time independent Maxwellian background distribution and the turbulent perturbation δf which is one order smaller in ρ_*, $\delta f \sim \rho_* F_M$. Higher order perturbations are neglected. Note that while background quantities are evaluated at the flux surface in the centre of the flux tube and are constant over the simulation domain they still have a radial gradient which is also constant across the domain. The background density and temperature gradients are retained as linear drive terms of the turbulence.

Since there is no radial variation in the background, the turbulence is homogeneous and periodic radial boundary conditions can be used, provided the correlation length of the turbulence is smaller than the computational domain [64]. Due to the toroidal symmetry, homogeneous turbulence can also be assumed in the binormal (ζ) direction. Periodic boundary conditions allow to reduce the simulation domain to a quadrilateral tube winding around the torus as illustrated in Fig. 1.14. Besides the obvious reduction in the computational costs due to the smaller grid sizes for the reduced simulation domain, the periodic boundary conditions allow for a spectral treatment of turbulence, further improving the efficiency.

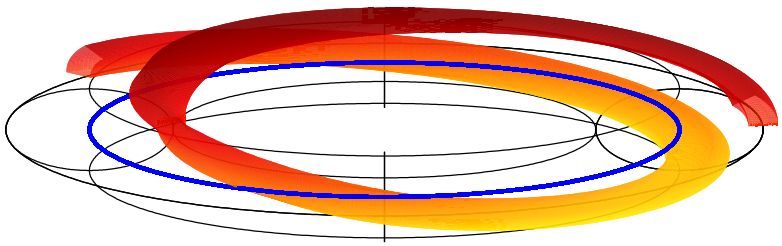

Figure 1.14. Schematic representation of the flux tube simulation domain for $q = 1.4$. The magnetic axis of the torus is shown in blue.

1.4.3. Adiabatic electron approximation

Due to their low mass the electrons move rapidly along the field lines with a much higher thermal velocity than the ions. For a deuterium plasma with similar electron and ion temperature this leads to a ratio of

$$\frac{v_{\mathrm{th},e}}{v_{\mathrm{th},i}} = \sqrt{\frac{m_i}{m_e}} \approx 60 \tag{1.84}$$

for the thermal velocities. On the time scale of ions the electrons react nearly instantly to restore quasi-neutrality, i.e. their density response is described solely by the electric field due to an ion density perturbation. The adiabatic electron response (see Sec. 1.3.1)

$$\frac{\tilde{n}_e}{n_{e0}} = \frac{e\tilde{\phi}}{T_e}, \tag{1.85}$$

where the tilde denotes a perturbed quantity, can be used to approximate the influence of the electrons in the Poisson equation analytically. Then, only the ions are treated as a kinetic species and the electron dynamics do not need to be simulated. Simulations with "adiabatic electrons" have significantly reduced requirements on computational resources, as the slower thermal ion velocity allows for a much larger time step.

The adiabatic electron approximation is suitable for many numerical experiments, where the dynamics are dominated by the ions, e.g. the heat transport due to ITG turbulence is mainly carried by the ions. In that case the electron dynamics provide a quantitative correction but do not impact the physical mechanisms or qualitative result. However, the kinetic treatment of electrons, often abbreviated by "kinetic electrons", is required for many plasma phenomena like the trapped electron mode instability [16], or the intrinsic current driven by turbulence (see Chapter 2).

1.5. The gyrokinetic code GKW

All turbulence simulations in this thesis are performed with the gyrokinetic code GKW (GyroKinetic Workshop). GKW is a Eulerian Vlaslov code designed for the study of turbulence and microinstabilities in a magnetically confined plasma. It solves the gyrokinetic equation on a fixed grid in the 5-dimensional phase space using a combination of finite difference and pseudo-spectral methods. This section details the aspects relevant to this work, namely the normalisation, the exact equations solved, and a brief discussion of the spectral representation and treatment of collisions. A complete description of the code is given in Ref. [65].

1.5.1. Normalisation

As is good practice in computer simulations all quantities in the code are normalised using a set of reference quantities: reference mass m_{ref}, density n_{ref}, temperature T_{ref}, thermal velocity v_{thref}, magnetic field B_{ref} evaluated on the magnetic axis and reference major radius R_{ref}. Naturally these are interrelated by

$$T_{\text{ref}} = \frac{1}{2} m_{\text{ref}} v_{\text{thref}}^2 \quad \text{and} \quad \rho_{\text{ref}} = \frac{m_{\text{ref}} v_{\text{thref}}}{e B_{\text{ref}}}, \tag{1.86}$$

with the reference Larmor radius ρ_{ref} which is used to define the smallness parameter, the normalised Larmor radius

$$\rho_* = \frac{\rho_{\text{ref}}}{R_{\text{ref}}}. \tag{1.87}$$

Using the reference values it is possible to relate the dimensionless quantities (subscript N) used in the code to the corresponding physical ones:

$$m = m_{\text{ref}} m_N, \quad n_0 = n_{\text{ref}} n_N, \quad v_{\text{th}} = v_{\text{thref}} v_{\text{th},N}. \tag{1.88}$$

Note that the normalised mass, density and thermal velocity are defined for each kinetic species. Similarly, the velocity space coordinates are normalised for each species

$$v_\parallel = v_{\text{th}} v_{\parallel N}, \quad \mu = \frac{m v_{\text{th}}}{B_{\text{ref}}} \mu_N \tag{1.89}$$

and accordingly the distribution functions

$$f = \rho_* \frac{n_0}{v_{\text{th}}^3} f_N, \quad F_M = \frac{n_0}{v_{\text{th}}^3} F_{M,N}. \tag{1.90}$$

The total particle distribution function $f_{\text{tot}} = f + F_M$ is split in the Maxwellian background F_M and the perturbed distribution function f. As all normalised quantities are supposed to be of order unity, factors of ρ_* are added for perturbed quantities.

All other quantities are normalised by using reference values only. The perturbed electrostatic potential ϕ is given by

$$\phi = \rho_* \frac{T_{\text{ref}}}{e} \phi_N \tag{1.91}$$

and the time t, angular rotation frequency Ω, major radius R, as well as the magnetic field B by

$$t = \frac{R_{\text{ref}}}{v_{\text{thref}}} t_N, \quad \Omega = \frac{v_{\text{thref}}}{R_{\text{ref}}} \Omega_N, \quad R = R_{\text{ref}} R_N, \quad B = B_{\text{ref}} B_N. \tag{1.92}$$

The radial coordinate ψ is normalised with R_{ref}, and for circular flux surfaces $\psi = r/R_{\text{ref}} = \epsilon$ is used, where r is the minor radius. The gradients are also normalised using the major radius

$$\nabla = \frac{1}{R_{\text{ref}}} \nabla_N. \tag{1.93}$$

The perpendicular variation of fluctuating quantities is on the scale of the Larmor radius and the wave vectors used in the case of a spectral representation are therefore normalised to ρ_{ref}:

$$k = \frac{1}{\rho_{\text{ref}}} k_N. \tag{1.94}$$

Finally, as customary in the literature, the dimensionless background temperature (density) gradient length scale R/L_T (R/L_n) is used

$$R/L_T = -\frac{R_{\text{ref}}}{T} \frac{\partial T}{\partial r} = -\frac{1}{T} \frac{\partial T}{\partial \psi}, \quad R/L_n = -\frac{R_{\text{ref}}}{n_0} \frac{\partial n_0}{\partial r} = -\frac{1}{n_0} \frac{\partial n_0}{\partial \psi}. \tag{1.95}$$

1.5.2. The gyrokinetic equation in GKW

The flux tube version of GKW solves the gyrokinetic equation for the gyroaveraged particle distribution function $f_{\text{tot}}(\mathbf{X}, v_\parallel, \mu)$ in a co-moving frame, using the gyrocentre position $\mathbf{X}$, the velocity parallel to the magnetic field $v_\parallel$ and the magnetic moment μ, which serves as the perpendicular velocity coordinate, to describe the 5-dimensional phase space. The collisionless equation takes the form [53, 66]:

$$\frac{\partial f_{\text{tot}}}{\partial t} + \frac{\mathrm{d}\mathbf{X}}{\mathrm{d}t} \cdot \nabla f_{\text{tot}} + \frac{\mathrm{d}v_\parallel}{\mathrm{d}t} \frac{\partial f_{\text{tot}}}{\partial v_\parallel} = 0. \tag{1.96}$$

Note that the magnetic moment is an adiabatic invariant in the gyrokinetic theory, i.e. $\mathrm{d}\mu/\mathrm{d}t = 0$. For kinetic electrons or multiple ion species the equation has to be solved for each kinetic species but this section uses a single kinetic species for clarity and omits the species subscript.

The code is designed to include a variety of physical mechanisms including centrifugal effects [66, 67] and electromagnetic field perturbations. However, these are neglected in the studies performed in this thesis and the terms are omitted in this section to avoid confusion. The time evolution of the gyrocentre position is given by

$$\frac{\mathrm{d}\mathbf{X}}{\mathrm{d}t} = v_\parallel \mathbf{b} + \mathbf{v}_E + \mathbf{v}_D, \tag{1.97}$$

where $\mathbf{b}$ is the unit vector in direction of the magnetic field. The velocity includes the motion

parallel to the field line, the E×B drift

$$\mathbf{v}_E = \frac{\mathbf{b} \times \nabla \langle \phi \rangle}{B} \tag{1.98}$$

and the drifts due to the inhomogeneous magnetic field and inertial terms (see Sec. 1.1.1)

$$\mathbf{v}_D = \left(m v_\parallel^2 + \mu B \right) \frac{\mathbf{b} \times \nabla B}{ZeB^2} + \frac{2 m v_\parallel}{ZeB} \mathbf{\Omega}_\perp, \tag{1.99}$$

where $\mathbf{\Omega}_\perp = \mathbf{\Omega} - (\mathbf{\Omega} \cdot \mathbf{b})\mathbf{b}$ is the part of the angular toroidal rotation vector perpendicular to the field. The first term represents the ∇B and the curvature drift in the low plasma β approximation and the last term is the Coriolis drift [6].

The parallel acceleration $\mathrm{d}v_\parallel / \mathrm{d}t$ can be derived using the conservation of energy

$$\frac{\mathrm{d}}{\mathrm{d}t} \left[\frac{1}{2} m v_\parallel^2 + \mu B + Ze \langle \phi \rangle \right] = 0 \tag{1.100}$$

$$m v_\parallel \frac{\mathrm{d}v_\parallel}{\mathrm{d}t} = -\frac{\mathrm{d}\mathbf{X}}{\mathrm{d}t} \cdot \left[\mu \nabla B + Ze \nabla \langle \phi \rangle \right]. \tag{1.101}$$

The distribution function is split into the perturbed part $f(\mathbf{X}, v_\parallel, \mu)$ and the Maxwellian background F_M, i.e. $f_{\text{tot}} = f + F_M$ and the δf approximation is employed. The equation for the time evolution of the perturbed distribution is given by [66]

$$\frac{\partial f}{\partial t} + \left(v_\parallel \mathbf{b} + \mathbf{v}_E + \mathbf{v}_D \right) \cdot \nabla f - \frac{\mu}{m} \mathbf{b} \cdot \nabla B \frac{\partial f}{\partial v_\parallel} = S, \tag{1.102}$$

where the source term S is determined by the background distribution and only terms up to the first order in ρ_* are considered. The Maxwellian is given by

$$F_M = \frac{n_0}{\pi^{3/2} v_{\text{th}}^3} \exp \left[- \frac{(v_\parallel - (RB_t/B)\omega_\varphi)^2 + 2\mu B/m}{v_{\text{th}}^2} \right], \tag{1.103}$$

where n_0 and v_{th} are the density and thermal velocity of the species. They are evaluated at the considered flux surface and are constant with a constant gradient across the radial domain of the flux tube. The mean parallel velocity $u_\parallel = (RB_t/B)\omega_\varphi(r)$ with the toroidal component of the magnetic field B_t and the angular rotation ω_φ is zero at the flux surface considered, as the equations are formulated in a co-moving frame which rotates as a rigid body with constant angular frequency $\mathbf{\Omega}$. However, plasma rotation can have a radial gradient and $\nabla \omega_\varphi$ will enter the equations, because a differential rotation of the frame is impractical as it entails a time dependent metric.

Inserting the Maxwellian in the gyrokinetic equation yields the source term

$$S = -(\mathbf{v}_E + \mathbf{v}_D) \cdot \left[\frac{\nabla n_0}{n_0} + \left(\frac{v_\parallel^2}{v_{\text{th}}^2} + \frac{\mu B}{T} - \frac{3}{2} \right) \frac{\nabla T}{T} + \frac{m v_\parallel}{T} \frac{R B_T}{B} \nabla \omega_\varphi \right] F_M \\ - \frac{Ze}{T} (v_\parallel \mathbf{b} + \mathbf{v}_D) \cdot \nabla \langle \phi \rangle F_M. \tag{1.104}$$

Note that S also contains the time evolution of the background without turbulence, which is a ρ_* correction to the Maxwellian and is given by the term $\mathbf{v}_D \cdot \nabla F_M$, i.e. the part proportional to $\mathbf{v}_D$ of the first term on the right. All other terms which are also of the order ρ_* are connected to the perturbed potential, which is determined by f. If one were to use a time-dependent background distribution function, the $\mathbf{v}_D \cdot \nabla F_M$ term would allow to describe the neoclassical transport in the gyrokinetic equation. The coupling of turbulence can be of interest for example for current generation or intrinsic rotation (see Chapters 2 and 3) but the numerical requirements for turbulence and neoclassics do not match up well, in particular, the high resolution required for an accurate calculation of the neoclassical background would lead to very expensive nonlinear turbulence simulations. Therefore, other methods, like the coupling of the code with a dedicated neoclassical equilibrium solver, to account for the neoclassical background are preferable. In standard gyrokinetic simulations the Maxwellian is assumed constant and the correction $\rho_* F_M$ is neglected. Note that when considering only the turbulent perturbation this is consistent with the ordering used in Eq. 1.102, as the correction to the perturbed distribution $f \sim \rho_*(F_M + \rho_* F_M)$ would be of second order in ρ_*.

To close the set of equations, the gyrokinetic Poisson equation needs to be adjoined to calculate the perturbed potential ϕ. GKW uses a spectral representation of the linearized gyrokinetic Poisson equation, which considers the polarisation density only for the Maxwellian background. In normalised units the equation is given for a single Fourier mode $\hat{\phi}$ by

$$\sum_s Z_s n_{0,s} \left[B \iint \mathrm{d}v_\parallel \mathrm{d}(2\pi\mu)\ J_0(k_\perp \rho_s) \hat{f}_s + \frac{Z_s}{T_{N,s}} \left(\Gamma(b_s) - 1 \right) \hat{\phi} \right] = 0, \tag{1.105}$$

where the Bessel function $J_0(k_\perp \rho_s)$ is used for the gyroaverage and the modified Bessel function $\Gamma(b_s)$ to express the polarisation density for the Maxwellian background. The species dependent parameter b_s is given by

$$b_s = \frac{1}{2} m_{N,s} T_{N,s} \frac{\rho_{\text{ref}} k_\perp}{Z_s B^2}. \tag{1.106}$$

The sum is performed over every kinetic species s. In the adiabatic electron limit the simplified equation

$$\sum_{\text{ions}} \left[B \iint \mathrm{d}v_\parallel \mathrm{d}(2\pi\mu)\ J_0(k_\perp \rho_s) \hat{f}_s + \frac{Z_s}{T_{N,s}} \left(\Gamma(b_s) - 1 \right) \hat{\phi} \right] = \frac{n_{0,e}}{T_{N,e}} (\hat{\phi} - \{\hat{\phi}\}) \tag{1.107}$$

sums only over the ions and uses the adiabatic electron response on the right hand side to

account for the electrons.

In GKW the terms of the time evolution are sorted by their physical meaning and it is possible to switch of or modify distinct physical effects for numerical experiments. Most notably, the non-linear term can be suppressed to perform a linear stability analysis, where the toroidal modes do not interact with each other, referred to as "linear simulations". The full set of equations including their implementation with geometric tensors can be found in [65].

1.5.3. Spectral representation

The local flux tube limit allows for periodic boundary conditions in the radial (ψ) and the binormal (ζ) direction as the assumption of a homogeneous background leads to homogeneous turbulence. Therefore, the turbulence in the plane perpendicular to the magnetic field line can be described by a computationally efficient Fourier approach. Therefore, GKW uses a semi-spectral space representation, i.e. the direction parallel to the field (s) and the velocity phase space is treated with a finite difference grid approach, while the ζ, ψ dependency is given by Fourier modes k_ψ, k_ζ. It is possible to also treat the radial direction with a finite difference scheme, which is used for so called flux-driven simulations and global simulations, where profile effects are kept. Flux-driven simulations use the local limit approximation with the turbulence driven by source and sink functions at the edges of the radial domain rather than by background gradients. They are used in Chapter 5 while all other chapters use gradient-driven simulations and the semi-spectral representation.

$$f(\psi, \zeta, s) = \sum_{k_\psi, k_\zeta} \left[\hat{f}(k_\psi, k_\zeta, s) \exp[\mathrm{i} k_\psi \psi/\rho_* + \mathrm{i} k_\zeta \zeta/\rho_*] \right] \tag{1.108}$$

Thus, the derivative in $\beta = \psi, \zeta$ direction is treated analytically $\rho_* \partial/\partial x_\beta = i k_\beta$. Note that f is a real quantity and thus $\hat{f}(k_\psi, k_\zeta, s) = \hat{f}^\dagger(-k_\psi, -k_\zeta, s)$. This is used in the code to calculate only the evolution of modes with $k_\zeta \geq 0$. The distribution function is given by

$$\begin{aligned} f(\psi, \zeta, s) = \sum_{k_\zeta > 0, k_\psi} \Big[& \hat{f}(k_\psi, k_\zeta, s) \exp[\mathrm{i} k_\zeta \zeta/\rho_* + \mathrm{i} k_\psi \psi/\rho_*] + \\ & \hat{f}^\dagger(k_\psi, k_\zeta, s) \exp[-\mathrm{i} k_\zeta \zeta/\rho_* - \mathrm{i} k_\psi \psi/\rho_*] \Big] + \sum_{k_\psi} \hat{f}(k_\psi, k_\zeta = 0, s) \exp[\mathrm{i} k_\psi \psi/\rho_*] \end{aligned} \tag{1.109}$$

with an equivalent expression for ϕ.

1.5.4. Collisions

Coulomb collisions between particles can be included in GKW. They are modelled with a linearized Fokker-Planck collision operator $\mathcal{C}$, which is added to the right hand side of the gyrokinetic equation (1.102). Assuming a Maxwellian background the linearized collision operator

can be derived from the Landau collision integral [68]

$$\mathcal{C}(f_a) = \sum_b \frac{1}{v^2}\frac{\partial}{\partial v}\left[v^2\left(D_{vv}^{a/b}\frac{\partial f_a}{\partial v} - F_v^{a/b} f_a\right)\right] + \frac{1}{v\sin\vartheta}\frac{\partial}{\partial \vartheta}\left[\sin\vartheta D_{\vartheta\vartheta}^{a/b}\frac{1}{v}\frac{\partial f_a}{\partial \vartheta}\right]. \quad (1.110)$$

The operator acts on the distribution of species a and sums over all species b (including self interaction). It is given in the (v, ϑ) coordinate system, where v is the velocity and ϑ the pitch angle, the angle between the velocity vector and the magnetic field. The model includes pitch angle scattering, energy scattering and momentum scattering with their respective coefficients $D_{\vartheta\vartheta}^{a/b}$, $D_{vv}^{a/b}$ and $F_v^{a/b}$.

The coefficients are proportional to the collision frequency

$$\Gamma^{a,b} = \frac{R_{\text{ref}} n_b Z_a^2 Z_b^2 e^4 \ln\Lambda^{a,b}}{4\pi\epsilon_0^2 m_a^2 m_b^2 v_{\text{th},a}} \quad (1.111)$$

for collision of species a with species b. The expressions for the Coulomb logarithm $\Lambda^{a,b}$, the coefficients and the implementation in the code is given in Ref. [65]. While the linearized Fokker-Planck preserves the particle number, there is no exact conservation of energy or momentum. Therefore, there are ad hoc corrections terms that an be used to artificially restore conservation.

2. Turbulence driven stationary electric currents in a tokamak

It is conventionally assumed, that the neoclassical and turbulent description of a plasma can be treated separately. This is, in many cases, a reasonable approximation because of the strong separation in length and time scales, with the neoclassical solution having length scales of the order of the plasma size and a timescale equal to the confinement time, while the turbulent dynamics have length scales of the order of the gyro-radius and evolve on the ion transit time scale. Furthermore, different aspects of plasma behaviour are well described by employing just one regime. Turbulent transport is the dominant loss channel for thermal energy in tokamak plasmas, while several other aspects, like current and resistivity are governed by neoclassical effects. A popular example is the intrinsic current called bootstrap current which is driven by pressure gradients [11–13].

Recently the impact of the neoclassical modifications to the background distribution function, used in turbulent transport calculations, has been the object of a number of studies, showing its relevance for the generation of intrinsic rotation [69–75]. Chapter 3 of this thesis is also dedicated to this effect. Another example for the interplay of turbulence and neoclassics is the synergy of the respective impurity transport channels [76]. The influence of the turbulent dynamics on the neoclassical transport has received less interest, but it has been shown to modify the momentum flux in neoclassics, which can also drive intrinsic rotation [77]. Furthermore, several mechanisms for turbulent current drive are known. These include modifications to Ohm's law like hyper-resistivity, anomalous resistivity, as well as turbulent sources, e.g. electromotive forces due to the interplay of density and potential perturbations and electromagnetic flutter. Also modifications to the electron momentum flux and a "turbulent bootstrap current" proportional to the current gradient have been investigated [78–83]. The magnitude of the turbulence driven current is expected to be up to 10% [81] or even 25% [83] of the neoclassical bootstrap current. In present experiments large parts of the current density are driven by an external transformer, limiting the operational time, and thus making additional current sources interesting for economically viable reactors.

The work presented in this chapter introduces turbulent source terms, which are connected to the parallel velocity nonlinearity in the gyrokinetic equation. These source terms have a non-zero time average and exert a force on the neoclassical background. The method of using a gyrokinetic and a neoclassical code separately and considering the full parallel balance equations, captures the impact of homogeneous turbulence consistently from a nonlinear description. Especially the force due to the heat flux balance can be expected to play an important role in ITG turbulence, and is not considered in the global simulations in Ref.[79] or in the quasi-linear theory used in the analytic description of fluxes in Ref. [81]. Thus, the study extends

previous work but, in the process, neglects effects generated by inhomogeneous turbulence.

The remainder of this chapter is structured as follows. In Section 2.1 the coupling of neoclassics and turbulence is discussed in detail and the turbulent terms associated with the velocity nonlinearity, affecting the neoclassical solution are derived. Section 2.2 gives a rough estimate of the relevance of the effect. Section 2.3 presents the results of simulations to assess the current generated by turbulence. Finally, conclusions are formulated in Section 2.4.

2.1. Coupling of turbulence and neoclassics

Consider the gyrokinetic equation for the distribution function f, written in conservative form

$$\frac{\partial f}{\partial t} + \nabla \cdot \left[\frac{\mathrm{d}\mathbf{X}}{\mathrm{d}t} f\right] + \frac{\partial}{\partial v_\parallel}\left[\frac{\mathrm{d}v_\parallel}{\mathrm{d}t} f\right] = C(f). \tag{2.1}$$

Here, $\mathrm{d}\mathbf{X}/\mathrm{d}t$ is the gyrocentre velocity

$$\frac{\mathrm{d}\mathbf{X}}{\mathrm{d}t} = v_\parallel \mathbf{b} + \mathbf{v}_D + \mathbf{v}_E, \tag{2.2}$$

where $v_\parallel \mathbf{b}$ is the velocity parallel to the magnetic field, $\mathbf{v}_D$ is the drift velocity connected with the magnetic field inhomogeneity as well as the plasma rotation, and $\mathbf{v}_E$ is the E×B velocity. The plasma is assumed to be electrostatic and $\mathrm{d}v_\parallel/\mathrm{d}t$ is the acceleration

$$m v_\parallel \frac{\mathrm{d}v_\parallel}{\mathrm{d}t} = -\frac{\mathrm{d}\mathbf{X}}{\mathrm{d}t} \cdot [Ze\nabla\langle\phi\rangle + \mu\nabla B] \tag{2.3}$$

where $\langle\phi\rangle$ is the gyroaveraged potential and B the magnetic induction. Finally, $C(f)$ is the collision operator which will be assumed to be accurately described by its linearized form.

The equation for the distribution function describes both the turbulent as well as the neoclassical transport. Below the evolution equation (2.1) is split to describe as far as possible each of these effects separately. This allows for the determination of the coupling between turbulence and neoclassics and clarifies how the turbulent transport can influence the neoclassical solution. To split the equation it is assumed that the turbulence can be described within the local flux tube limit. Thus, the turbulence is described as homogeneous in the plane perpendicular to the magnetic field. It is stressed that this approximation eliminates a channel through which the turbulence can have an impact on the neoclassical solution. Therefore the coupling between neoclassics and turbulence derived below does not contain all possible effects. The reader is referred to Ref. [77] for further details.

To proceed the distribution function f, the gyro-centre velocity $\mathrm{d}\mathbf{X}/\mathrm{d}t$ and the parallel acceleration $\mathrm{d}v_\parallel/\mathrm{d}t$ are split into a time independent (bar) and a fluctuating part (tilde)

$$f = \widetilde{f} + \overline{f} \qquad \frac{\mathrm{d}\mathbf{X}}{\mathrm{d}t} = \frac{\mathrm{d}\widetilde{\mathbf{X}}}{\mathrm{d}t} + \frac{\mathrm{d}\overline{\mathbf{X}}}{\mathrm{d}t} \qquad \frac{\mathrm{d}v_\parallel}{\mathrm{d}t} = \frac{\mathrm{d}\widetilde{v}_\parallel}{\mathrm{d}t} + \frac{\mathrm{d}\overline{v}_\parallel}{\mathrm{d}t}, \tag{2.4}$$

where, by definition, the time average of the fluctuating quantities disappears

$$\left\langle \widetilde{f} \right\rangle_t = 0 \qquad \left\langle \frac{\mathrm{d}\widetilde{\mathbf{X}}}{\mathrm{d}t} \right\rangle_t = 0 \qquad \left\langle \frac{\mathrm{d}\widetilde{v}_\parallel}{\mathrm{d}t} \right\rangle_t = 0. \tag{2.5}$$

The fluctuating part describes the turbulent dynamics, while the neoclassical solution as well as the background are contained in the time independent part. Substituting the expressions above in the evolution equation (2.1) and taking the time average yields

$$\frac{\partial \overline{f}}{\partial t} + \nabla \cdot \left[\left\langle \frac{\mathrm{d}\widetilde{\mathbf{X}}}{\mathrm{d}t} \widetilde{f} \right\rangle_t + \frac{\mathrm{d}\overline{\mathbf{X}}}{\mathrm{d}t} \overline{f} \right] + \frac{\partial}{\partial v_\parallel} \left[\left\langle \frac{\mathrm{d}\widetilde{v}_\parallel}{\mathrm{d}t} \widetilde{f} \right\rangle_t + \frac{\mathrm{d}\overline{v}_\parallel}{\mathrm{d}t} \overline{f} \right] = C(\overline{f}). \tag{2.6}$$

The equation above uses $\langle C(\widetilde{f}+\overline{f})\rangle_t = C(\overline{f})$ which is true for the linearized collision operator. Two terms appear in this equation that are connected with the turbulence. Using

$$\frac{\mathrm{d}\widetilde{\mathbf{X}}}{\mathrm{d}t} = \widetilde{\mathbf{v}}_E = \frac{\mathbf{b} \times \nabla \langle \widetilde{\phi} \rangle}{B}, \tag{2.7}$$

the first term can be written in the form

$$\left\langle \frac{\mathrm{d}\widetilde{\mathbf{X}}}{\mathrm{d}t} \widetilde{f} \right\rangle_t = \left\langle \widetilde{\mathbf{v}}_E \widetilde{f} \right\rangle_t. \tag{2.8}$$

In the case of homogeneous turbulence the time averaged fluxes are independent of the radial coordinate and the fluxes vanish under the divergence operator. Then, using

$$m v_\parallel \frac{\mathrm{d}\widetilde{v}_\parallel}{\mathrm{d}t} = -Ze \left(v_\parallel \mathbf{b} + \mathbf{v}_D \right) \cdot \nabla \langle \widetilde{\phi} \rangle - \mu \widetilde{\mathbf{v}}_E \cdot \nabla B, \tag{2.9}$$

the only term in the equation (2.6) for $\overline{f}$ related to the turbulence is:

$$\left\langle \frac{\mathrm{d}\widetilde{v}_\parallel}{\mathrm{d}t} \widetilde{f} \right\rangle_t = -\left\langle \frac{1}{m v_\parallel} \left[Ze \left(v_\parallel \mathbf{b} + \mathbf{v}_D \right) \cdot \nabla \langle \widetilde{\phi} \rangle + \mu \widetilde{\mathbf{v}}_E \cdot \nabla B \right] \widetilde{f} \right\rangle_t. \tag{2.10}$$

The various velocity moments of this term represent the particle, momentum and energy fluxes. The terms in the equation above can be transformed using the relation

$$\mu \widetilde{\mathbf{v}}_E \cdot \nabla B = \mu \frac{\mathbf{b} \times \nabla \langle \widetilde{\phi} \rangle}{B} \cdot \nabla B = -\mu \frac{\mathbf{b} \times \nabla B}{B} \cdot \nabla \langle \widetilde{\phi} \rangle, \tag{2.11}$$

and the equation for the drift in the low beta approximation

$$\mathbf{v}_D = \left[\frac{m v_\parallel^2}{B} + \mu \right] \frac{\mathbf{b} \times \nabla B}{ZeB} + \frac{2 m v_\parallel}{ZeB} \boldsymbol{\Omega}_\perp, \tag{2.12}$$

where $\boldsymbol{\Omega}_\perp = \boldsymbol{\Omega} - (\boldsymbol{\Omega} \cdot \mathbf{b})\mathbf{b}$ is the part of the angular rotation perpendicular to the field line. The

∇B-drift in the gyrocentre motion is then cancelled by the inner product of the fluctuating E×B velocity and the gradient of the magnetic field which yields

$$\left\langle \frac{\mathrm{d}\widetilde{v}_\parallel}{\mathrm{d}t}\widetilde{f} \right\rangle_t = -\left\langle \left[\frac{Ze}{m}\mathbf{b} + \frac{v_\parallel \mathbf{b}\times\nabla B}{B^2} + \frac{2}{B}\mathbf{\Omega}_\perp \right] \cdot \nabla\langle\widetilde{\phi}\rangle \widetilde{f} \right\rangle_t . \tag{2.13}$$

With the expression above the equation for the steady state distribution can be written in the form

$$\begin{aligned} \frac{\partial \overline{f}}{\partial t} + \nabla\cdot\left[\frac{\mathrm{d}\overline{\mathbf{X}}}{\mathrm{d}t}\overline{f}\right] + \frac{\partial}{\partial v_\parallel}\left[\frac{\mathrm{d}\overline{v}_\parallel}{\mathrm{d}t}\overline{f}\right] - C(\overline{f}) = \\ \frac{\partial}{\partial v_\parallel}\left[\left\langle \left(\frac{Ze}{m}\mathbf{b} + \frac{v_\parallel \mathbf{b}\times\nabla B}{B^2} + \frac{2}{B}\mathbf{\Omega}_\perp \right) \cdot \nabla\langle\widetilde{\phi}\rangle \widetilde{f} \right\rangle_t \right]. \end{aligned} \tag{2.14}$$

The left hand side is the equation that is usually solved in neoclassical theory, while the right hand side presents an additional source due to the turbulence. The source term does not depend explicitly on the steady state distribution $\overline{f}$, and if the turbulent solution is known, can thus be evaluated separately taking only the turbulent solution.

Subtracting the equation for $\overline{f}$ from the original equation (2.1), one obtains the equation for the turbulence

$$\begin{aligned} \frac{\partial \widetilde{f}}{\partial t} + \nabla\cdot\left[\left(\frac{\mathrm{d}\overline{\mathbf{X}}}{\mathrm{d}t} + \frac{\mathrm{d}\widetilde{\mathbf{X}}}{\mathrm{d}t}\right)\widetilde{f}\right] + \frac{\partial}{\partial v_\parallel}\left[\left(\frac{\mathrm{d}\overline{v}_\parallel}{\mathrm{d}t} + \frac{\mathrm{d}\widetilde{v}_\parallel}{\mathrm{d}t}\right)\widetilde{f}\right] = \\ C(\widetilde{f}) - \nabla\cdot\left[\frac{\mathrm{d}\widetilde{\mathbf{X}}}{\mathrm{d}t}\overline{f}\right] - \frac{\partial}{\partial v_\parallel}\left[\frac{\mathrm{d}\widetilde{v}_\parallel}{\mathrm{d}t}\overline{f} + \left\langle \frac{\mathrm{d}\widetilde{v}_\parallel}{\mathrm{d}t}\widetilde{f}\right\rangle_t\right]. \end{aligned} \tag{2.15}$$

The equation for the turbulence is usually formulated without the last term in the square brackets, i.e. the time averaged velocity nonlinearity. The velocity nonlinearity is one order higher in the normalised Larmor radius and will be neglected in the evaluation of $\widetilde{f}$. Note, however, that it is the velocity nonlinearity that generates the cross-coupling between the turbulence and the neoclassical solution. It should be also noted, that the neoclassical transport can influence the turbulence as well [71, 73]. The time averaged distribution $\overline{f}$ must be seen as a solution of Eq. (2.14), which can be assumed constant on the time scale of the turbulence, and will affect the turbulence through the terms on the right hand side. Here, this cross-coupling will not be examined, and the background will be assumed to be a Maxwellian $\overline{f} = F_M$.

The neoclassical equation (2.14) can be solved with a set of flux surface averaged parallel balance equations [14]. The left hand side of Eq. (2.14) is equivalent to the kinetic equation used in Ref. [14] (see Appendix A for the derivation of the parallel force balance starting from Eq. (2.14)). Following the notation of Ref. [15] (only for single charge states) the equations are given by

$$\{\mathbf{B}\cdot\nabla\cdot\mathbf{P}^a_\alpha\} = \{\mathbf{F}^a_\alpha\cdot\mathbf{B}\} + S^a_{\parallel,\alpha}, \tag{2.16}$$

for each species a with $\alpha = 1, 2, 3$ and follow from the kinetic equation by taking the odd

velocity moments $\{\int \mathrm{d}^3v\ m_a\mathbf{B}\cdot\mathbf{v}L_{\alpha-1}^{3/2}(x_a^2)\cdots\}$. Here $\mathbf{P}_\alpha^a$ is the viscosity tensor and $\mathbf{F}_\alpha^a$ the friction force. The curly brackets $\{\cdots\}$ denote the flux surface average and the Laguerre polynomials $L_{\alpha-1}^{3/2}(x_a^2)$ are,

$$L_0^{3/2}(x_a^2) = 1, \tag{2.17}$$

$$L_1^{3/2}(x_a^2) = \frac{5}{2} - x_a^2, \tag{2.18}$$

$$L_2^{3/2}(x_a^2) = \frac{35}{8} - \frac{7}{2}x_a^2 + \frac{1}{4}x_a^4, \tag{2.19}$$

with $x_a = v/v_{\mathrm{th},a}$ and $v_{\mathrm{th},a}$ being the thermal velocity of species a. The three moments correspond to the force balance, the heat flux balance and a higher order term, which has no direct physical interpretation but can strongly influence the lower order quantities. The source terms $S_{\parallel,\alpha}^a = S_{E\parallel,\alpha}^a + S_{\mathrm{VNL}\parallel,\alpha}^a$ include an external electric field E and the turbulent terms given by the right hand side of Eq. (2.14). The turbulent source terms are

$$\begin{aligned} S_{\mathrm{VNL}\parallel,\alpha}^a &= \left\{ \int \mathrm{d}^3v\ m_a\mathbf{B}\cdot\mathbf{v}L_{\alpha-1}^{3/2}(x_a^2)\frac{\partial}{\partial v_\parallel}\left\langle \frac{\mathrm{d}\widetilde{v}_\parallel}{\mathrm{d}t}\widetilde{f}\right\rangle_t \right\} \\ &= -\left\langle \left\{ \int \mathrm{d}^3v\ m_aB\frac{\partial}{\partial v_\parallel}\left(v_\parallel L_{\alpha-1}^{3/2}(x_a^2)\right)\frac{\mathrm{d}\widetilde{v}_\parallel}{\mathrm{d}t}\widetilde{f}\right\}\right\rangle_t, \end{aligned} \tag{2.20}$$

where partial integration in the parallel velocity is used for the last step and $\mathrm{d}\widetilde{v}_\parallel/\mathrm{d}t$ is given by Eq. (2.13). The terms, having different underlying physical mechanisms, are split in three parts $S_{\mathcal{T},\alpha}^a$, with $\mathcal{T} = \mathcal{A},\mathcal{B},\mathcal{C}$. They are connected to the parallel electrostatic field perturbations ($\mathcal{A}$), the curvature ($\mathcal{B}$) and the Coriolis force ($\mathcal{C}$) and are given by

$$S_{\mathcal{T},\alpha}^a = -\left\langle \left\{ \int \mathrm{d}^3v\ \frac{\partial}{\partial v_\parallel}\left(v_\parallel L_{\alpha-1}^{3/2}(x_a^2)\right)\mathcal{T}\widetilde{f}_a\right\}\right\rangle_t \tag{2.21}$$

with

$$\mathcal{A} = ZeB\mathbf{b}\cdot\nabla\langle\widetilde{\phi}\rangle, \tag{2.22}$$

$$\mathcal{B} = \frac{m_av_\parallel}{B}\mathbf{b}\times\nabla B\cdot\nabla\langle\widetilde{\phi}\rangle, \tag{2.23}$$

$$\mathcal{C} = 2m_a\mathbf{\Omega}_\perp\cdot\nabla\langle\widetilde{\phi}\rangle. \tag{2.24}$$

For the normalisation and implementation in GKW see Appendix B.

There is a crucial symmetry argument to be made here, closely following the discussion of momentum transport in Refs. [84–86]. In the model employed here and without background rotation or rotation gradient, the nonlinear gyrokinetic equation is invariant under the set of transformations

$$v_\parallel \to -v_\parallel,\ s\to -s,\ \psi\to-\psi,\ f\to -f,\ \phi\to-\phi, \tag{2.25}$$

where s is the field-aligned coordinate and ψ the radial coordinate. Furthermore, it can be shown that the source terms $S_{\mathcal{A}}$ and $S_{\mathcal{B}}$ change sign under the transformation while $S_{\mathcal{C}}$, which is zero without plasma rotation, is invariant. This allows for equivalent solutions of the gyrokinetic equation, which appear with equal probability but have the opposite sign in $S_{\mathcal{A}}$ and $S_{\mathcal{B}}$. Consequently, the time average of the turbulent state will yield a zero net contribution. However, this argument is no longer valid if the symmetry is broken by a non-zero background rotation or rotation gradient. If the symmetry breaking is small the effect will be linear in the responsible quantity. Note that $S_{\mathcal{C}}$ is also linear in the background rotation. The linear dependence on the background rotation can be verified in Fig. 2.1. Similarly, a small gradient in the rotation profile provides a linear scaling for $\mathcal{A}$ and $\mathcal{B}$. It is important to note, that the neoclassical description used here does not include rotational effects, whilst the turbulence simulations have a rotating background. This approximation, however, only leads to a small error in the limit of slow rotation, as the corrections to particle and heat fluxes are of the order

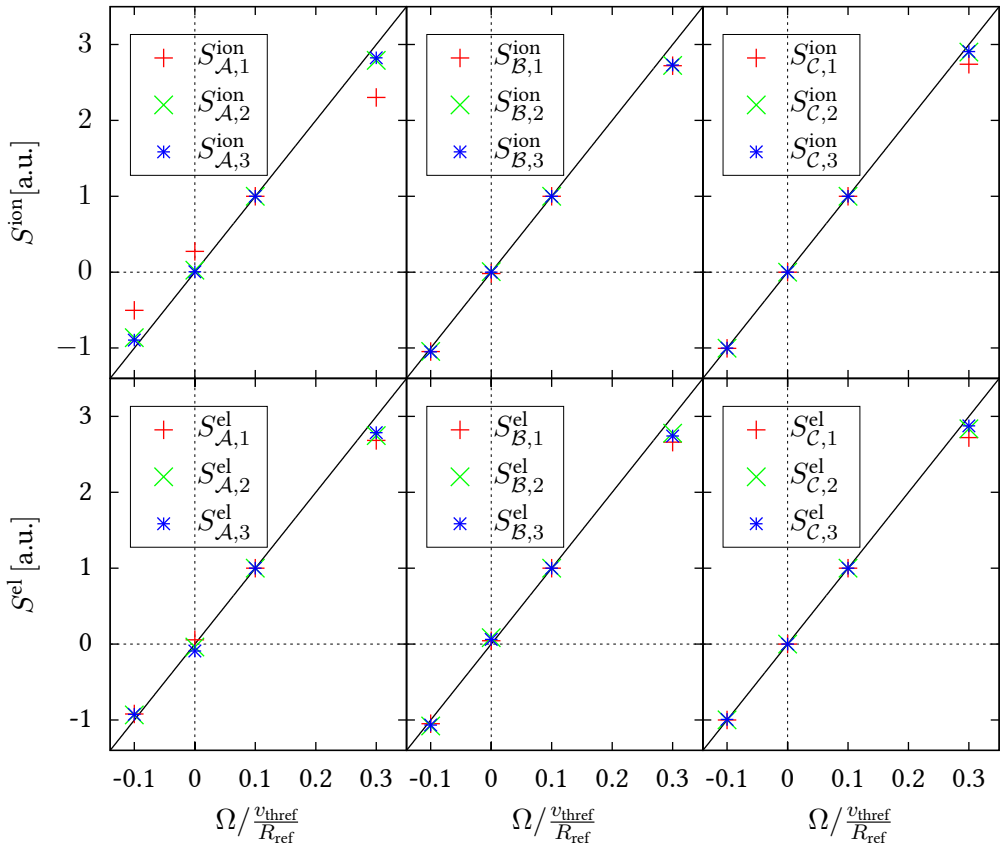

Figure 2.1. The time averaged source terms $S_{\mathcal{A},\mathcal{B},\mathcal{C}}$ for ions and electrons as a function of the angular frequency for a kinetic Cyclone Base Case simulation. Each order α is normalised to its respective value at $\Omega = 0.1$.

$(R\Omega/v_{\mathrm{th}})^2$ [15, 87]. Another important observation is that the direction of the force depends on the direction of the toroidal rotation. The current driven by $S_{\mathcal{A}}$ and $S_{\mathcal{B}}$ is always opposite to the rotation. The situation is more complicated for $S_{\mathcal{C}}$, which also depends on the orientation of $\mathbf{B}$. However, the current driven by $S^{\mathrm{el}}_{\mathcal{A}}$ is the most important contribution making the effect relevant for both directions of the magnetic field. Furthermore the orientation of the background current appears to have no significant effect on all terms considered.

2.2. Estimate of the effect of turbulence on the neoclassical solution

Before working out the effects of the turbulence forces on the neoclassical solution, the physical interpretation of the forcing terms is discussed.

The contribution from $\mathcal{A}$ can be interpreted as the interplay of density (or temperature) and potential perturbations and has already been studied for a global electromagnetic case in Ref. [79]. Density and potential are largely linked by the quasi-neutrality condition and the term can naturally be assumed small. It was found to be negligible with a current increase of about one percent. However there are two major differences to the approach taken here. Firstly, no plasma rotation was considered in Ref. [79]. Then the symmetry of Eq. (2.21) is not broken and in the formalism outlined above one would obtain a zero current contribution. Consequently, the current described in this chapter is caused by a different mechanism compared with Ref. [79], with the latter being related to the electromagnetic response or profile effects rather than the symmetry breaking. Secondly, higher order terms, especially the heat flux balance, which also exerts a force, were not considered. The dominant drive of the ITG is the temperature gradient. One may expect that the contribution of the heat flux forces is larger than that of the term studied by Ref. [79].

To better identify the physical origin of the source terms, the first velocity moment, which is the force the turbulence transfers to the background, is investigated in the fluid picture. In the following a tilde denotes a perturbed quantity, which is, compared to the background, one order smaller in $\rho_* = \rho_i/R$, i.e. the ion Larmor radius over the major radius. Ignoring the dependence of the quantities on the position inside the flux surface and neglecting the μ dependence of the gyroaverage, it is possible to express the terms with fluid quantities:

$$S^a_{\mathcal{A},1} \sim -ZeB\mathbf{b}\cdot\nabla\langle\widetilde{\phi}\rangle \int \mathrm{d}^3v\ \widetilde{f}_a = -ZeB\widetilde{n}_a\mathbf{b}\cdot\nabla\langle\widetilde{\phi}\rangle, \tag{2.26}$$

$$S^a_{\mathcal{B},1} \sim -\frac{m_a}{B}\mathbf{b}\times\nabla B\cdot\nabla\langle\widetilde{\phi}\rangle \int \mathrm{d}^3v\ v_\parallel\widetilde{f}_a \approx -\frac{m_a}{B}n_0\widetilde{u}_{\parallel a}\mathbf{b}\times\nabla B\cdot\nabla\langle\widetilde{\phi}\rangle, \tag{2.27}$$

$$S^a_{\mathcal{C},1} \sim -2m_a\mathbf{\Omega}_\perp\cdot\nabla\langle\widetilde{\phi}\rangle \int \mathrm{d}^3v\ \widetilde{f}_a = -2m\widetilde{n}_a\mathbf{\Omega}_\perp\cdot\nabla\langle\widetilde{\phi}\rangle, \tag{2.28}$$

where $\int \mathrm{d}^3v\ v_\parallel\widetilde{f} = \widetilde{nu_\parallel} \sim (n_0+\widetilde{n})(u_{\parallel 0}+\widetilde{u}_\parallel) - n_0u_{\parallel 0} \approx n_0\widetilde{u}_\parallel$ is interpreted as a first order perturbation of background density and perturbed fluid velocity $\widetilde{u}$. It is possible to identify the terms above with their counterparts in the fluid equation. For this purpose the first order

perturbed fluid velocity $\widetilde{\mathbf{u}}$ can be expressed as,

$$n_0\widetilde{\mathbf{u}} = \int \mathrm{d}^3v \ \left(v_\parallel \mathbf{b} + \mathbf{v}_D + \mathbf{v}_E\right)\left(F_M + \widetilde{f}\right) = n_0\widetilde{u}_\parallel \mathbf{b} + \frac{2n_0T_0}{ZeB}\frac{\mathbf{b}\times\nabla B}{B} + n_0\frac{\mathbf{b}\times\nabla\widetilde{\phi}}{B}, \quad (2.29)$$

assuming that the background is a Maxwellian F_M and $f = F_M + \widetilde{f}$. Note that

$$\int \mathrm{d}^3v \ \frac{mv_\parallel^2}{2}F_M = \frac{1}{2}n_0T_0 \quad \text{and} \quad \int \mathrm{d}^3v \ \frac{mv_\perp^2}{2}F_M = n_0T_0. \quad (2.30)$$

The fluid equation in the co-moving frame neglecting centrifugal forces, which is consistent with the treatment of the drifts in Eq. (2.12), is

$$mn\left[\frac{\partial u}{\partial t} + (\mathbf{u}\cdot\nabla)\mathbf{u}\right] = -2mn\boldsymbol{\Omega}\times\mathbf{u} + Zen\left[\mathbf{E} + \mathbf{u}\times\mathbf{B}\right] - \nabla p - \nabla\cdot\boldsymbol{\Pi}. \quad (2.31)$$

The first term on the right hand side is the Coriolis force. The force due to the turbulent fluctuations is

$$\mathbf{F}_C = -\langle 2m\widetilde{n}\boldsymbol{\Omega}\times\widetilde{\mathbf{u}}\rangle_t. \quad (2.32)$$

Using Eq. 2.29 and taking the inner product with $\mathbf{B}$ and averaging over the flux surface yields

$$\begin{aligned}\langle\{\mathbf{B}\cdot\mathbf{F}_C\}\rangle_t &= -\left\langle\left\{2m\widetilde{n}\left(\boldsymbol{\Omega}_\perp\cdot\nabla\widetilde{\phi} + \frac{2T_0}{ZeB}\boldsymbol{\Omega}_\perp\cdot\nabla B\right)\right\}\right\rangle_t \\ &= -\left\langle\left\{\int \mathrm{d}^3v\ 2m\boldsymbol{\Omega}_\perp\cdot\nabla\widetilde{\phi}f\right\}\right\rangle_t + \left\langle\left\{2m\widetilde{n}\frac{2T_0}{ZeB}\left(\frac{\epsilon}{q}\Omega\cos\theta\right)\left(\frac{\epsilon}{q}\sin\theta|\nabla B|\right)\right\}\right\rangle_t \approx S_{\mathcal{C},1}.\end{aligned} \quad (2.33)$$

Here the approximation $B_p/B = \epsilon/q \ll 1$ is used, where q is the safety factor and ϵ the inverse aspect ratio. The last step requires that the magnitude of the gradient of B is nearly constant on the flux surface and that $\widetilde{n}$ is only weakly up-down asymmetric. This shows that $\mathcal{C}$ is an inertial term, which is directly linked to the fluid equation. Note that $\mathcal{A}$ can also be obtained from the fluid equation if $\mathbf{E} = -\nabla\widetilde{\phi}$ is used in $Zen\mathbf{E}$. The curvature term $\mathcal{B}$ is not directly linked to the inertia $mn(\mathbf{u}\cdot\nabla)\mathbf{u}$ of the fluid equations. Rather, it is expected to enter through the viscous term.

In the remainder of this section a rough estimate of the magnitude of the source terms is given by using standard gyrokinetic ordering: $\widetilde{n} \sim \rho_* n_0, \widetilde{u}_{\parallel a} \sim \rho_* v_{\mathrm{th},a}, \widetilde{\phi} \sim \rho_* T/e, \nabla B \sim B/R$ and $\Omega_\perp \sim v_{\mathrm{th},i}/R$. The value of the magnetic field B is taken to be the same as on the magnetic axis and $v_{\mathrm{th},a} = \sqrt{2T/m_a}$ is the thermal velocity of species a. Furthermore the mass ratio $m_{Ra} = m_a/m$ is introduced, where m is the deuterium mass. The parallel length scale is of the order of the major radius R, while the perpendicular length scale is of the order of the ion gyro radius $\rho_i = mv_{\mathrm{th},i}/(eB)$. Using the above ordering in the Eqs. (2.26-2.28) yields

$$S^a_{\mathcal{A},1} \sim ZB\frac{n_0T}{R}\rho_*^2, \quad (2.34)$$

$$S^a_{\mathcal{B},1} \sim \sqrt{m_{Ra}} B \frac{n_0 T}{R} \rho_*^2, \tag{2.35}$$

$$S^a_{\mathcal{C},1} \sim m_{Ra} B \frac{n_0 T}{R} \rho_*^2. \tag{2.36}$$

All terms are force densities multiplied with the magnetic field strength B and are of second order in ρ_*. Note that the mass ratio appears only in the last two terms, likely making them small when considering electrons since $m_{Re} \approx 1/3600$. However, the electrons have a larger contribution to the current due to their low mass. Thus, especially the first term can yield a significant contribution when also considering the electron dynamics of the turbulence. In the following considerations the force exerted on the background is assumed to be $\rho_*^2 n_0 T/R$.

The ordering described above allows to predict the impact on neoclassical transport, as well as the current driven in a tokamak. A toroidal force F_t, like the one generated by the turbulent source terms, is balanced in the steady-state, usually either by a radial flux or, if applicable, electron-ion friction. Note that in the strict sense the forces introduced are parallel to the field but $B_t \approx B$ is a good approximation. Using the Lorentz force $\mathbf{F} = Ze n \mathbf{v} \times \mathbf{B}$ yields $F_t = Ze n v_r B_p$, where v_r is the radial velocity and B_p the poloidal magnetic field. Consequently, the radial velocity v_r^{vnl} driven by the turbulent source terms is

$$v_r^{\text{vnl}} = \frac{F_t}{ZenB_p} \sim \frac{nT}{enB_pR}\rho_*^2 = \frac{\rho_i B}{RB_p}\rho_*^2 \approx \frac{q}{\epsilon} v_{\text{th}} \rho_*^3. \tag{2.37}$$

The radial heat flux Q being mostly carried by the ions is the most important aspect of transport in terms of plasma confinement and can be written in diffusive form as $Q = n\chi\nabla T$, with thermal diffusivity χ. This flux also corresponds to a radial flow nv_rT, which can be compared to the radial velocity v_r^{vnl}. The flow driven by the temperature gradient is $v_r = \chi/L_T$, where $1/L_T = \nabla T/T$ is the temperature gradient length scale. Taking the banana-plateau ion thermal diffusivity $\chi \sim q^2 \epsilon^{-3/2} \nu_i \rho^2$ [3] as an approximation for the neoclassical transport yields

$$v_r^{\text{vnl}}/v_r^{\text{neo}} = \frac{\sqrt{\epsilon}}{q}\rho_* \frac{v_{\text{th}}}{R\nu_i} \frac{1}{R/L_T}, \tag{2.38}$$

where ν_i is the ion collision frequency. While ρ_* is a small parameter, the normalised collisionality $R\nu_i/v_{\text{th}}$ in high temperature plasmas is small as well, and thus the ratio $v_r^{\text{vnl}}/v_r^{\text{neo}}$ is not necessarily small under all conditions.

Lastly, the plasma current modifies the magnetic field configuration and more importantly in tokamaks limits the operation time, as it is mainly induced by a central solenoid. The externally driven current J_{ext} can be expressed through the poloidal field, using Ampere's law, as $J_{\text{ext}} = 2B_p/(\mu_0 r)$. The parallel force also drives a current $J_\parallel = en_e(u_{\parallel,i} - u_{\parallel,e})$, where the subscript i (e) denotes ion (electron) quantities. Here it is assumed that only the electrons are significantly accelerated, while the ions remain quasi-stationary due to their large mass. In a steady state the friction caused by electron-ion-collisions balances this parallel force:

$$F_\parallel - m_e n_e \nu_{ei}(u_{\parallel,i} - u_{\parallel,e}) = 0 \tag{2.39}$$

$$J_{\parallel} = \frac{eF_{\parallel}}{m_e \nu_{ei}} \tag{2.40}$$

This simple model allows us to estimate the magnitude of the effect on neoclassical transport and current in the plasma. In Table 2.1 cyclone base case parameters as well as device properties for ASDEX Upgrade (AUG) or ITER are employed to give the corresponding estimates.

Table 2.1. Estimation of the generated current $J_{\parallel}$ and modified transport due to the turbulent forcing terms. Cyclone base case parameters, as well as device properties for AUG and ITER are used.

	AUG	ITER
q	1.4	1.4
ϵ	0.19	0.19
R/L_T	6.9	6.9
$n/10^{19}\mathrm{m}^{-3}$	5	10
T/keV	1.5	8.0
B/T	2.5	5.3
R/m	1.65	6.2
ν_i/s^{-1}	200	32
$\nu_{ei}/10^3 s^{-1}$	34.1	5.5
$J_{\parallel}/J_{\mathrm{ext}}$	0.08	0.21
$v_r^{\mathrm{vnl}}/v_r^{\mathrm{neo}}$	0.10	0.11

Even though there is a ten percent change in the radial neoclassical transport, it is usually negligible compared to the turbulent transport. However, the change in current that is in the ten percent range of experimental accuracy, is significant, especially for the ITER scenario. Generating intrinsic current can be of great use for tokamak operation, as it allows for longer pulse length or potentially even steady state operation.

2.3. Numerical results

The current driven by the turbulent source terms is determined by first running a nonlinear simulation with the nonlinear gyrokinetic turbulence code GKW [65]. There the force, heat and higher order moments of the velocity nonlinearity are calculated and time averaged. The averages are added as source terms in the neoclassical equilibrium solver NEOART, which solves the flux surface averaged balance equations (2.16). The method of NEOART is nearly identical to the code NCLASS, for more details see Refs. [15, 88]. The current calculated with NEOART can then be compared with and without source terms, with the latter representing the bootstrap current. The parameters are compliant to the Cyclone Base Case (CBC), but with a moderate plasma rotation $\Omega_N = R_{\mathrm{ref}}\Omega/v_{\mathrm{thref}} = 0.1$. This plasma rotation is neglected in the neoclassical description of the system. However, the modification to the particle and heat fluxes is only of

the order $(\Omega_N)^2$ and thus negligible [87]. A deuterium-electron plasma is simulated, assuming a circular flux surface with safety factor $q = 1.4$, inverse aspect ratio $\epsilon = 0.19$ and magnetic shear $\hat{s} = 0.78$. The gradient length scales are $R/L_{Ti} = R/L_{Te} = 6.9$ for ion and electron temperature respectively and $R/L_{ni} = R/L_{ne} = 2.2$ for the density. The GKW simulations are nonlinear and electrostatic with kinetic electrons, using 83 radial and 21 toroidal modes, with a maximum poloidal wave vector $k_\theta \rho = 1.4$. The grid sizes are $N_s = 16$ along the field line and $N_{v_\parallel} = 64$, $N_\mu = 9$ for the velocity space. The device parameters used in NEOART are given in Table 2.2.

Table 2.2. Device parameters used in simulations.

Parameters	DIIID	AUG	ITER
$n/10^{19}\mathrm{m}^{-3}$	1.9	5	10
T/keV	0.77	1.5	8.0
B/T	1.57	2.5	5.3
R/m	1.65	1.65	6.2

Without an external electric field and the turbulent drive NEOART calculates the banana plateau bootstrap current J_{bs}, as shown in Fig. 2.2 for different temperature gradients. It is found to be in good agreement, with the analytic approximation in Ref. [89].

Note that the turbulent source terms are strongly fluctuating and require long averaging times, making the simulations computationally expensive. The statistical error can be estimated by taking the most important contribution $S^{\mathrm{el}}_{\mathcal{A},2}$ and determining the error of the mean using a

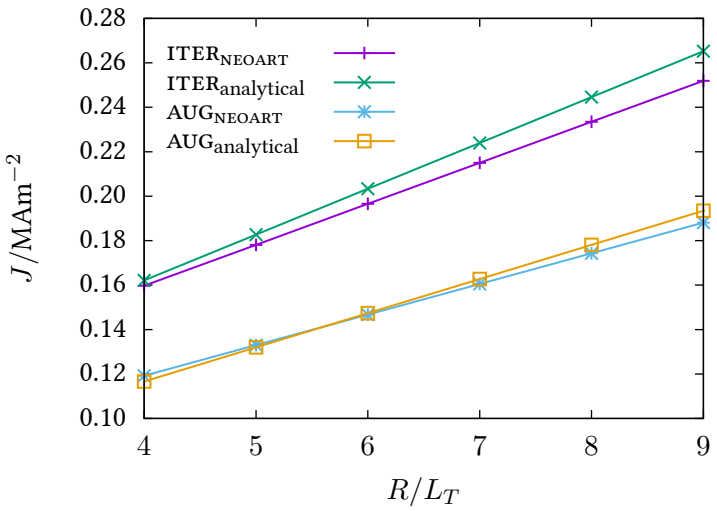

Figure 2.2. Benchmark of Bootstrap current calculated by NEOART compared to analytical approximation as a function of temperature gradient for AUG and ITER device parameters.

five part average. Varying the input value for NEOART according to the error range yields a relative error of less than 10% for the current driven by turbulence in the kinetic CBC simulation, leading to reasonably accurate results. The magnitude of the different contributions and respective orders in the velocity are shown in Fig. 2.3 as well as a comparison between different devices. The turbulence driven current is of the same magnitude as the bootstrap current and most current is driven by the parallel fluctuations of density/temperature and potential. The device size only weakly affects the result as the changed properties largely balance each other. The turbulent forcing ($\sim \rho_*^2 nT/R$) is smaller for larger reactors but the electron-ion collision

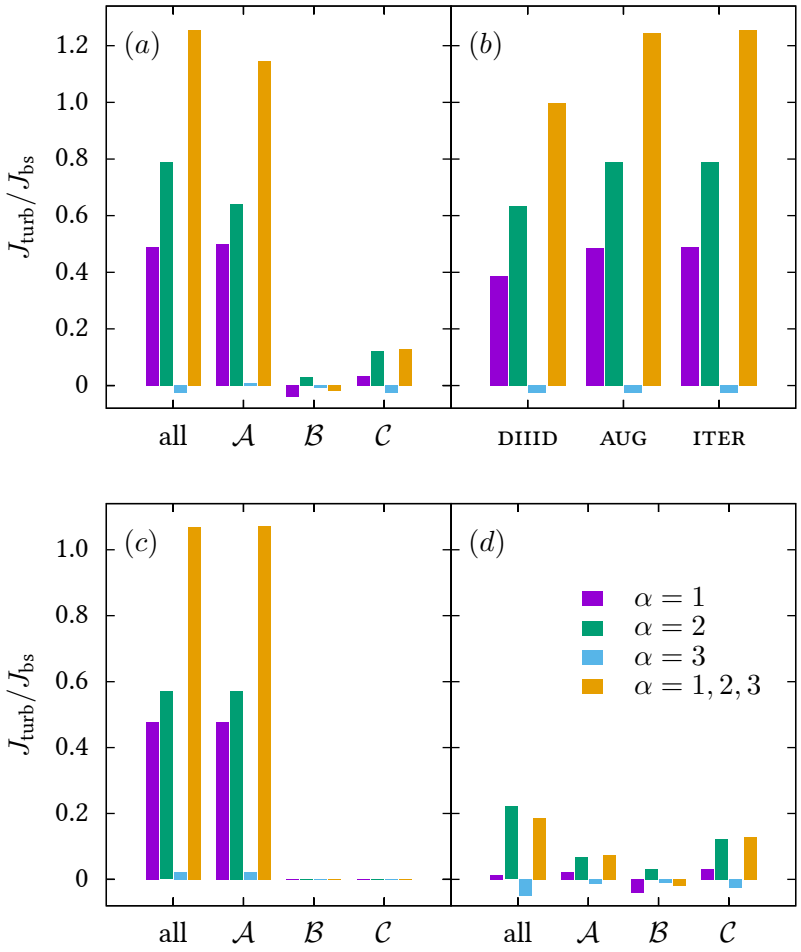

Figure 2.3. The ratio of turbulence driven current J_{turb} to the bootstrap current J_{bs}. The contribution of each order α in the velocity moment as well as the total is shown for each individual term. (a) Kinetic cyclone base case with ITER parameters. (b) Comparison for different devices. (c) Only electron source terms and (d) only ion source terms for ITER parameters.

frequency is reduced as well and compensates the change. Furthermore, the current drive associated with the heat flux balance is the most important contribution. This can be expected, as the source terms are calculated in ITG turbulence where heat flow is the dominant transport channel. The force exerted by the heat flux balance scales with the heat flow, and thus also the temperature gradient, which will be shown later on. The bottom panel of Fig. 2.3 shows electron and ion drive separately, showing that the electron contribution from $\mathcal{A}$ is dominant, which agrees with the mass scaling in Eqs. (2.34 - 2.36). The ion terms drive less than 20% of the current, which is almost exclusively due to their high contribution to the heat flux.

Fig. 2.4 shows the current driven in dependence of the temperature and density gradient for runs with ITER and CBC parameters. As expected the current increases with the temperature gradient as the turbulent transport and especially the heat flux is increasing. The dependence on the density gradient is non-monotonic. The physical reason for this is at present unclear. While the importance of the heat flux shows the necessity to consider the higher orders of the parallel balance equations, the current driven in a realistic scenario is much lower since the heat flux in nonlinear gyrokinetic turbulence simulations with CBC parameters is much larger than the experimental relevant heat flux levels. The current driven scales linearly with the heat flux as can be seen in Fig. 2.5, where an estimate for the heat flux in ITER is represented by the vertical black line which is estimated by

$$Q = \frac{0.2 P_{\text{fusion}}}{(2\pi R)^2} \frac{\epsilon}{\epsilon_{\text{core}}^2} \approx 0.2 \frac{\text{MW}}{\text{m}^2}, \tag{2.41}$$

considering that only 20% of the fusion power ($P_{\text{fusion}} = 500$ MW) is stored in the α par-

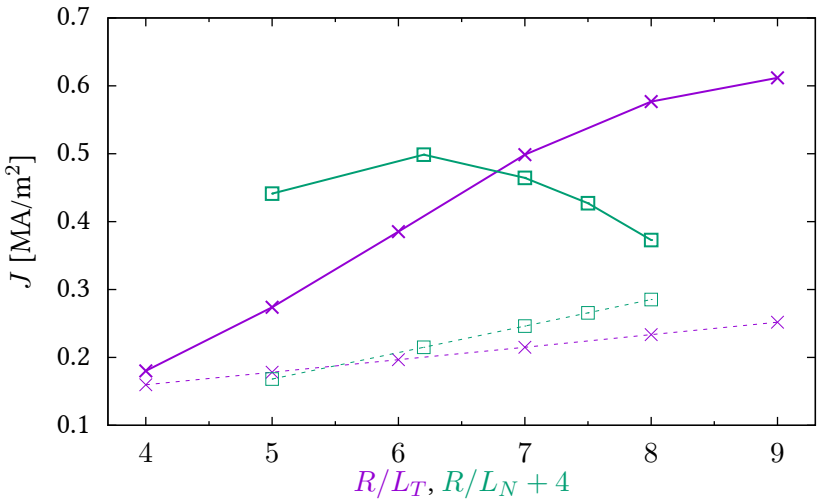

Figure 2.4. Bootstrap current (dashed lines) and current with turbulent drive (solid lines) as a function of R/L_T (crosses) with fixed $R/L_n = 2.2$ and as a function of R/L_n (squares) with fixed $R/L_T = 7.0$. The other parameters used are those of the kinetic cyclone base case and the ITER case.

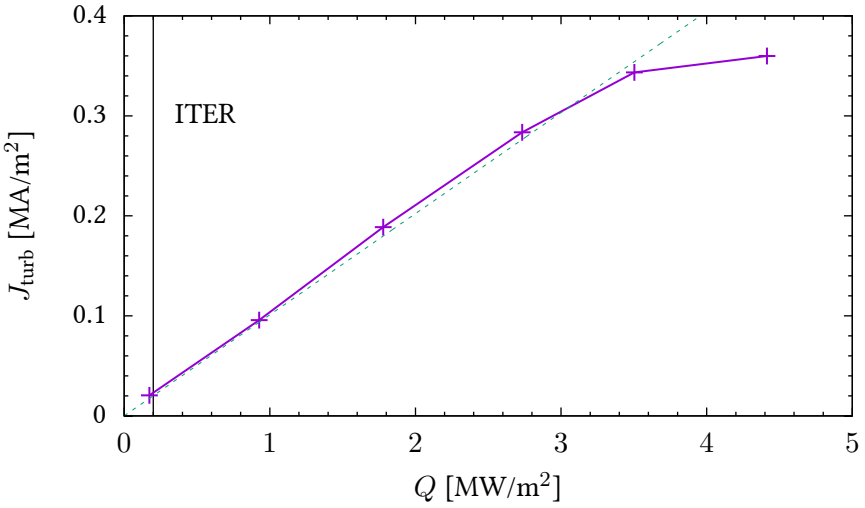

Figure 2.5. Current driven by ITG turbulence as a function of heat flux, using the temperature gradient scan shown in Fig. 2.4. The dashed dark green line is a linear fit of the data and the vertical black line shows an estimation of the expected heat flux in an ITER scenario.

ticles and assuming that the power is uniformly generated in the core region with radius $r = \epsilon_{\text{core}} R = 0.25R$. This leads to a realistic current, which is one order of magnitude smaller than in the cyclone base case. However, ten percent of the bootstrap current is still significant for high intrinsic current scenarios.

For practical purposes it is more interesting to compare the current generated to the total current required for present tokamak operation, i.e. including an external field E. The loop voltage $U = ER$ in NEOART is chosen such that the current obtained corresponds to the current required for the poloidal magnetic field, $J_{\text{ext}} + J_{\text{bs}} = 2B_p/(\mu_0 r) \approx 2qB/(\mu_0 R)$. Adding the turbulent source terms gets the actual increase in total current, shown in Table 2.3 for the kinetic cyclone base case which is found to be in good agreement with the estimate in Section 2.2. Table 2.3 also shows the impact of a rotation gradient, which provides a strong symmetry breaking mechanism further increasing the turbulent current.

Scaling down the values given in Table 2.3 to realistic heat flux levels, an intrinsic current driven by turbulence of 0.03 MA/m^2 might be achieved for an ITER scenario, which still amounts to a few percent additional current. Higher values can be achieved for operational scenarios with high rotation since the drive is nearly linear in Ω and the simulations described in this chapter use a relatively low rotation of $\Omega = 0.1$. Alternatively, a rotation gradient provides a strong symmetry breaking, further increasing the current driven by turbulence. For a still realistic value of $u' = -1$ the turbulent current is nearly tripled, thus allowing up to ten percent additional current generated by the turbulence.

Table 2.3. Loop voltage U and current J in MA/m^2 for AUG or ITER using kinetic cyclone base case parameters with $R_{\text{ref}}\Omega/v_{\text{thref}} = 0.1$. A rotation gradient $u' = -R_{\text{ref}}^2\nabla\Omega/v_{\text{thref}}$ significantly increases J_{turb}. However, the turbulent current and thus also the relative current increase for a realistic heat flux is one order of magnitude smaller.

Device		AUG	ITER
U/V		0.1	0.017
J_{bs}		0.16	0.21
$J_{\text{bs}} + J_{\text{ext}}$		1.71	1.0
$J_{\text{turb}} + J_{\text{bs}} + J_{\text{ext}}$	$u' = 0$	1.91	1.27
	$u' = -1$	2.28	1.79
relative increase	$u' = 0$	12%	27%
	$u' = -1$	33%	79%

2.4. Conclusions

The parallel velocity nonlinearity in the gyrokinetic equation couples with the neoclassical background and can drive a substantial current, provided the symmetry along the magnetic field is broken, for example due to background rotation. The current driven is mostly linear in the turbulent heat flux and even when scaling down to realistic values an increase of a few percent of total current can be expected in an ITER scenario. As an upper limit for scenarios with strong rotation or strong rotation gradient up to ten percent increased total current can be achieved. However, the model used only aims to identify the effect and establish the order of magnitude. Corrections can be expected from other symmetry breaking mechanisms like the stationary E×B flow associated with the rotation gradient, or the coupling with the neoclassical background, as described in Ref. [73]. Furthermore it is interesting to include the mechanism from Ref. [79], which is related to the electromagnetic response or profile effects, which are not treated here. For a proper quantitative prediction as the next possible step all these effects have to be included to study if they partly cancel each other or possibly further increase the current driven.

3. Scaling of intrinsic rotation with neoclassical flow

Intrinsic rotation, i.e. plasma rotation without an external momentum source, has been observed in multiple tokamak experiments [90] and is particularly important in reactor plasmas where the external torque will be comparatively small. Significant toroidal flow gradients can, by means of flow shearing, stabilise plasma turbulence and thus improve confinement [37, 39, 40, 91]. As turbulence drives the majority of heat and particle transport in magnetic fusion devices, understanding the generation and transport of toroidal rotation has received considerable interest [85, 92].

It is conventionally assumed, that the neoclassical and turbulent description of a plasma can be treated separately. This is in many cases a reasonable approximation because of the strong separation in length and time scales, with the neoclassical solution having length scales of the order of the plasma size and a timescale determined by the collision frequency, while the turbulent dynamics have length scales of the order of the gyroradius and evolve on the ion transit time. Turbulent transport is the dominant loss channel for thermal energy in tokamak plasmas, while several other aspects like current and resistivity are governed by neoclassical effects. A popular example is the intrinsic current called the bootstrap current driven by pressure gradients [11–13].

Recently the impact of the neoclassical modifications to the background distribution function, used in turbulent transport calculations, has been the object of a number of studies showing the relevance for the generation of intrinsic rotation [69–75]. Neoclassical effects are a possible drive of intrinsic rotation and the underlying physical mechanisms, the breaking of the parity symmetry [85, 93], is connected to the neoclassical toroidal particle and heat flow [71].

This chapter aims to provide insight in two different ways: firstly, by showing a large scale parameter analysis of the momentum transport driven by the neoclassical modifications to the background and exploring simple scaling models; secondly, a rough estimate of the equilibrium rotation gradient depending solely on the neoclassical first order flow is given.

The chapter is structured as follows. In Section 3.1 the implementation and numerical setup is explained in more detail. Section 3.2 shows simulation results and discusses the scaling of the momentum transport.

3.1. Numerical setup

The simulation process is split into two steps. First the neoclassical background is calculated by the neoclassical equilibrium solver NEO [94], which solves the drift kinetic equation. The

neoclassical modifications to the Maxwellian background distribution are then used in the gyrokinetic flux tube code GKW [65]. The reader is referred to Ref. [73] for details on the coupling of the codes and the modifications to the turbulence evolution due to the neoclassical background. Like in Ref. [73] the neoclassical modifications to the background are assumed constant because the time scale of neoclassical flows is significantly longer than the time scale of turbulence. Furthermore their cross–coupling is not considered, i.e. the influence of the turbulence on the neoclassical background is neglected.

In the following all quantities are normalised, unless explicitly stated otherwise. The full set of equations solved and the normalisations can be found in Refs. [65, 73]. The basic parameter set used is that of the Cyclone Base Case (CBC): Circular flux surfaces, safety factor $q = 1.4$, magnetic shear $\hat{s} = 0.8$, inverse aspect ratio $\epsilon = 0.18$ (of the $r/a = 0.5$ flux surface). Ion and electron temperatures and densities are equal, $T_i = T_e$ and $n_i = n_e$. The logarithmic gradients are $R/L_n = R\partial \ln n/\partial r = 2.2$ for the density and $R/L_{T_i} = R/L_{T_e} = 6.9$ for the ion and electron temperature. The grid resolution for simulations performed with NEO is, $N_E = 10, N_\zeta = 19, N_\Theta = 41$ for the energy, angular polynomials and in the poloidal direction respectively. In GKW the grid sizes are $N_s = 30$ points along the field, $N_{v_\parallel} = 64$ (96 for $\epsilon = 0.05$) and $N_\mu = 16$ grid points for the parallel velocity and magnetic moment respectively. For the radial resolution $N_x = 21$ modes are used. The local flux tube model is used [64], which is periodic in both the radial and binormal directions and shear-periodic in the parallel direction. The simulations are linear with kinetic electrons.

While the basic case is the Cyclone Base Case, the turbulent momentum flux driven by the neoclassical background is investigated for a large parameter space, listed in Table 3.1. Where α_x are the normalised second derivatives of the ion (electron) temperature T_i (T_e) or the density n at the flux surface, e.g. $\alpha_{T_i} = 1/(R/L_{T_i})^2 R^2 \partial^2 T_i/\partial r^2$. This second derivative significantly influences the gradient of the first order parallel flow. As multiple parameters are changed simultaneously they were grouped in three arbitrary groups to keep the number of simulations achievable. Simulations are performed for all combinations of a group, e.g. "geometry", for different ion-ion collision frequencies ν_{ii} while the remaining parameters are set to the CBC value.

Assuming that the symmetry breaking caused by the first order neoclassical flow and its gradient are the dominant drive of the intrinsic rotation, it is possible to develop a simple scaling model. Following Ref. [85] the flux of toroidal momentum Π, normalised by the heat flux Q, can be written like,

$$\Pi/Q = \chi_{\varphi E} u'_{\parallel E} + \chi_{\varphi N} u'_{\parallel N} + V_{\varphi E} u_{\parallel E} + V_{\varphi N} u_{\parallel N} + \Pi_{\text{other}}, \tag{3.1}$$

with the addition of distinguishing the neoclassical part (subscript N) and the part connected with the radial electric field (subscript E). Thus, the parallel flow velocity $u_\parallel = u_{\parallel E} + u_{\parallel N}$ and its gradient $u'_\parallel = u'_{\parallel E} + u'_{\parallel N}$ as well as the corresponding momentum diffusivities χ_φ and momentum pinch coefficients V_φ treat the neoclassical and electric field part separately. All other contributions to the momentum transport, e.g. due to the heat flux or the background potential, are contained in Π_{other}.

Table 3.1. The parameter space covered in the simulations. The reference quantities v_{thref} for the thermal velocity and R_{ref} for the major radius are used for the normalisation of the ion-ion collision frequency ν_{ii} and α_x are the normalised second derivatives of the temperature or density.

Parameter	Values	"classification"
$\nu_{ii}/(10^{-2}/v_{\text{thref}}/R_{\text{ref}})$	$0.2, 2, 20$	
ϵ	$0.05, 0.18, 0.30$	geometry
q	$1.4, 2.2, 3.0$	geometry
$\hat{s}$	$0.2, 0.8, 1.5$	geometry
R/L_{T_i}	$4.0, 6.9, 9.0$	gradients
R/L_{T_e}	$4.0, 6.9, 9.0$	gradients
R/L_n	$0.0, 2.2, 4.0$	gradients
α_{T_i}	$0.0, 1.0, 2.0$	profile
α_{T_e}	$0.0, 1.0, 2.0$	profile
α_n	$0.0, 1.0, 2.0$	profile

3.2. Results

The first set of simulations uses the full neoclassical background distribution calculated by NEO. Without bulk rotation (or rotation gradient) connected with the electric field, Eq. 3.1 is then reduced to

$$\Pi/Q = \chi_{\varphi N} u'_{\parallel N} + V_{\varphi N} u_{\parallel N} + \Pi_{\text{other}}. \tag{3.2}$$

Fig. 3.1 shows the flux ratios driven by the neoclassical background as a function of the neoclassical flow and flow gradient according to Eq. (3.2). Each point is a parameter tuple of the indicated group in Table 3.1. There is a significant amount of scatter in the data, especially for points with different aspect ratio or magnetic shear. Using a reduced parameter set without these parameters significantly changes the fit values of the coefficients. Not all aspects of the momentum transport generation can be covered by the scaling law which only uses the quantities directly responsible for the symmetry breaking. However, the data does follow a trend and the scaling can be used for a rough approximation. Note that in spite of χ_φ being one order of magnitude smaller the flow gradient still is the most significant contribution, as there is much more variation compared to the flow (standard deviation of 0.50 to 0.05).

The second set of simulations does not use the neoclassical background but sets the background rotation and its gradient to match the neoclassical flows. Fig. 3.2 again shows the flux ratios and a similar linear dependence with significant outliers as found for the full neoclassical simulations is found.

For the second simulation set, Eq. 3.1 reduces to

$$\Pi/Q = \chi_{\varphi E} u'_{\parallel E} + V_{\varphi E} u_{\parallel E} + \Pi_{\text{other}}. \tag{3.3}$$

Assuming that the contributions from flow and flow gradient are linearly independent, two simulations are run for each data point in this set: one where the corresponding neoclassical flow (from the first simulation set) is input as a background rotation and one using the same procedure for the flow gradient. This method makes all coefficients in Eq. 3.1 accessible by fitting the data.

Combining both simulation sets, it is possible to predict the equilibrium rotation gradient driven by the neoclassical background modifications. If there is no external momentum applied, the momentum flux has to go to zero, i.e. a rotation gradient $u'_{\parallel eq}$ has to balance the flux generated by the neoclassical first order flow. Assuming that the momentum diffusivities are similar for the neoclassical and the electric field part, i.e. $\chi_\varphi = \chi_{\varphi E} \approx \chi_{\varphi N}$, which is justifiable as can be seen in Fig. 3.2, it is possible to predict the equilibrium gradient driven by the neoclassical flow using Eq. 3.1.

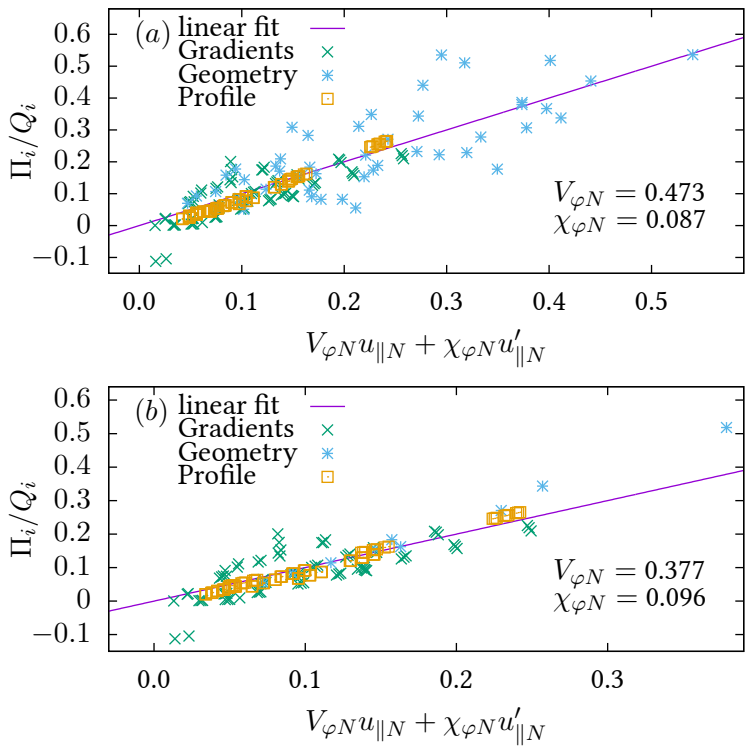

Figure 3.1. The ratio of the radial momentum flux (Π_i) to the radial heat flux (Q_i), for simulations with the full neoclassical background, as a function of the neoclassical first order flow $u_{\parallel N}$ and its gradient $u'_{\parallel N}$. The momentum diffusivity $\chi_{\varphi N}$ and the momentum pinch coefficient $V_{\varphi N}$ are determined by a least square fit, assuming the model in Eq. (3.2). (a) Every point is a different parameter combination of the indicated group (see Table 3.1). (b) Reduced set of geometry parameters, where $\epsilon = 0.18$ and $\hat{s} = 0.8$ are not varied.

$$0 = \chi_\varphi \underbrace{\left(u'_{\parallel E} + u'_{\parallel N}\right)}_{u'_{\parallel eq}} + V_{\varphi E} u_{\parallel E} + V_{\varphi N} u_{\parallel N} + \Pi_{other} \tag{3.4}$$

$$u'_{\parallel eq} = -\frac{1}{\chi_\varphi}\left(V_{\varphi N} u_{\parallel N} - V_{\varphi E} u_{\parallel E} - \Pi_{other}\right) \tag{3.5}$$

While the $V_{\varphi E} u_{\parallel E}$ contribution does not drive a momentum flux in most cases (see Fig. 3.3), the Coriolis pinch will still lead to a peaking of the toroidal velocity profile and thus modify the rotation profile [6]. However, without knowledge of the plasma edge in the local model used in this work the absolute magnitude of the Coriolis pinch is not accessible and is neglected in the following as the focus is on the effect of the neoclassical modifications to the background distribution. For a standard case with $u_{\parallel N} \approx 0.1$ and the coefficients from Fig. 3.1 this leads

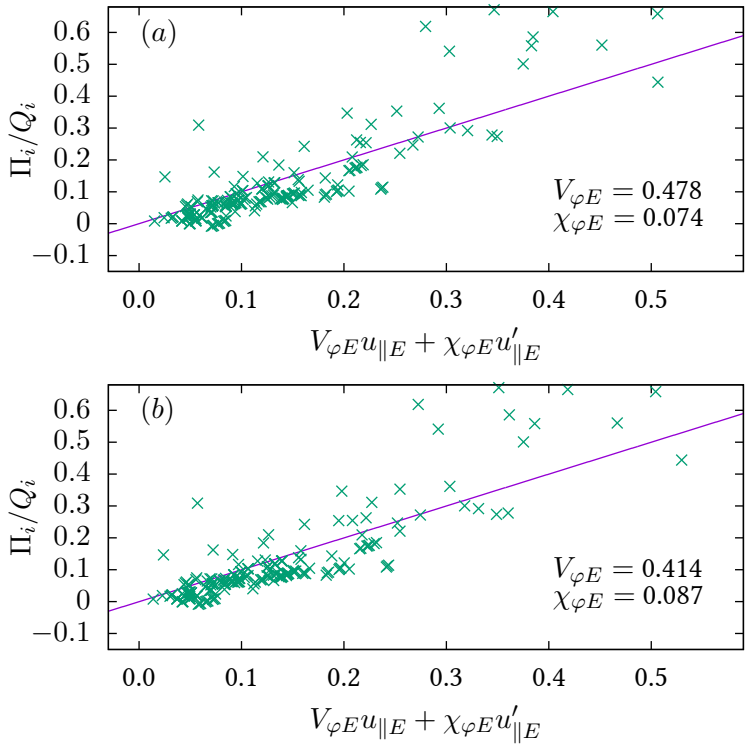

Figure 3.2. The ratio of the radial momentum flux (Π_i) to the radial heat flux (Q_i), for simulations without the neoclassical background, as a function of background rotation and rotation gradient. The input rotation and gradient are set to match the flow that would be driven by the neoclassical background. (a) The momentum diffusivity $\chi_{\varphi E}$ and the momentum pinch coefficient $V_{\varphi E}$ are determined by a least square fit, assuming the model in Eq. (3.3). (b) $\chi_{\varphi E}$ is fixed to the value of $\chi_{\varphi N}$ for the fit, showing the validity of the assumption of equal momentum diffusivity made for Eq. (3.5). The fit is qualitatively unchanged and the sum of squared residuals is virtually the same.

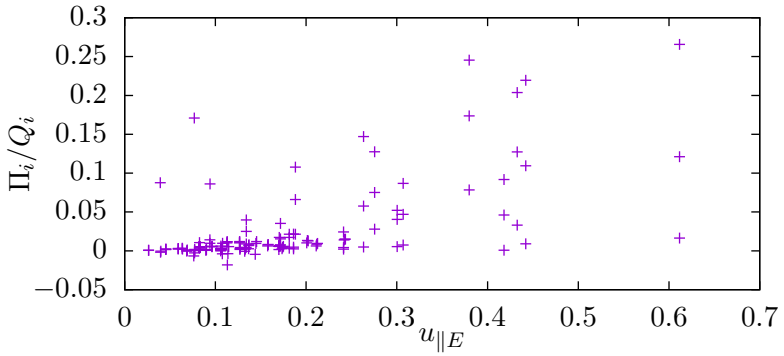

Figure 3.3. The ratio of radial momentum flux (Π_i) to the radial heat flux (Q_i) against the background rotation. The input rotation is set to match the flow that would be driven by the neoclassical background. In most cases no momentum flux is driven by the toroidal flow.

to

$$u'_{\parallel eq} \approx \frac{V_{\varphi N}}{\chi_\varphi} u_{\parallel N} \sim 0.5, \tag{3.6}$$

which is a sizeable contribution to the rotation gradient, which usually is of the order of one. However, with the significant amount of scatter in the data this rather serves as a magnitude prediction rather than a detailed scaling law. Nevertheless the quality of the prediction for low collisionality and regular magnetic shear and aspect ratio is significantly improved.

4. Damping of zonal modes through turbulent momentum transport

Zonal flows are latitude parallel, toroidally symmetric shear flows. They are observed in nature as well as in the laboratory. Popular examples are atmospheric phenomena like jet streams or the distinct belt structure of Jupiter. Zonal flows exhibit a self-regulating character as they work to reduce their drive, in the above example a temperature or pressure difference in the atmosphere. In laboratory fusion plasma experiments, turbulence drives a zonal flow through nonlinear coupling. The zonal flow in turn reduces the turbulence through eddy shear stabilisation [20]. Zonal flows lead to a nonlinear upshift of the temperature gradient threshold for turbulence generation, known as the Dimits shift [18]. Recent investigations [19, 21, 43] have shown that this upshift can be further enhanced through the formation of staircase structures [24, 41, 42]. The nonlinear upshift is beneficial for energy confinement since the turbulent transport sets in at higher temperature gradients when compared with linear stability predictions and, consequently, has been studied extensively.

The drift wave-zonal flow system is often described through a predator-prey model [20]. In this model the zonal flow is driven by the turbulence through the modulation instability [27, 95], and regulates the turbulence through E×B shearing [39, 40, 91]. The magnitude of the obtained turbulence reduction through E×B shearing depends critically on the saturation of the zonal flows, for which two mechanisms have been identified: collisional damping [21, 32] and Kelvin Helmholtz tertiary instabilities [33].

In this chapter a new mechanism, the damping of the zonal flow through turbulent momentum transport, is introduced, and shown to be relevant for the description of sufficiently long lived zonal flow structures. The basic idea is relatively simple. In tokamak plasmas the poloidal plasma rotation connected with the radial electric field of the zonal flow is not divergence free due to the inhomogeneity of the magnetic field. An initial perturbation in the zonal ion density then excites a geo-acoustic mode (GAM), that undergoes collisionless damping on the ion transit time, resulting in a final state that has a residual zonal flow [96]. The latter residual flow is the combination of the E×B velocity due to the radial electric field, and a parallel flow that removes the compression. Whether this final state is relevant for all zonal flows in the turbulent state is questionable, since it needs several transit times to develop and might therefore not be relevant for rapidly fluctuating zonal flows. Large wavelength zonal flows, however, are observed to be long lived, and can be expected to be well described by the residual zonal flow solution. This is particularly true for the staircase zonal flow structures that can live for many hundreds or thousands of transit times. For the residual zonal flow solution, also the evolution of the parallel flow needs to be considered, and this flow is affected by the turbulence through parallel momentum transport. It has been shown that a parallel dissipation can damp

the zonal flow relatively effectively [19], and it can be expected that the turbulent transport of parallel momentum will have a similar effect. Therefore, in a turbulent state the zonal flow is not merely driven by the Reynolds stress connected with the fluctuating perpendicular E×B velocity, it will also be damped by the stress connected with the fluctuations in the parallel velocity. This is different from the predator-prey model, in which the saturation mechanism of the zonal flow is independent of the turbulent dynamics.

The remainder of this chapter is structured as follows. In Section 4.1 some back of the envelope estimates of the magnitude of the effect are made. Section 4.2 then shows the effect by performing the Rosenbluth-Hinton test with the effect of the turbulence modelled by a diffusion of parallel momentum. Section 4.3 assesses the relevance for the turbulent state by eliminating the nonlinear convection of parallel momentum while maintaining the turbulent transport of density and temperature. Finally, conclusions are formulated in Section 4.4.

4.1. Reduced model

Below a qualitative description of the residual zonal flow state is given, after which the zonal flow damping rate due to the parallel momentum transport is estimated and compared with the growth rate due to the modulation instability. The focus is on the long term quasi-stationary state, and the GAM oscillation will not be considered.

Assume a zonal ion density perturbation is excited through the interaction of turbulent modes. The electrons can not retain quasi-neutrality through their motion along the magnetic field and, consequently, a large radial electric field quickly builds up until the ion polarisation density balances the initial ion density perturbation. The radial electric field ($E_r(0)$), however, also modifies the orbits of the particles. In particular, trapped particles can not be rotated in the poloidal direction by the radial electric field. They must rotate toroidally with a velocity

$$v_{tr} = \frac{E_r}{B_p}, \tag{4.1}$$

where B_p is the poloidal magnetic field, to satisfy the force balance. The velocity above is connected with a shift of the trapped particle domain in velocity space, with the domain centred around v_{tr} (Centrifugal effects will furthermore widen the trapping domain [66, 67], but will be neglected here). The shift in the trapped particle domain transforms some trapped particles to passing, while some originally passing particles will become trapped. This generates a rather complicated distribution function where the flow of trapped particles is partly balanced by a back flow in the passing domain carried by barely passing particles [97].

The modification in the distribution function due to the initial radial electric field (E_r^0) occurs on the time-scale of the bounce time and, due to the finite radial extend of the trapped particle orbits, the process is connected with a radial current, that will modify the radial electric field. The residual electric field (E_r^∞) that remains has been calculated by Rosenbluth and Hinton [96]

$$E_r^\infty = \frac{1}{1 + 1.6q^2/\sqrt{\epsilon}} E_r^0. \tag{4.2}$$

Important for the mechanism discussed in this chapter is that the final state has a finite parallel flow. This can be directly understood from the conservation of angular momentum. The original radial electric field E_r^0, corresponds to a toroidal angular momentum connected with the toroidal component of the E×B velocity

$$L^0 = n_i \frac{R E_r^0 B_p}{B^2} \approx n_i \frac{\epsilon}{q} \frac{R E_r^0}{B}, \tag{4.3}$$

where $B_p/B \approx \epsilon/q$ was used. Assuming the final state has a parallel flow

$$L^\infty = n_i \frac{R B_t}{B} u_\parallel + n_i \frac{\epsilon}{q} \frac{R E_r^\infty}{B}, \tag{4.4}$$

using the conservation of angular momentum, $B_t \approx B$, and substituting the result of Rosenbluth and Hinton, one obtains

$$n_i u_\parallel = 1.6 q \sqrt{\epsilon} n_i \frac{E_r^\infty}{B}. \tag{4.5}$$

The toroidal component of this parallel flow is much larger than the toroidal component of the E×B flow ($n_i E_r^\infty B_p / B^2 \approx n_i \epsilon E_r^\infty / (qB)$, but smaller by a factor ϵ compared with the flow in the trapped particle population

$$n u_\parallel|_{\mathrm{tr}} = \frac{q}{\sqrt{\epsilon}} n_i \frac{E_r^\infty}{B}, \tag{4.6}$$

where the density of trapped particles is approximated by $n_{\mathrm{tr}} = \sqrt{\epsilon} n_i$. This shows that most of the trapped particle flow is indeed compensated by a back flow of passing particles.

The Reynolds stress, that drives the zonal flow, does not modify the total angular momentum. Rather, angular momentum is radially transported, generating a local angular momentum perturbation that integrates to zero when the whole radial domain is considered. If the zonal flow is sufficiently long lived, the quasi-stationary state is described by the residual solution, and the electric field is accompanied by a stationary parallel flow, with the latter generating the dominant contribution to the toroidal angular momentum. In a turbulent state toroidal angular momentum is transported radially

$$\frac{\partial L(r)}{\partial t} + \nabla \cdot [\chi_\phi \nabla L] = 0, \tag{4.7}$$

where χ_ϕ is the transport coefficient. We neglect contributions from the pinch term as well as residual stresses and consider only diffusive transport in the model, since it is the dominant transport channel for small length scale systems. In the following it is assumed that the diffusion coefficient can be well approximated by the diffusion coefficient that is calculated for a background flow gradient [84], and which for ITG turbulence can be reasonably well approximated by the ion heat conduction coefficient since the Prandtl number is generally found to be of the order 0.7 and varies only slightly when changing plasma parameters like temperature gradient [85, 98]. It is furthermore assumed that the diffusive transport is not a strong function of the velocity space coordinates and is thus roughly equal for trapped and passing particles. This is a reasonable assumption for the ion temperature gradient (ITG) mode due to its fluid

character. Since the toroidal flow of the trapped particles is directly related to the radial electric field, the transport of angular momentum reduces the radial electric field accordingly and Eq. (4.7) yields

$$\frac{\partial E_r}{\partial t} = \nabla \cdot [\chi_\phi \nabla E_r]. \tag{4.8}$$

We proceed by considering a zonal flow described by a single Fourier mode $\phi = \phi_A \exp[\mathrm{i}k_{ZF}x + \gamma t]$, to obtain the damping rate

$$\gamma = -\chi_\phi k_{ZF}^2. \tag{4.9}$$

In the following only normalised quantities will be used. The transport coefficient is normalised with the gyro-Bohm diffusion $\rho^2 v_{th}/R$, where $\rho = m v_{th}/eB$ is the ion Larmor radius, $v_{th} = \sqrt{2T/m}$ is the thermal velocity, and R is the major radius. The zonal flow radial wave vector k_{ZF} is normalised with the ion Larmor radius, and the damping rate is normalised with respect to v_{th}/R. The normalisation leaves the equation above unchanged. The equation above gives the damping rate of the zonal flow through the parallel momentum transport, but does not include the driving term due to the modulation instability since the drive enters in the perpendicular dynamics over the negative viscosity effect. In toroidal geometry an expression for the growth rate of the zonal flow was derived in Ref. [27] and adding this to the growth / damping rate one obtains (neglecting a numerical factor of order unity)

$$\gamma = \epsilon^{1/4} k_{ZF} k_y \sqrt{I}/q - k_{ZF}^2 \chi_0 I \tag{4.10}$$

where $I = (e\phi/T\rho_*)^2$ is the turbulence intensity, with ϕ the fluctuating potential, $\rho_* = \rho/R$ is the normalised Larmor radius, and k_y is the wave vector of the turbulence (normalised to the Larmor radius). To bring out the correct scaling of the damping term, the momentum transport coefficient has furthermore been expressed in the turbulence intensity $\chi_\phi = \chi_0 I$, where χ_0 is a coefficient of order unity.

The following observations can be made:

• The damping rate scales with the zonal flow wave vector squared, and is quite substantial. Assuming $\chi_\phi = \chi_0 I \approx 1$, even a long wavelength zonal flow $k_{ZF} = 0.1$ has a damping rate $\gamma = -0.01$. This is substantially larger than the collisional damping for realistic parameters [21]. The damping rate, however, does not scale with the zonal flow intensity, and therefore modifies the growth and possibly stabilises the modulation instability, but does not provide a saturation mechanism.

• The scaling of the damping rate with turbulence intensity and zonal flow wave vector is different when compared with the scaling of the growth rate of the modulation instability. In particular, for small intensities ($I \ll 1$) the modulation instability dominates, while for strongly turbulent systems the damping can be dominant. This suggest a threshold in the turbulent intensity (I_t) above which the zonal flow of a certain wavelength is suppressed

$$I_t = \frac{\sqrt{\epsilon} k_y^2}{\chi_0 k_{ZF}^2 q^2} \tag{4.11}$$

• Shorter wavelength zonal flows are damped more strongly. Stability of the residual zonal

flow is obtained for

$$k_{ZF} > \sqrt{\frac{\epsilon^{1/2} k_y^2}{\chi_0^2 q^2 I}} \tag{4.12}$$

for typical values $k_y^2 = 0.04$ $\chi_0 = 1$, $I = 1$, $q = 1.4$ and $\epsilon = 0.19$, one obtains stability for $k_{ZF} > 0.09$, which is a relatively long wavelength zonal flow. Note that it does not mean that the modulation instability can not be effective in driving zonal flows at short wavelengths. Damping occurs only for sufficiently long lived zonal flows, that can be described by the residual zonal flow state. It does however suggest that the residual zonal flow may play no significant role in well developed turbulence of sufficient intensity.

• The physics mechanism outlined above is possibly relevant for staircase formation. Staircases form only at sufficiently small turbulence intensity [43], and are large wavelength long lived structures. Both the long wavelength nature of the staircase structure, as well as its occurrence in low turbulent states, is consistent with the mechanism outlined above.

4.2. Rosenbluth Hinton test

The reduced model presented in the previous section predicts a damping of the zonal flow through angular momentum transport. The validity of the model is tested in this section by performing a "Rosenbluth-Hinton-test" [96] including a model diffusion term for angular momentum in the gyrokinetic equation. The toroidal angular momentum of the residual zonal flow state was shown to be dominated by the parallel flow component, which in gyrokinetic theory can be expressed as

$$L = \left\{ \frac{mRB_t}{B} \int d^3v \, v_\parallel f \right\}, \tag{4.13}$$

where $f(\mathbf{X}, v_\parallel, \mu)$ is the distribution function with gyrocentre position $\mathbf{X}$, velocity parallel to the magnetic field $v_\parallel$ and magnetic moment μ. The curly brackets denote the flux-surface average. The radial momentum diffusion

$$\frac{\partial L}{\partial t} = D \frac{\partial^2 L}{\partial x^2}, \tag{4.14}$$

can then be modelled by adding the term

$$\frac{\partial f}{\partial t} \stackrel{+}{=} D \frac{\partial^2 f_a}{\partial x^2} = -D k_x^2 f_a. \tag{4.15}$$

Here, $\stackrel{+}{=}$ denotes that the term is added on top of the usual time evolution of the distribution function in a (linear) gyrokinetic simulation. The full set of equations solved can be found in Ref. [65]. In the last step of the equation above the spectral representation of f is introduced, i.e. $\partial f / \partial x = \mathrm{i} k_x f$. Note that the diffusion term is evaluated for f_a, which is the part of the distribution function which is anti-symmetric in the parallel velocity, i.e. $f_a = 1/2(f(v_\parallel) - f(-v_\parallel))$. The even parallel velocity moments of the added term vanish,

and the radial density or temperature profiles are not affected. The added term, however, does lead to a diffusion of toroidal angular momentum.

Fig. 4.1 shows the time evolution of the electrostatic potential for the Rosenbluth-Hinton test, with parameters: safety factor $q = 1.3$, inverse aspect ratio $\epsilon = 0.05$, magnetic shear $\hat{s} = 0.1$, and radial wave vector $k_x = 8.4 \cdot 10^{-2}$. The adiabatic electron approximation is used and the grid sizes are $N_s = 264$ points along the field line, $N_{v_\parallel} = 256$ parallel velocity grid points, and $N_\mu = 16$ magnetic moment grid points. The top graph shows the potential (blue) as well as the residual potential (red), with the latter obtained through the method described in Ref. [21] that filters out the geo acoustic mode. The bottom graph shows the residual potential for different values of the diffusion coefficient D. A clear damping of the zonal potential, with the damping rate increasing with the diffusion coefficient can be observed. Assuming an

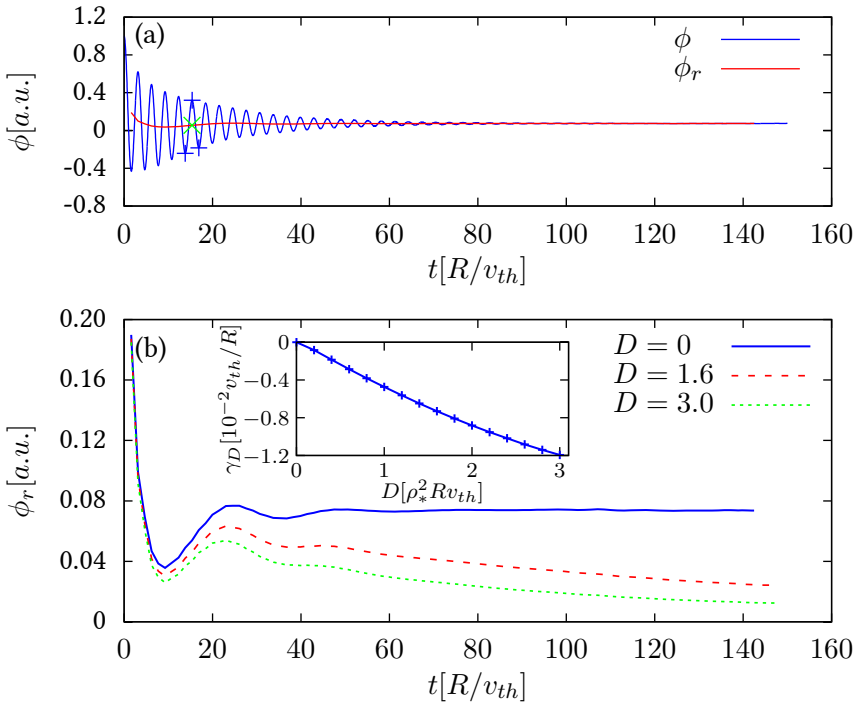

Figure 4.1. (a) The time evolution for the electrostatic potential ϕ and the residual potential ϕ_r without momentum diffusion ($D = 0$). The residual potential is obtained by averaging three neighbouring extrema, e.g. the green point is calculated from the three blue points.
(b) The time evolution of the residual electrostatic potential ϕ_r for different values of the diffusion constant D. Without diffusion (solid blue line) the zonal flow is undamped and has a non-zero steady final state. In simulations with momentum diffusion (dashed and dot-dashed lines) the zonal flow is dampened over time. The inlay shows the decay rate γ_D of the residual potential as a function off the diffusion coefficient D. The decay of the residual potential to zero cannot be shown as the simulation time is limited by the non-physical recurrence of the GAM-oscillation.

exponential decay $\phi_r = \phi_{r0}\exp(\gamma_D t)$, the zonal flow damping rate γ_D can be obtained from the data through a fit, and is shown in the inlay in Fig. 4.1b as a function of D. Using $\chi_\phi \approx 1$ in Eq. (4.9) yields $\gamma_D \approx -k_x^2 = -7\cdot 10^{-3}$ which is slightly larger but in good agreement with the decay rate $\gamma_D = -5\cdot 10^{-3}$ obtained in the simulation with $D = 1$. It is noted that the obtained damping rate is one order of magnitude larger than collisional damping for realistic ion collision frequencies ν_{ii} (Ref. [21] finds a damping rate of a few 10^{-4} for $\nu_{ii} \approx 10^{-3}$). While the damping rate due to angular momentum transport depends critically on the wavelength of the zonal flow, it is expected to be relevant for zonal potential wavelengths up to $k_x = 10^{-2}$.

4.3. Nonlinear simulations

In this section a nonlinear numerical experiment is presented that aims at investigating the role of the zonal flow damping through angular momentum transport. The normalised radial fluxes of density, parallel momentum and heat for the electrostatic case are given by

$$\Gamma_i = \left\{ \int d^3v \, (\mathbf{v}_E \cdot \nabla\psi)\alpha_i f \right\}, \tag{4.16}$$

where $\mathbf{v}_E = (\mathbf{B}\times\nabla\phi)/B^2$ is the E×B-velocity, ψ the normalised radial coordinate and $\alpha_i = \{1, mRB_t/Bv_\parallel, v^2\}$ are the respective parallel velocity moments. Writing the distribution function, as the sum of the symmetric and anti-symmetric part in the parallel velocity $f = f_s + f_a$, it is clear from the equation above that only the symmetric part $f_s = 1/2(f(v_\parallel) + f(-v_\parallel))$ contributes to the transport of particles and energy, while only the anti-symmetric part $f_a = 1/2(f(v_\parallel) - f(-v_\parallel))$ contributes to the transport of parallel momentum. By changing the E×B nonlinearity in the gyrokinetic equation to act on the symmetric part of the distribution function only

$$\mathbf{v}_E \cdot \nabla f \longrightarrow \mathbf{v}_E \cdot \nabla f_s, \tag{4.17}$$

transport of the odd moments of the perturbed distribution function is suppressed, thereby eliminating the turbulent parallel momentum transport. It is assumed here that the density and temperature perturbations, which are still transported, dominate the dynamics of the ITG, and that the nonlinear turbulent state is not strongly affected by the artificial modification made above.

Fig. 4.2 shows the heat conduction coefficient in gyro-Bohm units for nonlinear simulations with suppressed and regular momentum transport. The parameters are close to the cyclone base case: safety factor $q = 1.4$, inverse aspect ratio $\epsilon = 0.19$, magnetic shear $\hat{s} = 0.78$, and density gradient $R/L_n = 2.2$. The simulations use s–α geometry and adiabatic electrons. The temperature gradient length has been chosen to be larger than the finite heat flux threshold ($R/L_{Tc} = 7.3$ see Ref. [19]). Simulations are performed with 83 radial and 21 toroidal modes, with a maximum $k_\theta\rho = 1.4$, and the grid sizes are: $N_s = 16$ along the field line and $N_{v_\parallel} = 64$, $N_\mu = 9$.

It is shown in Fig. 4.2 that the removal of the parallel momentum transport can lead to reduced heat transport or even complete suppression of turbulent transport for weak turbulence

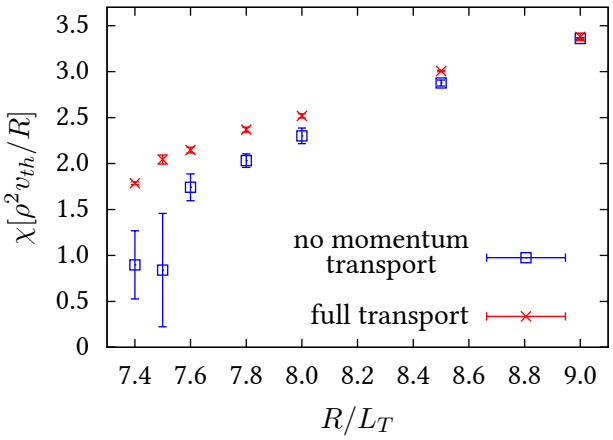

Figure 4.2. Gyro-Bohm heat diffusivity χ with error bars as function of temperature gradient $R/L_T = -R\partial \ln T/\partial r$. The blue squares are simulations where the momentum transport is artificially suppressed, which significantly reduces the turbulent heat flux compared to regular runs (red crosses). This effect is only relevant for weak turbulence with temperature gradients slightly above the nonlinear stability threshold $R/L_{Tc} = 7.3$.

directly above R/L_{Tc}, in agreement with the physical picture that the removal of the momentum transport allows for stronger zonal flow growth and, therefore, stronger suppression of turbulence. A direct comparison of zonal flow amplitudes does not necessarily show higher zonal flow amplitudes, since the turbulent drive of zonal modes is modified as well by a change in turbulent intensity. It is noted that the transition between zero heat flux at $R/L_T = 7.3$ and finite heat flux above the threshold goes more smoothly in the case in which momentum transport is suppressed. The proposed mechanism for zonal flow damping can explain the step in the heat flux that occurs at the finite heat flux threshold (see Refs. [19, 43]), since the mechanism predicts a critical turbulence intensity (I_t see Eq. 4.11) above which the damping dominates over the growth.

Fig. 4.3 depicts the time evolution of the heat flux for $R/L_T = 7.4$ and shows that the suppression of turbulence is connected with the formation of areas with strong zonal flow shearing ($\omega_{E\times B} = \partial v_E/\partial r$). These structures in the E×B shear are known as staircases [41]. The long wavelength structures in the zonal flow observed in Fig. 4.3b become more clearly visible when averaging over the corresponding time windows. The staircase structures are stable for several hundreds of transit times, allowing for the residual state to form. Staircases can completely suppress turbulence when they are fully developed [19], in which case the E×B shear equals the growth rate of the most unstable mode over (almost) the entire radial domain. Although not fully developed staircases have a similar E×B shear rate over a large part of the radial domain, the shear rate goes more gradually through zero and, consequently there is a sufficiently large radial region where turbulence can develop. Transport through the stable regions with $\gamma \approx \omega_{E\times B}$ then occurs through avalanches. Fig. 4.4 shows the radial profile of the E×B shear for the case with and without parallel momentum transport. It can be seen that both develop staircase structures. The case without momentum transport, and therefore stronger zonal flow

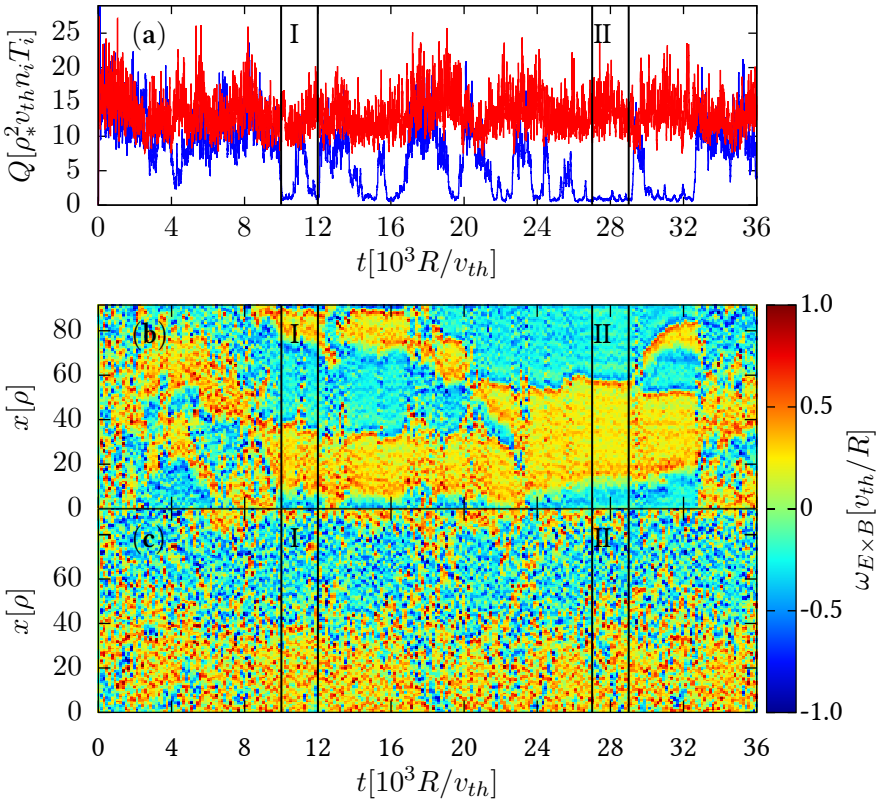

Figure 4.3. (a) Heat flux Q over time for a weakly turbulent ($R/L_T = 7.4$) nonlinear simulations with suppressed momentum transport (blue) and full transport (red). The zonal flow shear rate $\omega_{E\times B}$ for the simulation without momentum transport (b) forms long wavelength structures and suppresses the turbulence compared to the one with full transport (c). Note the highlighted areas I and II where the heat flux is significantly reduced and the staircase structure of the zonal flow is visible in b.

growth, allows the formation of a fully developed staircase, whereas the case with momentum transport does not.

Although the nonlinear experiment presented in this section suggests the parallel momentum transport is a mechanism that must be considered in staircase formation, it does not appear to have any impact on shorter wavelength zonal flows. For larger temperature gradients (above $R/L_T = 8$), no visible staircase structure appears in the E×B shearing rate, and the heat transport with or without parallel momentum transport is observed to be identical. This observation is striking since it is expected from the derivation in the Section II that the zonal flow damping rate scales inversely proportional to the square of the zonal flow wavelength. The reason why only long wavelengths are affected is at present not entirely clear. It is possible that short wavelength zonal flows have a temporal behaviour that is too fast to properly develop the residual state. In this case no significant parallel flows develop and the momentum transport does not provide a mechanism for zonal flow damping. It is also possible that the residual zonal

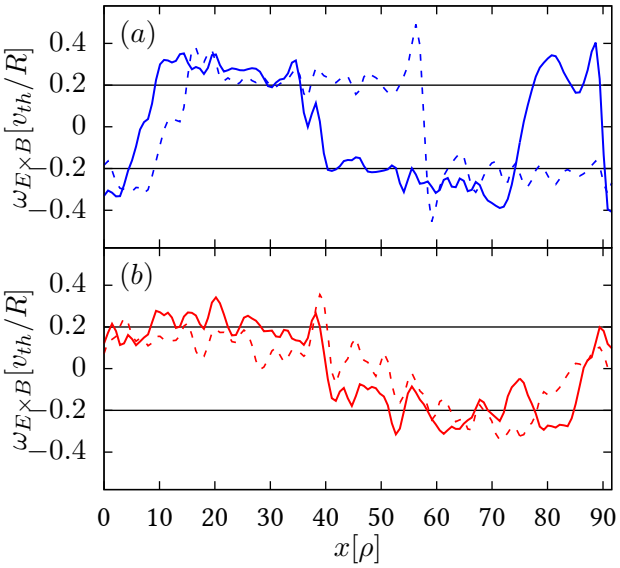

Figure 4.4. Time average of the shear rate of the highlighted areas I: $t \in [10000, 12000]$ (solid line) and II: $t \in [27000, 29000]$ (dashed line) in Fig. 4.3 for suppressed momentum transport (a) and full transport (b). Suppressing the momentum transport allows the development of a fully developed staircase, which is not observed in the case with momentum transport.

flow plays no or a very limited role in the saturation of gyrokinetic turbulence. Although the residual flow state has been proposed as an explanation for the difference between gyrofluid and gyrokinetic turbulence, a clear proof that this is the case appears to be lacking. Indeed, results presented in Ref. [99] suggest that scenarios exist in which the residual does not provide the dominant saturation mechanism. If the residual flow does not affect turbulence saturation, its damping will have little effect on the turbulent heat flux. These interesting research questions are left for future work.

4.4. Conclusions

The radial transport of parallel momentum provides a damping mechanism for the zonal flow, which is relevant for staircase formation in weakly turbulent simulations. Removing the zonal flow damping mechanism connected with the parallel momentum transport allows fully developed staircases to form at higher gradient lengths, and makes the transition in the heat flux as a function of the gradient length smoother. The damping mechanism can therefore explain the jump in the heat flux at the finite heat flux threshold. However, the mechanism discussed in this chapter counter-intuitively does not appear to affect shorter wavelength zonal flows. The results therefore give rise to questions about the relevance of the residual potential in turbulence saturation.

5. Interplay of an external torque and E×B structure formation

Rotation in tokamak plasmas is generally considered to be beneficial for confinement, as toroidal flow gradients can stabilise plasma turbulence by means of flow shearing[37, 39, 40, 91]. Furthermore, the resistive wall mode can be stabilised by sufficiently large rotation [100, 101]. Plasma rotation can occur intrinsically, without any external momentum source, or be driven by an external torque, caused, for example, by neutral beam injection. Intrinsic rotation, a phenomenon observed in multiple tokamak experiments [90], is particularly important in reactor plasmas, where the external torque will be comparatively small. Because of its promising effect in regulating the turbulence and, therefore, particle and energy confinement, the physics of the generation and transport of rotation has received considerable attention in the literature [85, 92]. However, in connection with the effects due to rotation it should be noted that a fusion experiment or reactor operates close to the nonlinear threshold of turbulence generation, where substantial shear flows are driven by the turbulence itself. It is well known that zonal flows lead to a nonlinear upshift of the temperature gradient threshold of turbulence generation, known as the Dimits shift [18] and recent investigations [19, 43] have shown that this upshift is further enhanced through the formation of meso-scale structures in the E×B shear, known as staircases [24, 41, 42]. Several studies [21–23, 102] have shown these structures to be robust features of plasma turbulence that are not suppressed by collisions or tertiary instabilities.

The staircase structures are stable for several hundred transit times and can completely suppress turbulence when they are fully developed, in which case the E×B shear equals or is greater than the growth rate of the most unstable mode over (almost) the entire radial domain. The radial average of the shear without external momentum is zero and the transition between high positive and negative shear is very steep, leaving no space for turbulence to develop. Although not fully developed staircases have a similar E×B shear rate over a large part of the radial domain, the shear rate passes through zero more gradually, and, consequently, there is a sufficiently large radial region where turbulence can develop. Energy is then transported through the stable regions by heat flux avalanches.

The above-mentioned studies of staircases are conducted without external torque and also exclude the mechanisms that lead to intrinsic momentum generation through symmetry breaking [84, 86]. The synergy between externally imposed torque and E×B structure formation is an unexplored area. Adding an external torque to the system will modify the shear flows and the radial average of the shear rate can be expected to be nonzero. However, how does this externally forced shear interact with the existing structures? Does the external shear simply add to the shear connected with the staircase, or is the staircase structure modified, perhaps even

destroyed? The answer to this question is highly relevant for the influence of plasma rotation on confinement: If an external torque destroys the staircase structure, it might adversely affect plasma confinement, whereas an unmodified staircase structure implies that the torque does not influence the confinement.

This chapter aims at clarifying the synergy of staircases and externally forced shear using gyrokinetic simulations. The shear profile and heat transport under the influence of a momentum source is studied slightly above the nonlinear stability threshold.

In Section 5.1 the simulation setup is discussed in detail and numerical results are presented. Finally, conclusions are formulated in Section 5.2.

5.1. Simulations

To assess the interplay between an external torque and staircase structure formation, nonlinear gyro-kinetic flux driven simulations using the GKW code [65] are performed, where the turbulence is driven by prescribing a heat source rather than a fixed background temperature gradient. Flux driven simulations are required to accurately study the turbulence close to the nonlinear turbulence stability threshold and the reader is referred to Ref. [43] for more details. Furthermore, flux driven simulations allow to prescribe the momentum input rather than the externally forced shearing rate. This is of the utmost importance since only this choice allows the shearing rate to develop into a self-consistent profile.

Following the setup of Ref. [43] (for a full overview of the model equations see also Ref. [65]), a Gaussian source and sink function are introduced at the edges of the computational domain, with a large source free region in the centre of the box. The source and sink will lead to an energy and momentum flux through the source free region, where the data is evaluated. The velocity dependence $G(v)$ of the source function is chosen such that it does not provide a particle source:

$$G(\mathbf{v}) = \Delta S \left(\frac{v^2}{v_{\text{th}}^2} - \frac{\int \mathrm{d}^3\mathbf{v}\ \frac{v^2}{v_{\text{th}}^2} F_M}{\int \mathrm{d}^3\mathbf{v}\ F_M} \right) F_M. \tag{5.1}$$

Here, ΔS is a parameter to control the source strength, v_{th} is the ion thermal velocity and F_M the Maxwellian background distribution. By shifting the midpoint of the Maxwellian in the parallel velocity domain by v_{shift}, the source is modified to generate both an energy as well as a parallel momentum input. The Maxwellian

$$F_M \propto \exp\left[-\frac{(v_\parallel - v_{\text{shift}})^2 + v_\perp^2}{v_{\text{th}}^2} \right], \tag{5.2}$$

where the velocities parallel and perpendicular to the magnetic field are denoted by $v_\parallel$ and $v_\perp$ respectively. For clarity it is noted that the shifted Maxwellian is only used in the source function which appears on the right-hand side of the gyrokinetic equation, while the remaining equation is unchanged.

The strength of the momentum source is specified by the ratio P_S/Q_S with the toroidal angular

momentum density

$$P_S = R \int \mathrm{d}^3\mathbf{v}\; m v_\parallel G(\mathbf{v}) \tag{5.3}$$

and the energy density

$$Q_S = \int \mathrm{d}^3\mathbf{v}\; \frac{1}{2} m v^2 G(\mathbf{v}) \tag{5.4}$$

generated by the source, where R is the major radius and m is the ion mass. The source can be considered as similar to using neutral beam injection in tokamak experiments, where the angle between the beam injection and the magnetic field line, in conjunction with the beam velocity, controls the ratio of applied torque to heating. In the following, for easier readability, the ratio P_S/Q_S is understood to be normalised by R/v_{th}.

The source strength $\Delta S = 10$ is chosen such that the simulation without a momentum source ($v_{\text{shift}} = 0$) is slightly above the nonlinear turbulence stability threshold (see Ref. [43]). Note that increasing $|v_{\text{shift}}|$ leads to an increased heating strength Q_S as well. Therefore, when increasing v_{shift}, $\Delta S = 10$ is reduced to ensure that all simulations are subject to the same level of heating, allowing for a direct comparison of turbulent transport. Furthermore, to ensure that the equilibrium state is a state in which the plasma rotates toroidally (rather than having a flow parallel to the magnetic field) collisions are used with an ion-ion collision frequency $\nu_{ii} = 10^{-2} v_{\text{th}}/R$. The collisions are modelled by a linearized Fokker-Planck pitch angle scattering collision operator that satisfies momentum conservation [65]. To ensure the fast relaxation of the particle distribution in velocity space, the collision frequency is set relatively high in comparison to the value of $6 \cdot 10^{-4} v_{\text{th}}/R$ expected in ITER. However, the effect of collisions is still weak enough to only slightly dampen the zonal flow and still allow for staircase formation [21].

All simulations use the adiabatic electron approximation and parameters similar to the Cyclone Base Case, with circular flux surfaces, safety factor $q = 1.4$, inverse aspect ratio $\epsilon = 0.19$, magnetic shear $\hat{s} = 0.78$, density gradient $R/L_n = 2.2$, and electron to ion temperature ratio $T_e/T_i = 1$. A background temperature gradient of $R/L_{T_0} = 3.0$ is used in addition to the heat source to reduce the equilibration time. Simulations are performed with 28 toroidal modes, with a maximum wavenumber $k_\theta \rho = 1.4$, while the other dimensions are treated with finite differences with the grid sizes being $N_{v_\parallel} = 32$ for the parallel velocity, $N_\mu = 8$ for the magnetic moment, $N_s = 24$ along the field line and $N_x = 240$ in the radial direction. The radial box size is 120 Larmor radii and the local flux tube model is used [64].

Fig. 5.1 shows the averaged E×B shear rate $\langle\langle \omega_{E\times B} \rangle\rangle$ for increasing momentum source strength. The shear rate is defined as the radial derivative of the E×B velocity $\omega_{E\times B} = \partial/\partial r\; v_{E\times B}$ and the double brackets $\langle\langle \cdots \rangle\rangle$ denote both a time as well as a spatial average over the source free region. It can be seen that the momentum source is working as intended, driving E×B shear in the simulation domain, with an average that depends linearly on the momentum source strength. The comparison with collisionless simulations shows that the collision frequency is not too high to deter the zonal flow from developing. All data shown in

the following is from simulations which take ion-ion collisions into account ($\nu_{ii} = 10^{-2} v_{\text{th}}/R$). The values of P_S/Q_S considered do indeed represent realistic values for forced plasma rotation, which can be verified by a simple magnitude estimation. Using $B_p/B \approx \epsilon/q$ and the force balance $E_r = B_p v_\varphi$, where E_r is the radial electric field, B_p the poloidal magnetic field and v_φ the toroidal velocity, it is possible to connect the shear rate with the ion Mach number M. The shear rate

$$\omega_{E\times B} \sim \frac{1}{a} v_{E\times B} \approx \frac{1}{a}\frac{E_r}{B} \approx \frac{v_{\text{th}}}{Rq}\frac{v_\varphi}{v_{\text{th}}} = \frac{v_{\text{th}}}{Rq} M, \tag{5.5}$$

where $\epsilon = a/R$ is the minor over the major radius. With the Mach number being $M \sim 0.1{-}0.3$ for most tokamaks [90], weak to moderate plasma rotation is well covered with P_S/Q_S up to 0.25 (see Fig. 5.1).

The externally forced shear can also be seen in Fig. 5.2 in the shear profile, along with it's effect on the radial meso-scale structures. Note that the time series and averages, are taken after very long equilibration times of about 10^4 transit times, which are required for the actual turbulence and shear profile to form in simulations close to the nonlinear stability threshold. Staircases can be observed for up to moderate values of external torque, as shown in the figure. They are stable over the entire time interval, and are only sporadically interrupted by avalanches that move through the system. Furthermore, they exhibit plateau areas with high shearing $|\omega_{E\times B}| > 0.2 v_{\text{th}}/R$ with a radial extend of several ten Larmor radii. From Fig. 5.2 the interplay between the external torque and the staircase structure can be observed: increasing external torque the positive shear areas are broadened at the expense of the negative ones, thus leading to the positive externally forced average shear. This behaviour can be observed until most of the simulation domain is covered by the high shear plateau areas. While the average

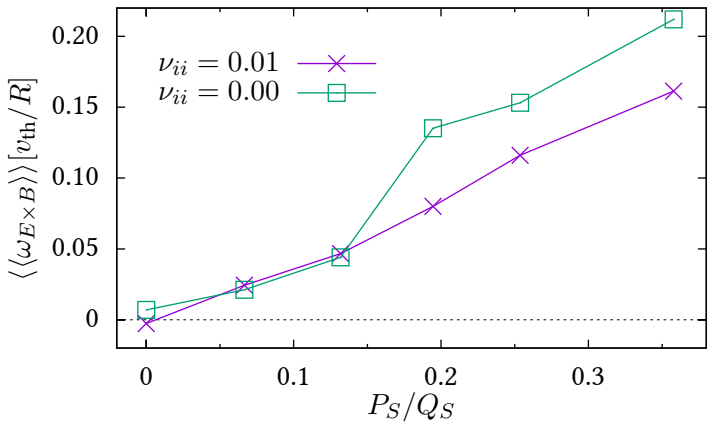

Figure 5.1. Averaged E×B shear rate $\langle\langle\omega_{E\times B}\rangle\rangle$ as a function of the momentum source strength P_S/Q_S. The shear rate for simulations with collisions $\nu_{ii} = 0.01$ (purple crosses) increases linearly with the external torque applied, which shows that the momentum source is indeed driving E×B shear as expected. For simulations without collisions $\nu_{ii} = 0.00$ (green squares) the behaviour is slightly erratic, which is likely due to the external momentum not being distributed evenly in velocity space.

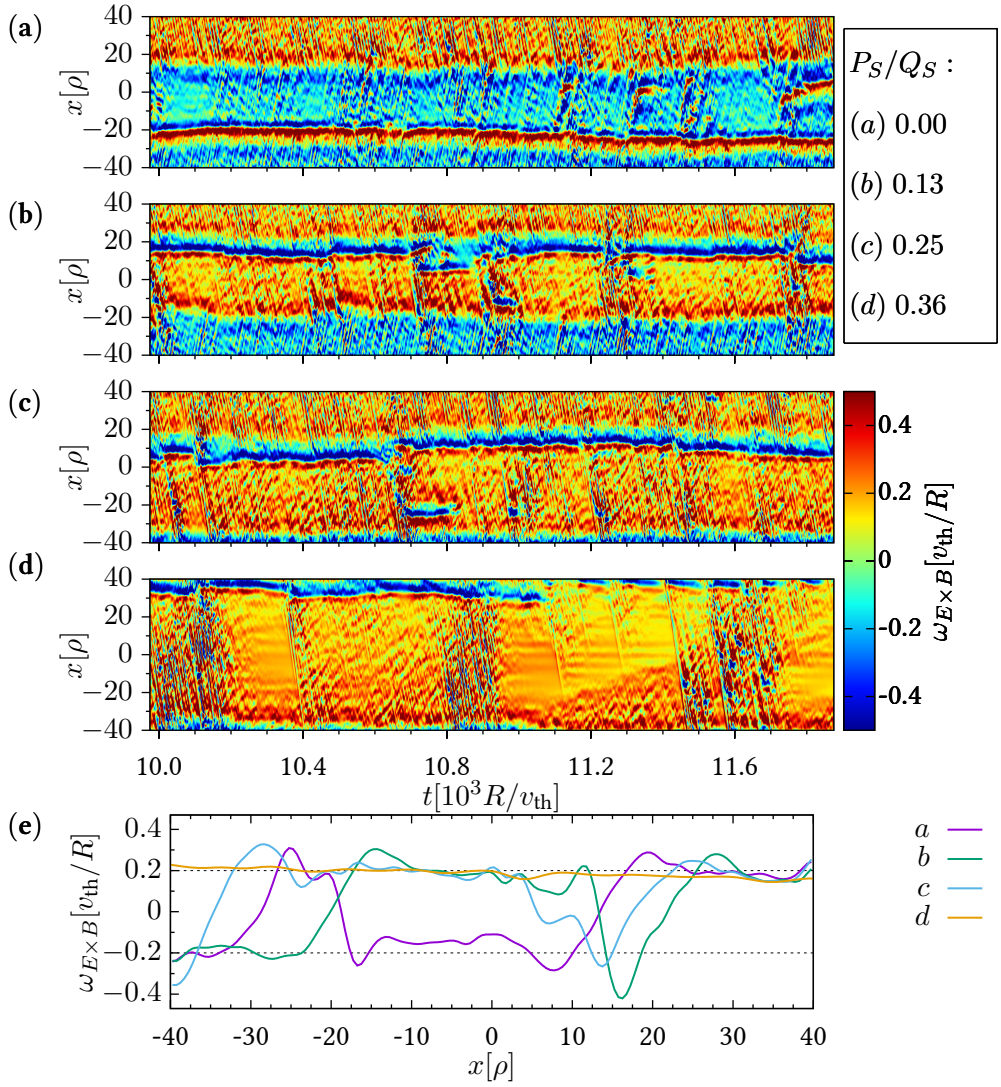

Figure 5.2. Radial structure of the E×B shear rate $\omega_{E\times B}$ over time and its time average for increasing values of the external torque. The large band like structures well visible in (a,b) are prime examples for so called staircase structures, which can effectively regulate turbulence. (a-c) Increasing the strength of the momentum source broadens the positive shear areas but preserves the qualitative structure, up to the point where the negative shear regions have nearly vanished. (d) Further increasing the torque breaks the structure and virtually the whole box exhibits high positive shear. (e) Despite the strongly modified shear, the time averaged shearing rate has similar plateau values for all cases.

shear increases with increasing external torque, the plateau values of the shear rate remain similar for all cases shown. The ability of staircases to suppress turbulence very effectively is due to two aspects of the shear profile: Firstly, large connected areas with an absolute shear rate comparable to or exceeding the ITG growth rate of $\gamma_{\mathrm{ITG}} \approx 0.2 v_{\mathrm{th}}/R$ are present. Secondly, the intermittent regions between positive and negative shear are very narrow. Transport is caused by avalanches generated in the region where the E×B shear passes through zero, which then propagate through the regions of high shear. This situation is similar for the first three structures shown in Fig. 5.2, regardless of the respective proportion of positive and negative shear areas. In consequence the ability to suppress turbulence is fairly similar in the examples shown even though the averaged shear rate is significantly modified. Only for the highest shown value $P_S/Q_S = 0.36$, the staircase structure is broken and the whole domain exhibits strong positive shear, except for a small region at the edge, which should lead to increased turbulence suppression compared to the cases with a weaker momentum source. This qualitative argument can be verified in Fig. 5.3, showing the radial heat flux profile Q and its average $\langle\langle Q \rangle\rangle$, which indicates the strength of the turbulent transport. The values are similar to, or exceed experimental relevant heat fluxes and the heat is mostly carried by avalanches, which build up in the low shear region and carry the energy into the suppressed high shear regions. This behaviour is similar for up to $P_S/Q_S = 0.25$, i.e. even a significant torque on the plasma does not improve confinement. Only very high values allow for improved turbulence suppression: Longer periods of several hundred transit times which exhibit no turbulent transport are occasionally interrupted by short bursts of avalanche dominated transport, which are quickly suppressed by the strong shearing rate.

5.2. Conclusions

Using nonlinear gyro-kinetic simulations it is shown, that for an external torque, comparable to that used in neutral beam heating experiments, the externally forced shear from rotation does not improve plasma confinement. The additional E×B shear does not simply yield an offset over the simulation domain but interacts with the meso-scale structures in the E×B shear, leaving the maximum shearing rate virtually unchanged. The ability of staircases to regulate turbulence very effectively is due to large connected areas where the absolute shear rate is equal or higher than the ITG growth rate $\gamma_{\mathrm{ITG}} \approx 0.2$ and the intermittent low regions between positive and negative shear being very narrow. A positive (negative) externally forced shear leads to a broadening of the corresponding region, but does not significantly change the plateau value or the narrow zero shear region. In consequence, the radial average is changed by the externally forced shear but the effect of the shear structures on the turbulent transport remains unaffected. Thus, a flux of radial momentum, which can be caused by neutral beam injection or intrinsic rotation does not aid in suppressing turbulent transport in this case, even though it modifies the average E×B shearing. The implication of this result is devastating. In contrast to the generally acknowledged beneficial impact of rotation on transport, this chapter shows that induced plasma rotation and, by extension, intrinsic rotation are irrelevant in the determination of experimentally relevant transport levels.

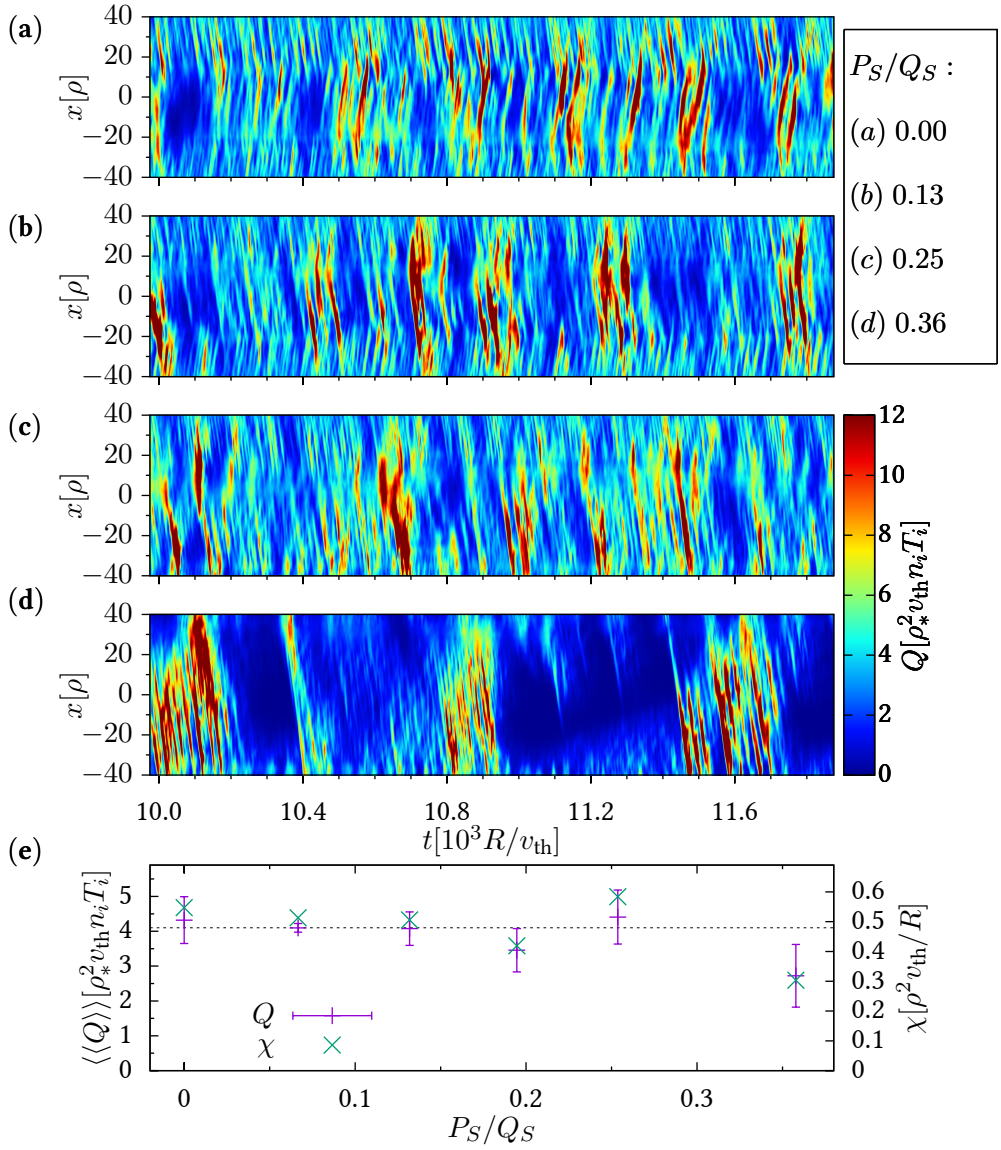

Figure 5.3. Radial structure of the radial heat flux Q in gyro-Bohm units over time and its average $\langle\langle Q\rangle\rangle$ for increasing values of the external torque. (a-c) Increasing the strength of the momentum source does not impact the turbulent transport, which is mainly carried by heat flux avalanches originating in the low shear regions. (d) For very strong external shear the turbulence exhibits periods of complete suppression over several 100 transit times, which are interrupted by short avalanche-like bursts that are eventually suppressed again. (e) The averaged radial heat flux $\langle\langle Q\rangle\rangle$ is, within the margin of error, nearly identical for a momentum source up to $P_S/Q_S = 0.25$, confirming the qualitative observations on the profile. The error bars of the heat flux are given by three part time averaging and the gyro-Bohm heat diffusivity $\chi = \langle\langle Q\rangle\rangle/\langle\langle R/L_T\rangle\rangle$ is shown for reference to showcase that all simulations are subject to a similar temperature gradient driving the turbulence.

6. Conclusions

Turbulent transport is a core problem when magnetically confining a fusion plasma. The theoretical description has advanced significantly over the last few decades as the gyrokinetic models of turbulent transport in tokamak plasmas, employing the increased computational power, have become increasingly sophisticated, allowing to consider more and more physical effects. This thesis continues the efforts of understanding and predicting turbulence in a tokamak by studying the cross-coupling of the background described by neoclassical theory and the gyrokinetic turbulence.

In Chapter 2, it was shown that the parallel velocity nonlinearity in the gyrokinetic equation couples with the neoclassical background. The term can cause a parallel drive of momentum and heat, provided the symmetry along the magnetic field is broken, for example through a background rotation. It was shown that this modification to the neoclassical equilibrium drives a substantial current, which is of great interest for tokamak operation as it can potentially increase the pulse time limited by the necessity of inductive current drive. The current driven is mostly linear in the turbulent heat flux and for the cyclone base case comparable in magnitude to the bootstrap current. When matching realistic heat flux values expected in an ITER scenario, the current drive still makes up for a few additional percent of total current. As an upper limit for scenarios with strong rotation or strong rotation gradient up to ten percent increase in total plasma current can be achieved. However, the model used only aims to identify the effect and establish the order of magnitude. Corrections can be expected from other symmetry breaking mechanisms like the stationary $E \times B$ flow associated with the rotation gradient, or the coupling with the neoclassical background. Furthermore, there are other current driving mechanisms from turbulence related to the electromagnetic response and profile effects [79]. Further research is required for a quantitative prediction, including all the mechanisms discussed above to assert if they partly cancel each other or possibly further increase the current driven.

Intrinsic rotation has been a topic of great interest in tokamak research, as plasma rotation is considered beneficial for confinement (even though the results of Chapter 5 question this assessment). Intrinsic rotation is always connected to symmetry breaking and in Chapter 3, a large scale parameter study of the intrinsic rotation caused by neoclassical modifications to the Maxwellian background in turbulent simulations was performed. It was shown that the toroidal angular momentum flux is mostly linear in the first order neoclassical flow and its gradient. However, there is a significant amount of scatter especially for different aspect ratios and values of the magnetic shear suggesting that a scaling law employing only the parameters directly involved in the symmetry breaking, namely the parallel flow and its gradient, is insufficient to produce accurate results. Comparing gyrokinetic simulations using neoclassical modifications and simulations with a Maxwellian background but subject to background rota-

tion (and rotation gradient) a model was developed to predict the equilibrium rotation gradient driven by the neoclassical modifications to the background. The results show that the toroidal angular momentum flux is roughly linear in the parallel flow velocity obtained in neoclassical theory. This suggests that the parallel flow in the neoclassical equilibrium provides the most important symmetry breaking mechanism required for momentum transport, and allows a simple scaling law for the flux in terms of the flow.

Zonal flows have a regulating effect on turbulence and play a critical role for the nonlinear stability threshold of turbulence. In Chapter 4 it was shown that the radial transport of parallel momentum provides a damping mechanism for the zonal flow. The damping mechanism was confirmed by "Rosenbluth-Hinton" tests with a model radial momentum diffusion. The decay rate of the residual potential was found to be proportional to the model diffusion coefficient and in good agreement with the analytic result. In nonlinear simulations the damping mechanism was shown to be relevant for turbulence slightly above the stability threshold, where the meso-scale structures called staircases in the zonal flow play a critical role. Removing the zonal flow damping mechanism connected with the parallel momentum transport allows fully developed staircases to form at higher temperature gradient lengths. Thus, turbulence is periodically suppressed above the stability threshold, called finite-heat-flux threshold, leading to a smoother transition in the heat flux as a function of the gradient length from the suppressed state to the weakly turbulent state above the threshold. The damping mechanism can therefore explain the jump in the heat flux at the finite heat flux threshold. However, while the mechanism scales with the wave number it counter-intuitively does not appear to affect shorter wavelength zonal flows. Furthermore, there is no effect on the heat flux level for strong turbulence significantly above the stability threshold. The results therefore give rise to questions about the relevance of the residual potential in turbulence saturation.

In Chapter 5, using nonlinear gyrokinetic simulations it was shown, that for an external torque, comparable to that used in neutral beam heating experiments, the externally forced shear from rotation does not improve plasma confinement. The additional E×B shear does not simply yield an offset over the simulation domain but interacts with the meso-scale structures in the E×B shear, leaving the maximum shearing rate virtually unchanged. The ability of staircases to regulate turbulence very effectively is due to large connected areas where the absolute shear rate is equal or higher than the ITG growth rate $\gamma_{\mathrm{ITG}} \approx 0.2$ and the intermittent low regions between positive and negative shear being very narrow. A positive (negative) externally forced shear leads to a broadening of the corresponding region, but does not significantly change the plateau value or the narrow zero shear region. In consequence, the radial average is changed by the externally forced shear but the effect of the shear structures on the turbulent transport remains unaffected. Thus, a flux of radial momentum, which can be caused by neutral beam injection or intrinsic rotation does not aid in suppressing turbulent transport in this case, even though it modifies the average E×B shearing. The implication of this result is devastating. In contrast to the generally acknowledged beneficial impact of rotation on transport, it was shown that induced plasma rotation and, by extension, intrinsic rotation are irrelevant in the determination of experimentally relevant transport levels.

Appendix

A. Derivation of the parallel force balance equation from the gyrokinetic Fokker-Planck equation

The gyrokinetic description of the steady state distribution (Eq. (2.14) in section 2.1 is equivalent to the kinetic equation used in Refs. [14, 15] to derive the parallel force balance equations. Obviously the gyrokinetic equation contains higher order drift effects, which are not treated in standard neoclassical theory, but these terms can be shown to be small. It is stressed that the goal of this work is to study only the effect of the turbulent velocity nonlinearity on the leading order of the neoclassical equilibrium and not to provide a more accurate neoclassical solution. The derivation of the balance equations is demonstrated deriving the first order of balance equation for a single species,

$$\{\mathbf{B}\cdot\nabla\cdot\mathbf{P}_1\} = \{\mathbf{F}_1\cdot\mathbf{B}\} + S_{\parallel,1}, \tag{A.1}$$

with the viscosity tensor $\mathbf{P}_1 = (p_\parallel - p_\perp)(\mathbf{bb} - \frac{1}{3}\mathbf{I})$, the friction force $\mathbf{F}_1 = \int \mathrm{d}^3v\; mC(\overline{f})$ and source terms $S_{\parallel,1} = S_{E\parallel,1} + S_{\text{vnl}\parallel,1} = Zen\{\mathbf{E}\cdot\mathbf{B}\} + S_{\text{vnl}\parallel,1}$ where $S_{\text{vnl}\parallel,1}$ is given by Eq. (2.21). The pressure $p = 1/3\,p_\parallel + 2/3\,p_\perp$ is expressed by a parallel $p_\parallel = \int \mathrm{d}^3v\; m(v_\parallel - u_\parallel)^2\overline{f}$ and a perpendicular part $p_\perp = \int \mathrm{d}^3v\; m|\mathbf{v}_\perp - \mathbf{u}_\perp|^2/2\,\overline{f}$.

The steady state distribution $\overline{f} = f_0 + f_1$ is split in a Maxwellian background f_0 and the neoclassical modification f_1, which is assumed to be one order smaller. Furthermore terms in the drift velocity $\mathbf{v}_D$ are assumed to be one order smaller than the parallel velocity $v_\parallel\mathbf{b}$. Thus, the contributions in $\mathcal{O}(\mathbf{v}_D f_1)$ are neglected for the large scale equilibrium. Using this ordering and the steady state ($\partial\overline{f}/\partial t = 0$) in Eq. (2.14) yields

$$\begin{aligned}\left[v_\parallel\mathbf{b} + \overline{\mathbf{v}}_E\right]\cdot\nabla\overline{f} + \mathbf{v}_D\cdot\nabla f_0 - \frac{\mu}{m}(\mathbf{b}\cdot\nabla B)\frac{\partial\overline{f}}{\partial v_\parallel} + \left[\frac{v_\parallel\mathbf{b}\times\nabla B}{B^2} + \frac{2}{B}\mathbf{\Omega}_\perp\right]\cdot\mathbf{E}\frac{\partial f_0}{\partial v_\parallel}\\ = C(\overline{f}) - \frac{Ze}{m}\mathbf{b}\cdot\mathbf{E}\frac{\partial\overline{f}}{\partial v_\parallel} + \frac{\partial}{\partial v_\parallel}\left[\left\langle\left[\frac{Ze}{m}\mathbf{b} + \frac{v_\parallel\mathbf{b}\times\nabla B}{B^2} + \frac{2}{B}\mathbf{\Omega}_\perp\right]\cdot\nabla\langle\widetilde{\phi}\rangle\widetilde{f}\right\rangle_t\right]\end{aligned} \tag{A.2}$$

The neoclassical electrostatic potential $\nabla\overline{\phi}$, being a perturbed quantity, is ignored like in Ref. [14], and only the external field $\mathbf{E}$ is considered.

The first velocity moment $\{\mathbf{B}\cdot\int \mathrm{d}^3v\ \mathbf{v}\cdots\}$ of the right hand side of Eq. A.2 is

$$\begin{aligned}&\{\mathbf{B}\cdot\mathbf{F}_1\} - Ze\left\{\int \mathrm{d}^3v\ \mathbf{B}\cdot\mathbf{E}v_\parallel\frac{\partial\overline{f}}{\partial v_\parallel}\right\} + S_{\text{VNL}\parallel,1} = \{\mathbf{B}\cdot\mathbf{F}_1\} + Ze\left\{\mathbf{B}\cdot\mathbf{E}\int \mathrm{d}^3v\ \overline{f}\right\} + S_{\text{VNL}\parallel,1}\\ &= \{\mathbf{B}\cdot\mathbf{F}_1\} + Zen\{\mathbf{E}\cdot\mathbf{B}\} + S_{\text{VNL}\parallel,1} = \{\mathbf{F}_1\cdot\mathbf{B}\} + S_{\parallel,1}\end{aligned} \tag{A.3}$$

and thus equal to the right hand side of Eq. A.1.

The velocity moment of the left hand side is more complicated and will be done in multiple steps. First the terms containing the Maxwellian background are removed using that f_0 is even in $v_\parallel$

$$f_0(v_\parallel,\mu) = f_0(-v_\parallel,\mu). \tag{A.4}$$

Note that $\mathbf{v}_D$ with the exception of the Coriolis term is even in $v_\parallel$ as well and f_0 spatially depends only on the radial coordinate ψ. Thus,

$$\begin{aligned}\left\{\int \mathrm{d}^3v\ mBv_\parallel(\mathbf{v}_D\cdot\nabla)f_0\right\} &= \left\{\int \mathrm{d}^3v\ \frac{2m^2v_\parallel^2}{Ze}(\boldsymbol{\Omega}_\perp\cdot\nabla)f_0\right\}\\ &= \int \mathrm{d}^3v\ \frac{2m^2v_\parallel^2}{Ze}\frac{\partial f_0}{\partial\psi}\{\boldsymbol{\Omega}_\perp\cdot\nabla\psi\} = 0,\end{aligned} \tag{A.5}$$

because $\boldsymbol{\Omega}_\perp\cdot\nabla\psi = \boldsymbol{\Omega}\cdot\nabla\psi$ is up-down symmetric it follows that the flux surface average of this quantity is zero. The two following terms are not exactly zero but can be shown to hold only a much smaller contribution. It is used that the electric field is only in the toroidal direction and that $B_p/B = \epsilon/q$, which is true up to the first order in ϵ. First

$$\begin{aligned}\left\{\int \mathrm{d}^3v\ mBv_\parallel\overline{\mathbf{v}}_E\cdot\nabla\overline{f}\right\} = \left\{\int \mathrm{d}^3v\ mv_\parallel(\mathbf{E}\times\mathbf{B})\cdot\nabla\overline{f}\right\} &= \left\{(\mathbf{E}\times\mathbf{B})\cdot\int \mathrm{d}^3v\ mv_\parallel\nabla f_1\right\}\\ &\approx \frac{\epsilon}{q}\left\{EB\int \mathrm{d}^3v\ mv_\parallel\nabla_\psi f_1\right\},\end{aligned} \tag{A.6}$$

where ∇_ψ is the radial derivative. The term is in ϵ and only the small up-down asymmetric part of f_1 contributes to the flux surface average, making it negligible. The last term on the left hand side disappears as well

$$\begin{aligned}&\left\{\int \mathrm{d}^3v\ \left[\frac{mv_\parallel^2}{B}\mathbf{b}\times\nabla B + 2mv_\parallel\boldsymbol{\Omega}_\perp\right]\cdot\mathbf{E}\frac{\partial f_0}{\partial v_\parallel}\right\}\\ &= -\left\{\int \mathrm{d}^3v\ \left[\frac{2mv_\parallel\mathbf{b}\times\nabla B}{B} + 2m\boldsymbol{\Omega}_\perp\right]\mathbf{E}f_0\right\}\\ &= -\left\{\int \mathrm{d}^3v\ 2m\boldsymbol{\Omega}_\perp\cdot\mathbf{E}f_0\right\} = -\{2mn_0\boldsymbol{\Omega}_\perp\cdot\mathbf{E}\} = \left\{\frac{2mn_0}{B}(\boldsymbol{\Omega}\cdot\mathbf{B})\mathbf{b}\cdot\mathbf{E}\right\}\\ &= -\left\{\frac{2mn_0}{B}(\boldsymbol{\Omega}\cdot\mathbf{B}_p)\mathbf{b}\cdot\mathbf{E}\right\} \approx 2mn_0\frac{\epsilon}{q}\Omega\{\pm\cos\theta(\mathbf{b}\cdot\mathbf{E})\} \approx 0.\end{aligned} \tag{A.7}$$

Here θ is the poloidal angle and $B_p/B \approx \epsilon/q$ is used. The sign depends on the direction of current and rotation.
Now the left hand side has two remaining terms connected with the parallel and perpendicular pressure:

$$
\begin{aligned}
&\left\{ \int \mathrm{d}^3v\ mBv_\parallel^2 \mathbf{b}\cdot\nabla\overline{f} - \int \mathrm{d}^3v\ \mu B v_\parallel (\mathbf{b}\cdot\nabla B)\frac{\partial \overline{f}}{\partial v_\parallel} \right\} \\
&= \left\{ \iint \mathrm{d}v_\parallel \mathrm{d}(2\pi\mu)\ mv_\parallel^2 \frac{B}{m}\mathbf{B}\cdot\nabla\overline{f} + \int \mathrm{d}^3v\ \mu B(\mathbf{b}\cdot\nabla B)\overline{f} \right\} \\
&= \left\{ \iint \mathrm{d}v_\parallel \mathrm{d}(2\pi\mu)\ mv_\parallel^2 \left[(\mathbf{B}\cdot\nabla)\left(\frac{B}{m}\overline{f}\right) - (\mathbf{b}\cdot\nabla B)\frac{B}{m}\overline{f} \right] + \int \mathrm{d}^3v\ \frac{mv_\perp^2}{2}(\mathbf{b}\cdot\nabla B)\overline{f} \right\} \\
&= \left\{ (\mathbf{B}\cdot\nabla)\left[\iint \mathrm{d}v_\parallel \mathrm{d}(2\pi\mu)\ \frac{B}{m} mv_\parallel^2 \overline{f} \right] - (\mathbf{b}\cdot\nabla B)\left[\iint \mathrm{d}v_\parallel \mathrm{d}(2\pi\mu)\ \frac{B}{m} mv_\parallel^2 \overline{f} \right] + (\mathbf{b}\cdot\nabla B)\int \mathrm{d}^3v\ \frac{mv_\perp^2}{2}\overline{f} \right\} \\
&= \left\{ (\mathbf{B}\cdot\nabla)\left[\int \mathrm{d}^3v\ mv_\parallel^2 \overline{f} \right] - (\mathbf{b}\cdot\nabla B)\left[\int \mathrm{d}^3v\ mv_\parallel^2 \overline{f} \right] + (\mathbf{b}\cdot\nabla B)p_\perp + (\mathbf{b}\cdot\nabla B)nmu_\perp^2 \right\} \\
&= \left\{ (\mathbf{B}\cdot\nabla)p_\parallel - (\mathbf{b}\cdot\nabla B)(p_\parallel - p_\perp) \right\} + \left\{ (\mathbf{B}\cdot\nabla)nmu_\parallel^2 - (\mathbf{b}\cdot\nabla B)nm(u_\parallel^2 - \frac{1}{2}u_\perp^2) \right\}. \quad \text{(A.8)}
\end{aligned}
$$

The second term containing the fluid velocities is of second higher order in ρ_* and can be neglected.
Adding

$$
0 = \mathbf{B}\cdot\nabla p - \mathbf{B}\cdot\nabla p = \mathbf{B}\cdot\nabla p - (\mathbf{B}\cdot\nabla)\left[\frac{1}{3}p_\parallel + \frac{2}{3}p_\perp \right] \quad \text{(A.9)}
$$

to the left hand side equation we get

$$
\left\{ (\mathbf{B}\cdot\nabla)p + \frac{2}{3}(\mathbf{B}\cdot\nabla)(p_\parallel - p_\perp) - \mathbf{b}\cdot\nabla B(p_\parallel - p_\perp) \right\}. \quad \text{(A.10)}
$$

Using $\{\mathbf{B}\cdot\nabla p\} = 0$ we can write the parallel force balance equation

$$
\left\{ \frac{2}{3}(\mathbf{B}\cdot\nabla)(p_\parallel - p_\perp) - (\mathbf{b}\cdot\nabla B)(p_\parallel - p_\perp) \right\} = \{\mathbf{F}_1\cdot\mathbf{B}\} + S_{\parallel,1}. \quad \text{(A.11)}
$$

Rewriting the viscosity $\langle \mathbf{B}\cdot\nabla\cdot\mathbf{P}_1^a \rangle$ using $\mathbf{P}_1^a = (p_\parallel - p_\perp)(\mathbf{bb} - \frac{1}{3}\mathbf{I})$ and $\tilde{p} \equiv p_\parallel - p_\perp$ yields

$$
\begin{aligned}
\langle \mathbf{B}\cdot\nabla\cdot\mathbf{P}_1^a \rangle &= \left\{ \mathbf{B}\cdot\left[\nabla\tilde{p}\cdot(\mathbf{bb} - \frac{1}{3}\mathbf{I}) + \tilde{p}\nabla\cdot(\mathbf{bb} - \frac{1}{3}\mathbf{I}) \right] \right\} \\
&= \left\{ \mathbf{B}\cdot\left[(\nabla\tilde{p}\cdot\mathbf{b})\mathbf{b} - \frac{1}{3}\nabla\tilde{p} + \tilde{p}\nabla\cdot(\mathbf{bb}) \right] \right\} = \left\{ B(\mathbf{b}\cdot\nabla\tilde{p}) - \frac{1}{3}\mathbf{B}\cdot\nabla\tilde{p} + \tilde{p}B_j\frac{\partial b_j b_k}{\partial x_k} \right\} \\
&= \left\{ \frac{2}{3}\mathbf{B}\cdot\nabla\tilde{p} + B\tilde{p}\left[b_j b_j \frac{\partial b_k}{\partial x_k} + b_j b_k \frac{\partial b_j}{\partial x_k} \right] \right\} = \left\{ \frac{2}{3}\mathbf{B}\cdot\nabla\tilde{p} + B\tilde{p}\left[\nabla\cdot\mathbf{b} + \mathbf{b}\cdot(\mathbf{b}\cdot\nabla)\mathbf{b} \right] \right\}
\end{aligned}
$$

$$= \left\{ \frac{2}{3}\mathbf{B}\cdot\nabla\tilde{p} + B\tilde{p}\left[\frac{1}{B}\nabla\cdot\mathbf{B} - \frac{\mathbf{B}\cdot\nabla B}{B^2} + \mathbf{b}\cdot(\nabla(\mathbf{b}\cdot\mathbf{b}) - \mathbf{b}\times(\nabla\times\mathbf{b}))\right]\right\}$$
$$= \left\{ \frac{2}{3}\mathbf{B}\cdot\nabla(p_\parallel - p_\perp) - (\mathbf{b}\cdot\nabla B)(p_\parallel - p_\perp)\right\}, \tag{A.12}$$

which is the left hand side of Eq. (A.11) showing that it is indeed the same as Eq. (A.1).

B. Normalisation and implementation of the velocity nonlinearity source terms

The source terms are given in Eq. (2.21)

$$S^a_{\mathcal{A},\alpha} = -\left\langle \left\{ \int \mathrm{d}^3 v \, \frac{\partial}{\partial v_\parallel} \left(v_\parallel L^{3/2}_{\alpha-1}(x_a^2) \right) ZeB\mathbf{b} \cdot \nabla \langle \widetilde{\phi} \rangle \widetilde{f}_a \right\} \right\rangle_t \tag{B.1}$$

$$S^a_{\mathcal{B},\alpha} = -\left\langle \left\{ \int \mathrm{d}^3 v \, \frac{\partial}{\partial v_\parallel} \left(v_\parallel L^{3/2}_{\alpha-1}(x_a^2) \right) \frac{m_a v_\parallel}{B} \mathbf{b} \times \nabla B \cdot \nabla \langle \widetilde{\phi} \rangle \widetilde{f}_a \right\} \right\rangle_t \tag{B.2}$$

$$S^a_{\mathcal{C},\alpha} = -\left\langle \left\{ \int \mathrm{d}^3 v \, \frac{\partial}{\partial v_\parallel} \left(v_\parallel L^{3/2}_{\alpha-1}(x_a^2) \right) 2m_a \mathbf{\Omega}_\perp \cdot \nabla \langle \widetilde{\phi} \rangle \widetilde{f}_a \right\} \right\rangle_t \tag{B.3}$$

The following normalisations are made according to Ref. [65]. Normalised quantities are denoted by a subscript N or R for velocity, mass and density. The velocity element is

$$\mathrm{d}^3 v = \mathrm{d}v_\parallel 2\pi v_\perp \mathrm{d}v_\perp = \frac{B}{m} \mathrm{d}v_\parallel 2\pi \mathrm{d}\left(\frac{m v_\perp^2}{2B} \right) = \frac{B}{m} \mathrm{d}v_\parallel \mathrm{d}\left(2\pi\mu\right) = B_N v_{\mathrm{th}}^3 \mathrm{d}v_{\parallel N} \mathrm{d}\left(2\pi\mu_N\right) \tag{B.4}$$

with $B = B_N B_{\mathrm{ref}}$, $v_\parallel = v_{\mathrm{th}} v_{\parallel N}$ and $\mu = m v_{\mathrm{th}}^2 / B_{\mathrm{ref}} \, \mu_N$. Furthermore: $\nabla = 1/R_{\mathrm{ref}} \, \nabla_N$, $\widetilde{\phi} = \rho_* T_{\mathrm{ref}} / e \, \phi_N$, $\widetilde{f} = \rho_* n_{R_0} / v_{\mathrm{th}}^3 \, f_N$, $\mathbf{\Omega}_\perp = v_{\mathrm{thref}} \mathbf{\Omega}_{\perp N} / R_{\mathrm{ref}}$, $n_{R_0} = n_R n_{\mathrm{ref}}$, $v_{\mathrm{th}} = v_R v_{\mathrm{thref}}$, $m = m_R m_{\mathrm{ref}}$, $x_a^2 = v^2 / v_{\mathrm{th}}^2 = (v_{\parallel N}^2 + 2 B_N \mu_N)$. The Larmor radius is $\rho = m_{\mathrm{ref}} v_{\mathrm{thref}} / (e B_{\mathrm{ref}})$ and $\rho_* = \rho / R_{\mathrm{ref}}$.

In the following all quantities except the reference values are dimensionless and the subscript N is omitted. The normalised source terms are

$$S^a_{\mathcal{A},\alpha} = -B_{\mathrm{ref}} \frac{n_{\mathrm{ref}} T_{\mathrm{ref}}}{R_{\mathrm{ref}}} \rho_*^2 n_R \left\langle \left\{ \iint \mathrm{d}v_\parallel \mathrm{d}(2\pi\mu) \, \frac{\partial}{\partial v_\parallel} \left(v_\parallel L^{3/2}_{\alpha-1}(x_a^2) \right) ZB^2 \mathbf{b} \cdot \nabla \langle \phi \rangle f_a \right\} \right\rangle_t \tag{B.5}$$

$$S^a_{\mathcal{B},\alpha} = -B_{\mathrm{ref}} \frac{n_{\mathrm{ref}} T_{\mathrm{ref}}}{R_{\mathrm{ref}}} \rho_*^2 m_R n_R v_R \left\langle \left\{ \iint \mathrm{d}v_\parallel \mathrm{d}(2\pi\mu) \, \frac{\partial}{\partial v_\parallel} \left(v_\parallel L^{3/2}_{\alpha-1}(x_a^2) \right) v_\parallel \mathbf{b} \times \nabla B \cdot \rho_* \nabla \langle \phi \rangle f_a \right\} \right\rangle_t \tag{B.6}$$

$$S^a_{\mathcal{C},\alpha} = -B_{\mathrm{ref}} \frac{n_{\mathrm{ref}} T_{\mathrm{ref}}}{R_{\mathrm{ref}}} \rho_*^2 m_R n_R \left\langle \left\{ \iint \mathrm{d}v_\parallel \mathrm{d}(2\pi\mu) \, \frac{\partial}{\partial v_\parallel} \left(v_\parallel L^{3/2}_{\alpha-1}(x_a^2) \right) 2B \mathbf{\Omega}_\perp \cdot \rho_* \nabla \langle \phi \rangle f_a \right\} \right\rangle_t \tag{B.7}$$

with the derivatives of the Laguerre polynomials given by

$$\frac{\partial}{\partial v_\parallel}\left(v_\parallel L_0^{3/2}(x_a^2)\right) = 1 \tag{B.8}$$

$$\frac{\partial}{\partial v_\parallel}\left(v_\parallel L_1^{3/2}(x_a^2)\right) = \frac{5}{2} - (v_\parallel^2 + 2B\mu) - 2v_\parallel^2 \tag{B.9}$$

$$\frac{\partial}{\partial v_\parallel}\left(v_\parallel L_2^{3/2}(x_a^2)\right) = \frac{35}{8} - \frac{7}{2}(v_\parallel^2 + 2B\mu) + \frac{1}{4}(v_\parallel^2 + 2B\mu)^2 - 7v_\parallel^2 + v_\parallel^4 \tag{B.10}$$

Hamada coordinates $\alpha = \psi, \zeta, s$ (see Sec. 1.4.1) are used and the vector products are calculated using the geometry tensors $\mathcal{F}, \mathcal{D}, \mathcal{H}$

$$\mathbf{b}\cdot\nabla = \mathcal{F}\frac{\partial}{\partial s} \tag{B.11}$$

$$\mathcal{D}^\alpha = -\frac{1}{B^2}(\nabla x_\beta \times \nabla x_\beta)\cdot\mathbf{b}\frac{\partial B}{\partial x_\beta} = \frac{1}{B^2}(\mathbf{b}\times\nabla B)\cdot\nabla x_\beta \tag{B.12}$$

$$\mathcal{H}^\alpha = -\frac{s_B}{B\Omega}\mathbf{\Omega}_\perp\cdot\nabla x_\beta \tag{B.13}$$

where s_B is the sign of the magnetic field and Ω the normalised angular frequency. Note that the approximation $\mathcal{D}^s\partial\langle\phi\rangle/\partial s = \mathcal{H}^s\partial\langle\phi\rangle/\partial s = 0$ is used, as the geometry tensors are of similar magnitude but are connected with the parallel derivative which is one order smaller in ρ_* than the perpendicular derivative. Using the representation of the gradient

$$\nabla\langle\phi\rangle = \nabla\psi\frac{\partial\langle\phi\rangle}{\partial\psi} + \nabla\zeta\frac{\partial\langle\phi\rangle}{\partial\zeta} + \nabla s\frac{\partial\langle\phi\rangle}{\partial s} \tag{B.14}$$

and the geometry tensors, the source terms are

$$S^a_{\mathcal{A},\alpha} = -B_{\text{ref}}\frac{n_{\text{ref}}T_{\text{ref}}}{R_{\text{ref}}}\rho_*^2 n_R\left\langle\left\{\iint \mathrm{d}v_\parallel\mathrm{d}(2\pi\mu)\,\frac{\partial}{\partial v_\parallel}\left(v_\parallel L_{\alpha-1}^{3/2}(x_a^2)\right)ZB^2\mathcal{F}\frac{\partial\langle\phi\rangle}{\partial s}f_a\right\}\right\rangle_t \tag{B.15}$$

$$S^a_{\mathcal{B},\alpha} = -B_{\text{ref}}\frac{n_{\text{ref}}T_{\text{ref}}}{R_{\text{ref}}}\rho_*^2 m_R n_R v_R\left\langle\left\{\iint \mathrm{d}v_\parallel\mathrm{d}(2\pi\mu)\,\frac{\partial}{\partial v_\parallel}\left(v_\parallel L_{\alpha-1}^{3/2}(x_a^2)\right)\right.\right.$$
$$\left.\left. v_\parallel B^2\left(\mathcal{D}^\psi\rho_*\frac{\partial\langle\phi\rangle}{\partial\psi} + \mathcal{D}^\zeta\rho_*\frac{\partial\langle\phi\rangle}{\partial\zeta}\right)f_a\right\}\right\rangle_t \tag{B.16}$$

$$S^a_{\mathcal{C},\alpha} = -B_{\text{ref}}\frac{n_{\text{ref}}T_{\text{ref}}}{R_{\text{ref}}}\rho_*^2 m_R n_R\left\langle\left\{\iint \mathrm{d}v_\parallel\mathrm{d}(2\pi\mu)\,\frac{\partial}{\partial v_\parallel}\left(v_\parallel L_{\alpha-1}^{3/2}(x_a^2)\right)\right.\right.$$
$$\left.\left. -2s_B B^2\Omega\left(\mathcal{H}^\psi\rho_*\frac{\partial\langle\phi\rangle}{\partial\psi} + \mathcal{H}^\zeta\rho_*\frac{\partial\langle\phi\rangle}{\partial\zeta}\right)f_a\right\}\right\rangle_t \tag{B.17}$$

The distribution function and potential use a semi-spectral space representation, i.e. ζ, ψ dependency of f and ϕ is given by Fourier modes k_ψ, k_ζ while the field aligned coordinate s is

treated in real space.

$$f(\psi,\zeta,s) = \sum_{k_\zeta>0,k_\psi}\left[\hat{f}(k_\psi,k_\zeta,s)\exp[\mathrm{i}k_\zeta\zeta/\rho_* + \mathrm{i}k_\psi\psi/\rho_*] + \hat{f}^\dagger(k_\psi,k_\zeta,s)\exp[-\mathrm{i}k_\zeta\zeta/\rho_* - \mathrm{i}k_\psi\psi/\rho_*]\right] + \sum_{k_\psi}\hat{f}(k_\psi,k_\zeta=0,s)\exp[\mathrm{i}k_\psi\psi/\rho_*] \tag{B.18}$$

With an equivalent expression for ϕ. Thus, the derivative in $\beta = \psi,\zeta$ direction is $\rho_*\partial/\partial x_\beta = ik_\beta$.

The flux surface average is, despite its name, a volume average over the volume between two infinitely close flux surfaces. The flux tube limit assumes that there is an infinitely large scale separation between the Larmor radius and the system size. A computational box in the radial direction is used that scales with the Larmor radius, and although it has a finite radial extend, this length is, within the formulation, always negligible to the system size. For this reason no radial dependence of any of the background quantities is retained in the flux tube formulation and the Jacobian $\mathcal{J}$ being a flux surface label in the GKW coordinate system is a constant that can be removed from the integral. The coordinates s and ζ are chosen such that $\int \mathrm{d}s \int \mathrm{d}\zeta = 1$. Then the flux surface average of a quantity Q in the local limit is

$$\{Q\} = \frac{\int \mathrm{d}^3x\, Q}{\int \mathrm{d}^3x} = \frac{\int \mathrm{d}s \int \mathrm{d}\psi \int \mathrm{d}\zeta\, \mathcal{J}Q}{\int \mathrm{d}s \int \mathrm{d}\psi \int \mathrm{d}\zeta\, \mathcal{J}} = \frac{1}{L_\psi}\int \mathrm{d}s \int \mathrm{d}\psi \int \mathrm{d}\zeta\, Q, \tag{B.19}$$

where L_ψ is the radial box size. Note that in the flux tube approximation only f and ϕ depend on ψ and ζ in Eqs. (B.15-B.17). Hence the ψ and ζ integral of the $\partial\phi/\partial x_\beta f$ part of the equations be can directly simplified, as the quantities are periodic in k_ψ, k_ζ. Thus, a space integral over a nonzero wave vector (or a combination of wave vectors) vanishes.

$$\begin{aligned}
&\frac{1}{L_\psi}\int \mathrm{d}\psi \int \mathrm{d}\zeta\, \rho_*\frac{\partial\phi}{\partial\psi}f = \frac{1}{L_\psi}\int \mathrm{d}\psi \int \mathrm{d}\zeta \left(\sum_{k_\zeta>0,k_\psi}\left[\mathrm{i}k_\psi\hat{\phi}(k_\psi,k_\zeta,s)\exp[\mathrm{i}k_\zeta\zeta/\rho_* + \mathrm{i}k_\psi\psi/\rho_*]\right.\right.\\
&\left.\left. - \mathrm{i}k_\psi\hat{\phi}^\dagger(k_\psi,k_\zeta,s)\exp[-\mathrm{i}k_\zeta\zeta/\rho_* - \mathrm{i}k_\psi\psi/\rho_*]\right] + \sum_{k_\psi}\mathrm{i}k_\psi\hat{\phi}(k_\psi,k_\zeta=0,s)\exp[\mathrm{i}k_\psi\psi/\rho_*]\right)\\
&\left(\sum_{k'_\zeta>0,k'_\psi}\left[\hat{f}(k'_\psi,k'_\zeta,s)\exp[\mathrm{i}k'_\zeta\zeta/\rho_* + \mathrm{i}k'_\psi\psi/\rho_*] + \hat{f}^\dagger(k'_\psi,k'_\zeta,s)\exp[-\mathrm{i}k'_\zeta\zeta/\rho_* - \mathrm{i}k'_\psi\psi/\rho_*]\right]\right.\\
&\left. + \sum_{k'_\psi}\hat{f}(k'_\psi,k'_\zeta=0,s)\exp[\mathrm{i}k'_\psi\psi/\rho_*]\right)\\
&= \sum_{k_\zeta>0,k_\psi}\left[\mathrm{i}k_\psi\hat{\phi}\hat{f}^\dagger - \mathrm{i}k_\psi\hat{\phi}^\dagger\hat{f}\right] + \sum_{k_\psi}\mathrm{i}k_\psi\hat{\phi}(k_\psi,k_\zeta=0,s)\hat{f}(-k_\psi,k_\zeta=0,s)
\end{aligned}$$

$$
\begin{aligned}
&= \sum_{k_\zeta>0,k_\psi} 2k_\psi \Re\left[\mathrm{i}\hat{\phi}\hat{f}^\dagger\right] + \sum_{k_\psi} \mathrm{i}k_\psi \hat{\phi}(k_\psi, k_\zeta = 0, s)\hat{f}^\dagger(k_\psi, k_\zeta = 0, s) \\
&= \sum_{k_\zeta>0,k_\psi} -2k_\psi \Im\left[\hat{\phi}\hat{f}^\dagger\right] + \sum_{k_\psi>0} \mathrm{i}k_\psi \hat{\phi}(k_\psi, 0, s)\hat{f}^\dagger(k_\psi, 0, s) + \underbrace{\sum_{k_\psi<0} \mathrm{i}k_\psi \hat{\phi}(k_\psi, 0, s)\hat{f}^\dagger(k_\psi, 0, s)}_{=\sum_{k_\psi>0} -\mathrm{i}k_\psi \hat{\phi}^\dagger(k_\psi,0,s)\hat{f}(k_\psi,0,s)} \\
&= \sum_{k_\zeta>0,k_\psi} -2k_\psi \Im\left[\hat{\phi}\hat{f}^\dagger\right] + \sum_{k_\zeta=0,k_\psi>0} -2k_\psi \Im\left[\hat{\phi}\hat{f}^\dagger\right] \\
&= \sum_{k_\zeta>0,k_\psi} -2k_\psi \Im\left[\hat{\phi}\hat{f}^\dagger\right] + \sum_{k_\zeta=0,k_\psi>0} -k_\psi \Im\left[\hat{\phi}\hat{f}^\dagger\right] + \sum_{k_\psi<0} k_\psi \Im\left[\hat{\phi}(-k_\psi, 0, s)\hat{f}^\dagger(-k_\psi, 0, s)\right] \\
&= \sum_{k_\zeta>0,k_\psi} -2k_\psi \Im\left[\hat{\phi}\hat{f}^\dagger\right] + \sum_{k_\zeta=0,k_\psi>0} -k_\psi \Im\left[\hat{\phi}\hat{f}^\dagger\right] + \sum_{k_\psi<0} k_\psi \underbrace{\Im\left[\hat{\phi}^\dagger(k_\psi, 0, s)\hat{f}(k_\psi, 0, s)\right]}_{=-\Im\left[\hat{\phi}(k_\psi,0,s)\hat{f}^\dagger(k_\psi,0,s)\right]} \\
&= \sum_{k_\zeta>0,k_\psi} -2k_\psi \Im\left[\hat{\phi}\hat{f}^\dagger\right] + \sum_{k_\zeta=0,k_\psi} -k_\psi \Im\left[\hat{\phi}\hat{f}^\dagger\right] = \sum_{k_\zeta,k_\psi} -\gamma(k_\zeta)k_\psi \Im\left[\hat{\phi}\hat{f}^\dagger\right]
\end{aligned} \tag{B.20}
$$

with $\gamma(k_\zeta > 0) = 2$ and $\gamma(k_\zeta = 0) = 1$ and $\Re$ ($\Im$) taking the real (imaginary) part of the expression. The expression for the ζ derivative is equivalent and an analogous calculation for $\partial\phi/\partial s$ leads to

$$
\int \mathrm{d}\psi \int \mathrm{d}\zeta \, \frac{\partial \phi}{\partial s} f = \sum_{k_\psi,k_\zeta} \gamma(k_\zeta) \Re\left[\frac{\partial \hat{\phi}}{\partial s}\hat{f}^\dagger\right] \tag{B.21}
$$

The moments are output for every large time step and the time average is done post simulation. For the sake of completeness the terms as in written the code (for each species) are

$$
S_{\mathcal{A},\alpha} = -\sum_{k_\psi,k_\zeta} \iint \mathrm{d}v_\parallel \mathrm{d}\,(2\pi\mu) \int \mathrm{d}s \; (Z n_R B^2) \frac{\partial}{\partial v_\parallel}\left(v_\parallel L_{\alpha-1}^{3/2}(x_a^2)\right) \gamma(k_\zeta) \mathcal{F} \Re\left[\frac{\partial \langle\hat{\phi}\rangle}{\partial s}\hat{f}^\dagger\right] \tag{B.22}
$$

$$
S_{\mathcal{B},\alpha} = \sum_{k_\psi,k_\zeta} \iint \mathrm{d}v_\parallel \mathrm{d}\,(2\pi\mu) \int \mathrm{d}s \; (m_R n_R v_R B^2) v_\parallel \frac{\partial}{\partial v_\parallel}\left(v_\parallel L_{\alpha-1}^{3/2}(x_a^2)\right) \gamma(k_\zeta) \mathcal{D}^\beta k_\beta \Im\left[\langle\hat{\phi}\rangle\hat{f}^\dagger\right] \tag{B.23}
$$

$$
S_{\mathcal{C},\alpha} = -\sum_{k_\psi,k_\zeta} \iint \mathrm{d}v_\parallel \mathrm{d}\,(2\pi\mu) \int \mathrm{d}s \; (2 m_R n_R s_B B^2 \Omega) \frac{\partial}{\partial v_\parallel}\left(v_\parallel L_{\alpha-1}^{3/2}(x_a^2)\right) \gamma(k_\zeta) \mathcal{H}^\beta k_\beta \Im\left[\langle\hat{\phi}\rangle\hat{f}^\dagger\right] \tag{B.24}
$$

with $\beta = \psi, \zeta$. Note that the factor for denormalisation is $\rho_*^2 B_{\mathrm{ref}} n_{\mathrm{ref}} T_{\mathrm{ref}}/R_{\mathrm{ref}}$.

Bibliography

[1] K. Ikeda, "ITER on the road to fusion energy", *Nuclear Fusion* **50**, 014002 (2009).

[2] D. Meade, "50 years of fusion research", *Nuclear Fusion* **50**, 014004 (2009).

[3] J. Wesson, *Tokamaks*, 4th ed. (Oxford University Press, 2011).

[4] W. M. Stacey, *Fusion Plasma Physics*, 2nd ed. (John Wiley & Sons, 2012).

[5] R. Fitzpatrick, *Plasma Physics: An Introduction*, 1st ed. (CRC Press, 2014).

[6] A. G. Peeters, C. Angioni, and D. Strintzi, "Toroidal momentum pinch velocity due to the coriolis drift effect on small scale instabilities in a toroidal plasma", *Physical Review Letters* **98**, 265003 (2007).

[7] S. Li, H. Jiang, Z. Ren, and C. Xu, "Optimal tracking for a divergent-type parabolic PDE system in current profile control", *Abstract and Applied Analysis* **2014**, 940965 (2014).

[8] H. Grad and H. Rubin, "Hydromagnetic equilibria and force-free fields", *Journal of Nuclear Energy* **7**, 284–285 (1958).

[9] V. D. Shafranov, "On magnetohydrodynamical equilibrium configurations", *Soviet Physics JETP* **6**, 545–554 (1958).

[10] V. D. Shafranov, "Plasma equilibrium in a magnetic field", *Reviews of Plasma Physics* **2**, 103 (1966).

[11] A. A. Galeev and R. Z. Sagdeev, "Transport phenomena in a collisionless plasma in a toroidal magnetic system", *Soviet Physics JETP* **26**, 233–240 (1968).

[12] R. J. Bickerton, J. W. Connor, and J. B. Taylor, "Diffusion driven plasma currents and bootstrap tokamak", *Nature Physical Science* **229**, 110–112 (1971).

[13] A. G. Peeters, "The bootstrap current and its consequences", *Plasma Physics and Controlled Fusion* **42**, B231–B242 (2000).

[14] S. P. Hirshman and D. J. Sigmar, "Neoclassical transport of impurities in tokamak plasmas", *Nuclear Fusion* **21**, 1079–1201 (1981).

[15] W. A. Houlberg, K. C. Shaing, S. P. Hirshman, and M. C. Zarnstorff, "Bootstrap current and neoclassical transport in tokamaks of arbitrary collisionality and aspect ratio", *Physics of Plasmas* **4**, 3230–3242 (1997).

[16] W. Horton, "Drift waves and transport", *Reviews of Modern Physics* **71**, 735–778 (1999).

[17] S. C. Cowley, R. M. Kulsrud, and R. Sudan, "Considerations of ion-temperature-gradient-driven turbulence", *Physics of Fluids B: Plasma Physics* **3**, 2767–2782 (1991).

[18] A. M. Dimits, G. Bateman, M. A. Beer, B. I. Cohen, W. Dorland, G. W. Hammett, C. Kim, J. E. Kinsey, M. Kotschenreuther, A. H. Kritz, et al., "Comparisons and physics basis of tokamak transport models and turbulence simulations", *Physics of Plasmas* **7**, 969–983 (2000).

[19] A. G. Peeters, F. Rath, R. Buchholz, Y. Camenen, J. Candy, F. J. Casson, S. R. Grosshauser, W. A. Hornsby, D. Strintzi, and A. Weikl, "Gradient-driven flux-tube simulations of ion temperature gradient turbulence close to the non-linear threshold", *Physics of Plasmas* **23**, 082517 (2016).

[20] P. H. Diamond, S. I. Itoh, K. Itoh, and T. S. Hahm, "Zonal flows in plasma—a review", *Plasma Physics and Controlled Fusion* **47**, R35–R161 (2005).

[21] A. Weikl, A. G. Peeters, F. Rath, S. R. Grosshauser, R. Buchholz, W. A. Hornsby, F. Seiferling, and D. Strintzi, "Ion temperature gradient turbulence close to the finite heat flux threshold", *Physics of Plasmas* **24**, 102317 (2017).

[22] F. Rath, A. G. Peeters, R. Buchholz, S. R. Grosshauser, F. Seiferling, and A. Weikl, "On the tertiary instability formalism of zonal flows in magnetized plasmas", *Physics of Plasmas* **25**, 052102 (2018).

[23] F. Seiferling, A. G. Peeters, R. Buchholz, S. R. Grosshauser, F. Rath, and A. Weikl, "Damping of zonal modes through turbulent momentum transport", *Physics of Plasmas* **25**, 022505 (2018).

[24] G. Dif-Pradalier, G. Hornung, X. Garbet, P. Ghendrih, V. Grandgirard, G. Latu, and Y. Sarazin, "The E×B staircase of magnetised plasmas", *Nuclear Fusion* **57**, 066026 (2017).

[25] P. H. Diamond and Y. .-. Kim, "Theory of mean poloidal flow generation by turbulence", *Physics of Fluids B: Plasma Physics* **3**, 1626–1633 (1991).

[26] P. N. Guzdar, "Shear-flow generation by drift/rossby waves", *Physics of Plasmas* **2**, 4174–4176 (1995).

[27] L. Chen, Z. Lin, and R. White, "Excitation of zonal flow by drift waves in toroidal plasmas", *Physics of Plasmas* **7**, 3129–3132 (2000).

[28] A. I. Smolyakov, P. H. Diamond, and V. I. Shevchenko, "Zonal flow generation by parametric instability in magnetized plasmas and geostrophic fluids", *Physics of Plasmas* **7**, 1349–1351 (2000).

[29] P. N. Guzdar, R. G. Kleva, and L. Chen, "Shear flow generation by drift waves revisited", *Physics of Plasmas* **8**, 459–462 (2001).

[30] G. Manfredi, C. M. Roach, and R. O. Dendy, "Zonal flow and streamer generation in drift turbulence", *Plasma Physics and Controlled Fusion* **43**, 825–837 (2001).

[31] Y. Nagashima, S.-I. Itoh, S. Shinohara, M. Fukao, A. Fujisawa, K. Terasaka, Y. Kawai, G. R. Tynan, P. H. Diamond, M. Yagi, et al., "Observation of the parametric-modulational instability between the drift-wave fluctuation and azimuthally symmetric sheared radial electric field oscillation in a cylindrical laboratory plasma", *Physics of Plasmas* **16**, 020706 (2009).

[32] Z. Lin, T. S. Hahm, W. W. Lee, W. M. Tang, and P. H. Diamond, "Effects of collisional zonal flow damping on turbulent transport", *Physical Review Letters* **83**, 3645–3648 (1999).

[33] B. N. Rogers, W. Dorland, and M. Kotschenreuther, "Generation and stability of zonal flows in ion-temperature-gradient mode turbulence", *Physical Review Letters* **85**, 5336–5339 (2000).

[34] F. Wagner, G. Becker, K. Behringer, D. Campbell, A. Eberhagen, W. Engelhardt, G. Fussmann, O. Gehre, J. Gernhardt, G. v. Gierke, et al., "Regime of improved confinement and high beta in neutral-beam-heated divertor discharges of the asdex tokamak", *Physical Review Letters* **49**, 1408–1412 (1982).

[35] T. S. Hahm and K. H. Burrell, "Flow shear induced fluctuation suppression in finite aspect ratio shaped tokamak plasma", *Physics of Plasmas* **2**, 1648–1651 (1995).

[36] P. W. Terry, "Suppression of turbulence and transport by sheared flow", *Reviews of Modern Physics* **72**, 109–165 (2000).

[37] G. M. Staebler, R. E. Waltz, J. Candy, and J. E. Kinsey, "New paradigm for suppression of gyrokinetic turbulence by velocity shear", *Physical Review Letters* **110**, 055003 (2013).

[38] T. S. Hahm, M. A. Beer, Z. Lin, G. W. Hammett, W. W. Lee, and W. M. Tang, "Shearing rate of time-dependent E×B flow", *Physics of Plasmas* **6**, 922–926 (1999).

[39] R. E. Waltz, G. D. Kerbel, and J. Milovich, "Toroidal gyro-landau fluid model turbulence simulations in a nonlinear ballooning mode representation with radial modes", *Physics of Plasmas* **1**, 2229–2244 (1994).

[40] R. E. Waltz, R. L. Dewar, and X. Garbet, "Theory and simulation of rotational shear stabilization of turbulence", *Physics of Plasmas* **5**, 1784–1792 (1998).

[41] G. Dif-Pradalier, P. H. Diamond, V. Grandgirard, Y. Sarazin, J. Abiteboul, X. Garbet, P. Ghendrih, A. Strugarek, S. Ku, and C. S. Chang, "On the validity of the local diffusive paradigm in turbulent plasma transport", *Physical Review E* **82**, 025401 (2010).

[42] G. Dif-Pradalier, G. Hornung, P. Ghendrih, Y. Sarazin, F. Clairet, L. Vermare, P. H. Diamond, J. Abiteboul, T. Cartier-Michaud, C. Ehrlacher, et al., "Finding the elusive $\mathbf{E} \times \mathbf{B}$ staircase in magnetized plasmas", *Physical Review Letters* **114**, 085004 (2015).

[43] F. Rath, A. G. Peeters, R. Buchholz, S. R. Grosshauser, P. Migliano, A. Weikl, and D. Strintzi, "Comparison of gradient and flux driven gyro-kinetic turbulent transport", *Physics of Plasmas* **23**, 052309 (2016).

[44] A. C. C. Sips et al., "Advanced scenarios for ITER operation", *Plasma Physics and Controlled Fusion* **47**, A19–A40 (2005).

[45] J. A. Krommes, "The gyrokinetic description of microturbulence in magnetized plasmas", *Annual Review of Fluid Mechanics* **44**, 175–201 (2012).

[46] A. J. Brizard and T. S. Hahm, "Foundations of nonlinear gyrokinetic theory", *Reviews of Modern Physics* **79**, 421–468 (2007).

[47] X. Garbet, Y. Idomura, L. Villard, and T. H. Watanabe, "Gyrokinetic simulations of turbulent transport", *Nuclear Fusion* **50**, 043002 (2010).

[48] J. R. Cary, "Lie transform perturbation theory for hamiltonian systems", *Physics Reports* **79**, 129–159 (1981).

[49] J. R. Cary and R. G. Littlejohn, "Noncanonical hamiltonian mechanics and its application to magnetic field line flow", *Annals of Physics* **151**, 1–34 (1983).

[50] R. G. Littlejohn, "A guiding center hamiltonian: a new approach", *Journal of Mathematical Physics* **20**, 2445–2458 (1979).

[51] R. G. Littlejohn, "Hamiltonian formulation of guiding center motion", *The Physics of Fluids* **24**, 1730–1749 (1981).

[52] R. G. Littlejohn, "Hamiltonian perturbation theory in noncanonical coordinates", *Journal of Mathematical Physics* **23**, 742–747 (1982).

[53] R. G. Littlejohn, "Variational principles of guiding centre motion", *Journal of Plasma Physics* **29**, 111–125 (1983).

[54] D. H. Dubin, J. A. Krommes, C. Oberman, and W. W. Lee, "Nonlinear gyrokinetic equations", *The Physics of Fluids* **26**, 3524–3535 (1983).

[55] T. S. Hahm, W. W. Lee, and A. Brizard, "Nonlinear gyrokinetic theory for finite-beta plasmas", *The Physics of Fluids* **31**, 1940–1948 (1988).

[56] T. S. Hahm, "Nonlinear gyrokinetic equations for tokamak microturbulence", *The Physics of Fluids* **31**, 2670–2673 (1988).

[57] A. Brizard, "Nonlinear gyrokinetic Maxwell-Vlasov equations using magnetic coordinates", *Journal of Plasma Physics* **41**, 541–559 (1989).

[58] E. A. Frieman and L. Chen, "Nonlinear gyrokinetic equations for low-frequency electromagnetic waves in general plasma equilibria", *The Physics of Fluids* **25**, 502–508 (1982).

[59] W. W. Lee, "Gyrokinetic approach in particle simulation", *The Physics of Fluids* **26**, 556–562 (1983).

[60] S. Hamada, *Kakuyugo Kenkyu* **1**, 542 (1958).

[61] S. Hamada, "Hydromagnetic equilibria and their proper coordinates", *Nuclear Fusion* **2**, 23 (1962).

[62] X. Lapillonne, S. Brunner, T. Dannert, S. Jolliet, A. Marinoni, L. Villard, T. Görler, F. Jenko, and F. Merz, "Clarifications to the limitations of the s-α equilibrium model for gyrokinetic computations of turbulence", *Physics of Plasmas* **16**, 032308 (2009).

[63] V. D. Shafranov, "Equilibrium of a toroidal pinch in a magnetic field", *Soviet Atomic Energy* **13**, 1149–1158 (1963).

[64] M. A. Beer, S. C. Cowley, and G. W. Hammett, "Field-aligned coordinates for nonlinear simulations of tokamak turbulence", *Physics of Plasmas* **2**, 2687–2700 (1995).

[65] A. G. Peeters, Y. Camenen, F. J. Casson, W. A. Hornsby, A. P. Snodin, D. Strintzi, and G. Szepesi, "The nonlinear gyro-kinetic flux tube code gkw", *Computer Physics Communications* **180**, 2650–2672 (2009).

[66] A. G. Peeters, D. Strintzi, Y. Camenen, C. Angioni, F. J. Casson, W. A. Hornsby, and A. P. Snodin, "Influence of the centrifugal force and parallel dynamics on the toroidal momentum transport due to small scale turbulence in a tokamak", *Physics of Plasmas* **16**, 042310 (2009).

[67] F. J. Casson, A. G. Peeters, C. Angioni, Y. Camenen, W. A. Hornsby, A. P. Snodin, and G. Szepesi, "Gyrokinetic simulations including the centrifugal force in a rotating tokamak plasma", *Physics of Plasmas* **17**, 102305 (2010).

[68] C. F. Karney, "Fokker-Planck and quasilinear codes", *Computer Physics Reports* **4**, 183–244 (1986).

[69] M. Barnes, F. I. Parra, J. P. Lee, E. A. Belli, M. F. F. Nave, and A. E. White, "Intrinsic rotation driven by non-maxwellian equilibria in tokamak plasmas", *Physical Review Letters* **111**, 055005 (2013).

[70] J. Lee, F. I. Parra, and M. Barnes, "Turbulent momentum pinch of diamagnetic flows in a tokamak", *Nuclear Fusion* **54**, 022002 (2014).

[71] J. Lee, M. Barnes, F. I. Parra, E. Belli, and J. Candy, "Turbulent momentum transport due to neoclassical flows", *Plasma Physics and Controlled Fusion* **57**, 125006 (2015).

[72] P. Manas, W. A. Hornsby, C. Angioni, Y. Camenen, and A. G. Peeters, "Impact of the neoclassical distribution function on turbulent impurity and momentum fluxes: fluid model and gyrokinetic simulations", *Plasma Physics and Controlled Fusion* **59**, 035002 (2017).

[73] W. A. Hornsby, C. Angioni, E. Fable, P. Manas, R. McDermott, A. G. Peeters, M. Barnes, F. Parra, et al., "On the effect of neoclassical flows on intrinsic momentum in ASDEX Upgrade Ohmic L-mode plasmas", *Nuclear Fusion* **57**, 046008 (2017).

[74] Z. X. Lu, E. Fable, W. A. Hornsby, C. Angioni, A. Bottino, P. Lauber, and F. Zonca, "Symmetry breaking of ion temperature gradient mode structure: from local to global analysis", *Physics of Plasmas* **24**, 042502 (2017).

[75] W. A. Hornsby, C. Angioni, Z. X. Lu, E. Fable, I. Erofeev, R. McDermott, A. Medvedeva, A. Lebschy, A. G. Peeters, and T. A. U. Team, "Global gyrokinetic simulations of intrinsic rotation in ASDEX Upgrade Ohmic L-mode plasmas", *Nuclear Fusion* **58**, 056008 (2018).

[76] D. Estève, Y. Sarazin, X. Garbet, V. Grandgirard, S. Breton, P. Donnel, Y. Asahi, C. Bourdelle, G. Dif-Pradalier, C. Ehrlacher, et al., "Self-consistent gyrokinetic modeling of neoclassical and turbulent impurity transport", *Nuclear Fusion* **58**, 036013 (2018).

[77] F. I. Parra and M. Barnes, "Intrinsic rotation in tokamaks: theory", *Plasma Physics and Controlled Fusion* **57**, 045002 (2015).

[78] J. Schmidt and S. Yoshikawa, "Anomalous viscosity as a possible explanation for an anomalous plasma skin effect", *Physical Review Letters* **26**, 753–756 (1971).

[79] F. L. Hinton, R. E. Waltz, and J. Candy, "Effects of electromagnetic turbulence in the neoclassical Ohm's law", *Physics of Plasmas* **11**, 2433–2440 (2004).

[80] C. J. McDevitt, X.-Z. Tang, and Z. Guo, "Turbulence-driven bootstrap current in low-collisionality tokamaks", *Physical Review Letters* **111**, 205002 (2013).

[81] X. Garbet, D. Esteve, Y. Sarazin, G. Dif-Pradalier, P. Ghendrih, V. Grandgirard, G. Latu, and A. Smolyakov, "Turbulent current drive", *Journal of Physics: Conference Series* **561**, 012007 (2014).

[82] C. J. McDevitt, X.-Z. Tang, and Z. Guo, "Turbulent current drive mechanisms", *Physics of Plasmas* **24**, 082307 (2017).

[83] I. Chavdarovski and R. Gatto, "Turbulent contributions to Ohm's law in axisymmetric magnetized plasmas", *Physics of Plasmas* **24**, 072512 (2017).

[84] A. G. Peeters, C. Angioni, and the ASDEX Upgrade Team, "Linear gyrokinetic calculations of toroidal momentum transport in a tokamak due to the ion temperature gradient mode", *Physics of Plasmas* **12**, 072515 (2005).

[85] A. G. Peeters, C. Angioni, A. Bortolon, Y. Camenen, F. J. Casson, B. Duval, L. Fiederspiel, W. A. Hornsby, Y. Idomura, T. Hein, et al., "Overview of toroidal momentum transport", *Nuclear Fusion* **51**, 094027 (2011).

[86] F. I. Parra, M. Barnes, and A. G. Peeters, "Up-down symmetry of the turbulent transport of toroidal angular momentum in tokamaks", *Physics of Plasmas* **18**, 062501 (2011).

[87] F. L. Hinton and S. K. Wong, "Neoclassical ion transport in rotating axisymmetric plasmas", *The Physics of Fluids* **28**, 3082–3098 (1985).

[88] A. G. Peeters, "Reduced charge state equations that describe Pfirsch-Schlüter impurity transport in tokamak plasma", *Physics of Plasmas* **7**, 268–275 (2000).

[89] O. Sauter, C. Angioni, and Y. R. Lin-Liu, "Neoclassical conductivity and bootstrap current formulas for general axisymmetric equilibria and arbitrary collisionality regime", *Physics of Plasmas* **6**, 2834–2839 (1999).

[90] J. E. Rice, A. Ince-Cushman, J. S. deGrassie, L. .-.-G. Eriksson, Y. Sakamoto, A. Scarabosio, A. Bortolon, K. H. Burrell, B. P. Duval, C. Fenzi-Bonizec, et al., "Inter-machine comparison of intrinsic toroidal rotation in tokamaks", *Nuclear Fusion* **47**, 1618–1624 (2007).

[91] H. Biglari, P. H. Diamond, and P. W. Terry, "Influence of sheared poloidal rotation on edge turbulence", *Physics of Fluids B: Plasma Physics* **2**, 1–4 (1990).

[92] P. H. Diamond, Y. Kosuga, Ö. D. Gürcan, C. J. McDevitt, T. S. Hahm, N. Fedorczak, J. E. Rice, W. X. Wang, S. Ku, J. M. Kwon, et al., "An overview of intrinsic torque and momentum transport bifurcations in toroidal plasmas", *Nuclear Fusion* **53**, 104019 (2013).

[93] M. Barnes, F. I. Parra, E. G. Highcock, A. A. Schekochihin, S. C. Cowley, and C. M. Roach, "Turbulent transport in tokamak plasmas with rotational shear", *Physical Review Letters* **106**, 175004 (2011).

[94] E. A. Belli and J. Candy, "Kinetic calculation of neoclassical transport including self-consistent electron and impurity dynamics", *Plasma Physics and Controlled Fusion* **50**, 095010 (2008).

[95] P. H. Diamond, S. Champeaux, M. Malkov, A. Das, I. Gruzinov, M. N. Rosenbluth, C. Holland, B. Wecht, A. I. Smolyakov, F. L. Hinton, et al., "Secondary instability in drift wave turbulence as a mechanism for zonal flow and avalanche formation", *Nuclear Fusion* **41**, 1067–1080 (2001).

[96] M. N. Rosenbluth and F. L. Hinton, "Poloidal flow driven by ion-temperature-gradient turbulence in tokamaks", *Physical Review Letters* **80**, 724–727 (1998).

[97] W. Sengupta and A. B. Hassam, "Effective mass in rosenbluth-hinton type zonal flows", *arXiv*, 1602. 04366.

[98] R. E. Waltz, G. M. Staebler, J. Candy, and F. L. Hinton, "Gyrokinetic theory and simulation of angular momentum transport", *Physics of Plasmas* **14**, 122507 (2007).

[99] R. E. Waltz and C. Holland, "Numerical experiments on the drift wave-zonal flow paradigm for nonlinear saturation", *Physics of Plasmas* **15**, 122503 (2008).

[100] A. Bondeson and D. J. Ward, "Stabilization of external modes in tokamaks by resistive walls and plasma rotation", *Physical Review Letters* **72**, 2709–2712 (1994).

[101] E. J. Strait, T. S. Taylor, A. D. Turnbull, J. R. Ferron, L. L. Lao, B. Rice, O. Sauter, S. J. Thompson, and D. Wróblewski, "Wall stabilization of high beta tokamak discharges in DIII-D", *Physical Review Letters* **74**, 2483–2486 (1995).

[102] A. Weikl, A. G. Peeters, F. Rath, F. Seiferling, R. Buchholz, S. R. Grosshauser, and D. Strintzi, "The occurrence of staircases in ITG turbulence with kinetic electrons and the zonal flow drive through self-interaction", *Physics of Plasmas* **25**, 072305 (2018).